

# **NYU WIRELESS TR 2014-003**

## *Technical Report*

# **73 GHz Millimeter-Wave Indoor and Foliage Propagation Channel Measurements and Results**

**Shuai Nie, Mathew K. Samimi, Ting Wu, Sijia Deng,  
George R. MacCartney, Jr., Theodore S. Rappaport**  
shuainie@nyu.edu, mks@nyu.edu, ting.wu@nyu.edu,  
sijia@nyu.edu, gmac@nyu.edu, tsr@nyu.edu

NYU WIRELESS  
NYU Polytechnic School of Engineering  
2 MetroTech Center  
Brooklyn, NY 11201

July 29, 2014



## Abstract

This technical report provides measurement results and propagation models for the 73 GHz millimeter-wave indoor, free space, foliage, polarization, and ground bounce measurement campaign conducted by the NYU WIRELESS team from Fall 2013 through Summer 2014. This work was sponsored by Nokia, and benefitted from additional support from the NYU WIRELESS Industrial Affiliates program and the National Science Foundation. The measurements were performed in Brooklyn, New York, on the campus of the NYU Polytechnic School of Engineering using a 400 Mega-chip-per-second sliding correlator channel sounder system. The measurement system included the use of steerable, directional horn antennas at both the transmitter and receiver, where both vertical and horizontal polarizations were used to measure co- and cross-polarized channel behavior. The indoor measurements were conducted in a typical office environment on the 9<sup>th</sup> floor of 2 MetroTech Center, Brooklyn, NY for co- and cross-polarization antenna configurations with transmitters located at a height of 2.5 meters near the ceiling (similar to current indoor wireless access points), and the receivers located at heights of 1.5 meters (similar to current cubicle and human level heights). Free space, foliage, and ground bounce measurements for both co- and cross-polarized antennas were conducted on the MetroTech Commons Courtyard, Brooklyn, NY with the transmitter at a lamppost access point height (4.06 meters) and the receivers at 2 meters above ground level. This technical report presents the measurement locations, the measurement configurations performed for each transmitter and receiver combination, the procedures for post-processing the raw collected data, and the measurement results, including directional (unique pointing angle) and omnidirectional path loss models, propagation characteristics such as number of multipath components, RMS delay spread as a function of the T-R separation distance, and spatial characteristics, all for the

indoor wireless channel. Free space, foliage attenuation, and ground bounce results and models are also presented for the outdoor 73 GHz wireless channel. Results show that 73 GHz indoor channels are not very different from UHF channels, and most receiver locations have at least a few distinct angles of arrival with multipath energy. For the omnidirectional indoor model, the vertically polarized measurements have a line-of-sight path loss exponent better than free space due to ground bounces in an office environment, and the non-line-of-sight path loss exponent is 3.1, not significantly higher than common UHF non-line-of-sight channels. The outdoor free space measurements show the viability of line-of-sight links in a busy courtyard environment and the foliage measurements produced attenuation loss factors and ground bounce reflection coefficients that can be used in the future to estimate the 73 GHz outdoor channel performance in computer simulations.

# Table of Contents

Chapter 1	Background on Millimeter-Wave Radio Propagation Channels.....	1
1.1	Project Overview .....	1
1.2	Report Overview.....	2
1.3	Motivation for Indoor and Courtyard Millimeter-Wave Propagation Channel Modeling .....	3
Chapter 2	Literature Review of Past Indoor and Foliage Measurements .....	7
2.1	Introduction.....	7
2.2	Indoor Single Floor Propagation Study .....	7
2.2.1	Path Loss Studies .....	7
2.2.2	Delay Spread Studies .....	14
2.3	Indoor Multi-Floor Studies .....	16
2.4	Outdoor-to-Indoor Propagation Studies.....	18
2.5	Reflection, Refractive, and Transmission Coefficient Studies .....	19
2.6	Antenna Pattern Diversity Studies .....	25
2.7	Indoor Channel Models and E-band Regulations .....	28
2.7.1	ITU Recommendation ITU-R P.1238-7.....	28
2.7.2	E-Band Regulations in the United States and Europe.....	29
2.7.2.1	FCC Regulation.....	29
2.7.2.2	European ETSI Regulation.....	32
2.8	Foliage Studies.....	33
2.9	Ray-tracing and Modeling for Wireless Channels.....	34

Chapter 3	Indoor and Outdoor Measurement Campaign Overview .....	37
3.1	Channel Sounder System and Hardware.....	37
3.1.1	Transmitter Hardware Descriptions .....	38
3.1.1.1	Pseudorandom Noise Sequence Generating PCB Board .....	39
3.1.1.2	Intermediate Frequency Synthesizer .....	39
3.1.1.3	Local Oscillator Frequency Synthesizer .....	42
3.1.1.4	Up-Converter Box .....	42
3.1.1.5	Transmitter Antennas .....	43
3.1.2	Receiver Hardware Descriptions.....	44
3.1.1	20 dBi Antenna Pattern Characteristics .....	45
3.1.1.1	Antenna Pattern Basics.....	45
3.1.1.2	Antenna Measurement Procedures.....	48
3.2	Measurement Descriptions.....	55
3.2.1	Indoor Measurement Environment and System Specifications .....	55
3.2.1.1	Measurement Descriptions for the MTC1 Transmitter .....	59
3.2.1.2	Measurement Descriptions for the MTC2 Transmitter .....	62
3.2.2	Outdoor Measurement Campaign .....	63
3.2.2.1	Measurement Environment and System Specifications .....	66
3.2.2.2	Free Space Measurement Descriptions for the CMN_FS1 Transmitter .....	68
3.2.2.3	Foliage and Ground Bounce Descriptions for the CMN1 Transmitter .....	68
Chapter 4	Data Post-Processing.....	71

4.1	Overview of Data Acquisition .....	71
4.2	Calibration Routine .....	71
4.3	PDP Thresholding Algorithm .....	73
4.4	Measurement Log Sheets .....	74
4.5	Hierarchical Structure of Raw Data .....	76
Chapter 5	73 GHz Indoor Measurement Analysis .....	79
5.1	Path Loss Models for the 73 GHz Indoor Channel .....	79
5.2	Propagation Characteristics of the 73 GHz Indoor Channel .....	85
5.3	73 GHz LOS and NLOS Spatial (Lobe) Statistics .....	91
5.4	73 GHz Indoor Office Environment Partition-Dependent Path Loss Model .....	100
5.4.1	Partition-Dependent Directional Antenna Model .....	100
5.4.2	Partition-Dependent Omnidirectional Model .....	103
Chapter 6	Measurement Analysis of the 73 GHz Outdoor Free Space and Foliage Environment .....	106
6.1	73 GHz Outdoor Free Space Channel .....	106
6.1.1	Free Space Path Loss Models .....	107
6.1.2	Propagation Characteristics of the 73 GHz Free Space Channel .....	110
6.2	73 GHz Outdoor Channel with Foliage .....	115
6.2.1	Foliage Attenuation Path Loss Models .....	116
6.2.2	Characteristics of the Outdoor 73 GHz Propagation Channel with Foliage .....	120
6.2.3	Ground Bounce Reflection Coefficient .....	125
Chapter 7	Conclusion .....	130
References	.....	133

# List of Figures

Fig. 1.1 The atmospheric attenuation at microwave and mmWave frequency bands. The white circle denotes frequencies with very low attenuation used for current cellular, the green circles represent frequency bands for potential backhaul and mobile access technologies with low atmospheric attenuation for short cell radii, and the blue circles show higher atmospheric attenuation bands. The yellow circle points out the atmospheric attenuation at 73 GHz and is about 0.09 dB / 200 meters [4].....5

Fig. 2.1 The configuration of partition loss measurements.  $d_1$  and  $d_2$  are separation distances from the tested material to the transmitter and receiver, respectively.  $H$  is the distance from the direct propagation line to the edge of the tested partition [20].....22

Fig. 2.2 Floor layout of polarization dependent measurements at 60 GHz [26]. .....26

Fig. 3.1 Block diagram of the transmitter for the 73 GHz channel sounder. The transmitter consists of the following critical components: a pseudorandom noise sequence generating PCB board; an intermediate frequency synthesizer; a local oscillator frequency synthesizer; an up-converter RF front end box; and a narrowbeam directional horn antenna.....38

Fig. 3.2 The layout of the PN sequence generating board. ....39

Fig. 3.3 Phase Matrix QuickSyn frequency synthesizer for the IF. ....40

Fig. 3.4 Phase Matrix QuickSyn frequency synthesizer for the LO signal. The top box is a model FSW-0020 digital frequency synthesizer and the bottom box contains a frequency doubler and amplifier. ....41

Fig. 3.5 Block diagram of the 73 GHz channel sounder up-converter.....43

Fig. 3.6 Block diagram of the receiver for the 73 GHz channel sounder system. The receiver consists of the following critical components: a pseudorandom noise sequence generating PCB board; an intermediate frequency synthesizer; a local oscillator frequency synthesizer; a down-converter RF front end box; a narrowbeam directional antenna; a low noise amplifier (LNA); a bandpass filter; a quadrature mixer; low pass filters; sliding correlator mixers; and a 2 port digitizer. ....44

Fig. 3.7 Block diagram of the 73 GHz channel sounder down-converter.....44

Fig. 3.8 Transmitter setup for the antenna pattern measurements. The height of the transmit antenna is 2 meters relative to ground.....48

Fig. 3.9 Receiver setup for the antenna pattern measurements. The height of the receive antenna is 2 meters relative to ground.....49

Fig. 3.10 Antenna pattern measurement environment. The majority of surrounding furniture was at a height lower than the TX and RX antennas. ....49

Fig. 3.11 Normalized antenna radiation pattern for vertical-to-vertical polarization. The estimated front-to-back ratio is around 40 dB. However, the converter box blocks some of the power to the back of the antenna, so the actual front-to-back ratio will realistically be lower than that measured. ....51

Fig. 3.12 Normalized antenna radiation pattern for vertical-to-horizontal polarization using 20 dBi gain pyramidal horn antennas at 73 GHz. The XPD for V-H polarization is 31 dB.....51

Fig. 3.13 The 20 dBi receive antenna for antenna pattern measurements attached to a 90° waveguide twister to change the antenna polarization to horizontal. The waveguide twister is attached to a UG-385/U flange on the down-converter box. ....52

Fig. 3.14 Normalized antenna radiation pattern for horizontal-to-horizontal polarization using 20 dBi gain pyramidal horn antennas at 73 GHz. ....	52
Fig. 3.15 Normalized antenna radiation pattern for horizontal-to-vertical polarization using 20 dBi gain pyramidal horn antennas at 73 GHz.....	53
Fig. 3.16 Transmitter located at the indoor MTC1 location with the antenna attached to the up-converter box that is mounted on top of a steerable gimbal, which is mounted on top of a pneumatic mast to reach the height of 2.5 meters. ....	55
Fig. 3.17 Receiver location for one of the MTC1 TX site measurements with the antenna attached to the down-converter box that is mounted on top of a steerable gimbal that is mounted on top of a tripod to reach a height of 1.5 meters. ....	56
Fig. 3.18 Map of the indoor measurement office environment layout on the 9th floor of 2 MetroTech Center with transmitter locations represented as triangles and receiver locations represented as dots. The first TX location is MTC1 in the map and is marked in red. The red dots 1 to 9 represent RX locations for RX1 to RX9 for the measurements conducted with MTC1 as the TX location. The second TX location is MTC2 and is marked in green. The green dots 11 to 22 represent RX locations for RX 11 to RX 22 for the measurements conducted with MTC2 as the TX location. Note that RX 10 does not appear on this map as those measurements were invalid and thus not used for results and analysis. ....	57
Fig. 3.19 Photo of the free space measurement layout in front of the Bern Dibner Library on the MetroTech Commons Courtyard.....	64
Fig. 3.20 Photo of a foliage measurement with the receiver located under the canopy of the cherry tree branches and leaves. The cherry tree leaves are about 7-14 cm when fully blossomed and the cherry flower blossoms had a diameter of 6-12 cm when fully blossomed.....	64
Fig. 3.21 Photo of the foliage measurement ground bounce surface (soil / dirt / gravel) at the MetroTech Commons Courtyard, located between the trees and beneath the branch canopy. ....	65
Fig. 3.22 Map of the TX and RX locations for the outdoor free space measurements. The T-R separation distance between TX1 and RX1 is 10 meters, and an additional 10 meters separation exists for each subsequent RX location. ....	66
Fig. 3.23 Map of the TX and RX locations for the outdoor foliage and ground bounce measurements. The T-R separation distance between TX1 and RX1 is 10 meters, and an additional 10 meters separation exists for each subsequent RX location. The foliage type is cherry trees with leaves and flower blossoms. ....	66
Fig. 3.24 Depiction of the ground bounce scenario through foliage between a TX and RX. ....	70
Fig. 4.1 Sample calibration graph. ....	72
Fig. 4.2 Sample calibration log sheet. ....	74
Fig. 4.3 Sample measurement log sheet. ....	75
Fig. 4.4 Hierarchy structure of the raw measurement data collected during the campaign. ....	77
Fig. 5.1 73 GHz indoor single beam path losses with respect to a 1 meter free space reference distance as a function of T-R separation using 20 dBi (15° HPBW) gain antennas at both the TX and RX. NLOS path losses include LOS NB and truly NLOS measurements. Co-polarized and cross-polarized LOS measured path losses are also shown. The corresponding $n = 2, 3, 4,$ and $5$ path loss exponent path loss models with respect to a 1 meter reference distance are shown for comparison purposes.....	80

Fig. 5.2 73 GHz omnidirectional path loss models with respect to a 1 meter free space reference distance for a typical indoor office environment, synthesized from the 73 GHz directional measurements, using a pair of 20 dBi gain horn antennas with a 15° HPBW. ....84

Fig. 5.3 Cumulative distribution function of the RMS delay spreads measured in the 73 GHz indoor channel for each unique pointing angle combination, using 20 dBi gain, 15° HPBW antennas. ....86

Fig. 5.4 The RMS delay spreads as a function of T-R separation distance obtained for the 73 GHz indoor channel using 20 dBi gain, 15° HPBW antennas. The RMS delay spread is independent of distance. 21 T-R separations distances were measured for V-V antenna polarizations and 9 T-R separation distances were measured for the V-H antenna polarizations. ....86

Fig. 5.5 The mean number of multipath components observed at any unique arbitrary pointing angle (15°) at the RX for different T-R separation distances measured for the 73 GHz indoor office environment measurements using 20 dBi gain, 15° HPBW antennas. 21 T-R separation distances were tested for V-V antenna polarizations and 9 T-R separation distances were measured for V-H antenna polarizations. The multipath components were detected using a peak detection algorithm. ....87

Fig. 5.6 (a), (b) and (d) show typical power delay profiles (PDP) measured in the indoor environment with vertical-to-vertical polarization. (c) shows the PDP with maximum RMS delay spread. The horizontal red line on each PDP represents the computed noise threshold level. Because of the absence of GPS synchronization between the TX and RX, the excess delay is relative to the first arriving multipath above the threshold level. The received power is in dBm / nanosecond. Each PDP corresponds to a recording for a specific TX-RX antenna angle combination in the azimuth and elevation planes. The measurement information including environmental type, T-R separation distance, TX and RX azimuth and elevation, path loss with respect to 1 meter, received power, maximum peak delay, excess delay 10 dB and 20 dB down from the maximum peak, RMS delay spread, and number of multipath components are shown on the right of each PDP. ....90

Fig. 5.7 (a), (b) and (c) show typical power delay profiles (PDP) measured in the indoor environment with vertical-to-horizontal polarization. (d) shows the PDP with maximum RMS delay spread. The horizontal red line on each PDP represents the computed noise threshold level. Because of the absence of GPS synchronization between the TX and RX, the excess delay is relative to the first arriving multipath above the threshold level. The received power is in dBm / nanosecond. Each PDP corresponds to a recording for a specific TX-RX antenna angle combination in the azimuth and elevation planes. The measurement information including environmental type, T-R separation distance, TX and RX azimuth and elevation, path loss with respect to 1 meter, received power, maximum peak delay, excess delay 10 dB and 20 dB down from the maximum peak, RMS delay spread, and number of multipath components are shown on the right of each PDP. ....92

Fig. 5.8 (LEFT): Diagram showing typical power delay profile measured in Manhattan at 28 GHz with energy arriving from a particular AOA, obtained directional 24.5 dBi gain antennas (10.9° HPBW), where cluster terminology is illustrated. Four time clusters may be seen with time durations ranging from 2 ns to 31 ns. (RIGHT): Diagram showing a polar plot measured in Manhattan at 28 GHz, where lobe terminology is illustrated. Five distinct lobes may be seen with various lobe azimuth spreads and AOAs. Each 'dot' is a lobe angular segment, and represents the total integrated received power over a 10° angle [6]. ....93

Fig. 5.9 Typical polar plot measured at 73 GHz at a RX in a NLOS indoor environment using a pair of 20 dBi (15° beamwidth) gain antennas at the. Multiple lobes can be observed where energy arrives in very tight directions over a wide angular spread. This polar plot was obtained from an RX sweep at receiver RX 3 for the MTC 1 transmitter. .94

Fig. 5.10 Histogram of the number of AOA lobes measured in a NLOS office indoor environment for the co-polarized scenario (V-V). The mean and standard deviation for the number of AOA lobes were 2.2 and 1.1, respectively. The number of AOA lobes in a NLOS environment was determined by thresholding the AOA NLOS polar plots using a 15 dB down from maximum peak threshold. 18 TX-RX combinations were measured for these results. ....97

Fig. 5.11 The cumulative distribution function of the mean AOAs in a NLOS environment for the co-polarized scenario. The measured data points are blue circles, and the red line is the cumulative distribution function of a

uniformly distributed random variable between  $0^\circ$  and  $360^\circ$ . 18 TX-RX combinations were measured for these results.....97

Fig. 6.1 73 GHz outdoor single beam path losses as a function of T-R separation relative to a 1 m free space reference distance, using 27 dBi ( $7^\circ$  HPBW) antennas at both the TX and RX. Co-polarized and cross-polarized LOS measured path losses are also shown. The corresponding close-in reference equation lines with respect to a 1 m free space reference distance are shown. Path loss models labeled 'LOS B' correspond to angle combinations in which the TX and RX antennas are pointed perfectly on boresight with each other. 'LOS NB' measurements indicate TX-RX antenna combinations that were not aligned on boresight. Four distinct T-R separation distances were measured: 10, 20, 30, and 40 m. The TX height was at 4.06 meters and RX heights were at 2 meters relative to ground.....107

Fig. 6.2 73 GHz omnidirectional LOS free space propagation path loss models with respect to a 1 meter free space reference distance, synthesized from the 73 GHz directional measurements, using a pair of 27 dBi gain horn antennas with a  $7^\circ$  HPBW. Four distinct T-R separation distances were measured: 10, 20, 30, and 40 m. The TX height was at 4.06 meters and RX heights were at 2 meters relative to ground.....109

Fig. 6.3 Cumulative distribution function for the outdoor free space 73 GHz unique pointing angle measurements for both co- and cross-polarized antenna configurations. T-R separations distances were for 10, 20, 30, and 40 meters, with the TX antenna at a height of 4.06 meters and the RX antennas at a height of 2 meters. TX and RX antennas had 27 dBi of gain with  $7^\circ$  HPBW. ....111

Fig. 6.4 RMS delay spreads as a function of T-R separation distance for the outdoor free space 73 GHz unique pointing angle measurements for both co- and cross-polarized antenna configurations. T-R separations distances were for 10, 20, 30, and 40 meters, with the TX antenna at a height of 4.06 meters and the RX antennas at a height of 2 meters. TX and RX antennas had 27 dBi of gain with  $7^\circ$  HPBW. ....111

Fig. 6.5 Mean number of multipath components detected at the receiver for any arbitrary unique pointing angle combination between the TX and RX antennas for the outdoor free space 73 GHz unique pointing angle measurements for both co- and cross-polarized antenna configurations. T-R separations distances were for 10, 20, 30, and 40 meters, with the TX antenna at a height of 4.06 meters and the RX antennas at a height of 2 meters. TX and RX antennas had 27 dBi of gain with  $7^\circ$  HPBW. ....113

Fig. 6.6 (a), (c) and (d) show typical power delay profiles (PDPs) measured in the outdoor free space environment with vertical-to-vertical and vertical-to-horizontal polarization. (b) shows the PDP with maximum RMS delay spread observed from the outdoor free space measurements. The horizontal red line on each PDP represents the computed noise threshold level. Because of the absence of GPS synchronization between the TX and RX, the excess delay is relative to the first arriving multipath above the threshold level. The received power is in dBm / nanosecond. Each PDP corresponds to a recording for a specific TX-RX antenna angle combination in the azimuth and elevation planes. The measurement information including environmental type, T-R separation distance, TX and RX azimuth and elevation, path loss with respect to 1 meter, received power, maximum peak delay, excess delay 10 dB and 20 dB down from the maximum peak, RMS delay spread, and number of multipath components are shown on the right of each PDP. ....115

Fig. 6.7 73 GHz outdoor foliage attenuation path loss model for co- (V-V) and cross-polarized (V-H) antenna configurations for T-R separation distances of 10, 20, 30, and 40 meters with the TX at a height of 4.06 meters and the RX heights at 2 meters relative to ground, using 27 dBi gain,  $7^\circ$  HPBW antennas. The foliage type was common cherry tree branches, leaves and trunks. ....117

Fig. 6.8 73 GHz outdoor foliage attenuation path loss model in excess of free space path loss for co- (V-V) and cross-polarized (V-H) antenna configurations for T-R separation distances of 10, 20, 30, and 40 meters with the TX at a height of 4.06 meters and the RX heights at 2 meters relative to ground, using 27 dBi gain,  $7^\circ$  HPBW antennas. The foliage type was common cherry tree branches, leaves and trunks. ....117

Fig. 6.9 Cumulative distribution function for the outdoor foliage attenuated 73 GHz unique pointing angle measurements for both co- and cross-polarized antenna configurations. T-R separations distances were for 10, 20,

30, and 40 meters, with the TX antenna at a height of 4.06 meters and the RX antennas at a height of 2 meters. TX and RX antennas had 27 dBi of gain with 7° HPBW. .... 119

Fig. 6.10 RMS delay spreads as a function of T-R separation distance for the outdoor foliage attenuated 73 GHz unique pointing angle measurements for both co- and cross-polarized antenna configurations. T-R separations distances were for 10, 20, 30, and 40 meters, with the TX antenna at a height of 4.06 meters and the RX antennas at a height of 2 meters. TX and RX antennas had 27 dBi of gain with 7° HPBW. .... 119

Fig. 6.11 Mean number of multipath components detected at the receiver for any arbitrary unique pointing angle combination between the TX and RX antennas for the outdoor foliage attenuated 73 GHz unique pointing angle measurements for both co- and cross-polarized antenna configurations. T-R separations distances were for 10, 20, 30, and 40 meters, with the TX antenna at a height of 4.06 meters and the RX antennas at a height of 2 meters. TX and RX antennas had 27 dBi of gain with 7° HPBW. .... 121

Fig. 6.12 (a), (b) and (c) show typical power delay profiles (PDP) measured in the foliage environment for vertical-to-vertical and vertical-to-horizontal antenna polarization configurations. (d) shows the PDP with maximum RMS delay spread in foliage measurement. The horizontal red line on each PDP represents the computed noise threshold level. Because of the absence of GPS synchronization between the TX and RX, the excess delay is relative to the first arriving multipath above the threshold level. The received power is in dBm / nanosecond. Each PDP corresponds to a recording for a specific TX-RX antenna angle combination in the azimuth and elevation planes. The measurement information including environmental type, T-R separation distance, TX and RX azimuth and elevation, path loss with respect to 1 meter, received power, maximum peak delay, excess delay 10 dB and 20 dB down from the maximum peak, RMS delay spread, and number of multipath components are shown on the right of each PDP. .... 124

Fig. 6.13 Ground bounce reflection coefficient versus incidence angle at 73 GHz through foliage for a ground material of soil, dirt, and gravel, using 27 dBi gain, 7° HPBW directional antennas for co- and cross-polarization configurations. T-R separation distances of 10, 20, 30, and 40 meters with the TX at a height of 4.06 meters and the RX heights at 2 meters relative to ground were measured. .... 127

Fig. 6.14 The theoretical and measured ground bounce reflection coefficient versus incidence angle at 73 GHz for vertical-to-vertical polarization through foliage for a ground material of soil, dirt, gravel, and fallen leaves using 27 dBi gain, 7° HPBW directional antennas for co- and cross-polarization configurations. T-R separation distances of 10, 20, 30, and 40 meters with the TX at a height of 4.06 meters and the RX heights at 2 meters relative to ground were measured. Theoretical permittivity values of the soil range, from 1 to 9 in increments of 2 in order to compare theoretical and empirical reflection coefficients. .... 129

# List of Tables

Table 2.1 Penetration loss factors of some common building materials in the COST-231 model [11] [12].	9
Table 2.2 Summary of previous work in indoor millimeter wave channel characterization.	13
Table 2.3 Summary of measured RMS delay spreads using various antenna configurations [16].	15
Table 2.4 Summary of floor penetration factors at various frequency bands [23].	16
Table 2.5 Transmission coefficients of inner building wall partitions and movable partitions at 57.5 GHz [19].	21
Table 2.6 Complex refractive indices of various test materials in office buildings at 57.5 GHz, 78.5 GHz, and 95.9 GHz [20].	23
Table 2.7 Common antenna comparisons [28].	27
Table 2.8 FCC E-band regulations [30].	29
Table 2.9 Antenna standards [29].	31
Table 2.10 The ETSI EN 302 217-3 EIPR limit and minimum antenna gain [31].	32
Table 2.11 Antenna regulations provided by the FCC, ETSI, and those used by NYU WIRELESS in the E-band [5] [29] [30] [31].	33
Table 3.1 Specifications of the Phase Matrix QuickSyn frequency synthesizer for the IF.	40
Table 3.2 Marki mixer (M10408HA) operating specifications and requirements.	41
Table 3.3 Specifications of the Phase Matrix QuickSyn frequency synthesizer for the LO.	42
Table 3.4 73 GHz channel sounder up-converter specifications and requirements.	43
Table 3.5 73 GHz channel sounder down-converter specifications and requirements.	46
Table 3.6 Dimensions of waveguide flange and the flared horn antenna used for antenna pattern measurements.	52
Table 3.7 Channel sounder specifications and settings for the indoor measurements.	56
Table 3.8 TX-RX location combination environment descriptions, T-R separation distances, and calibration and measurement powers used for the indoor measurements.	59
Table 3.9 Initial boresight-to-boresight azimuth angles and elevation angles for the MTC1 transmitter and corresponding receiver locations RX 1 through RX 9. The azimuth angles are relative to the compass shown in Fig. 3.18. The elevation angles are relative to a plane parallel to the floor of the measurement environment, where uptilt refers to positive angles and downtilt refers to negative angles relative to the plane parallel to the floor.	60
Table 3.10 Initial boresight-to-boresight azimuth angles and elevation angles for the MTC2 transmitter and corresponding receiver locations RX 11 through RX 21. The azimuth angles are to the compass shown in Fig. 3.18. The elevation angles are relative to a plane parallel to the floor of the measurement environment, where uptilt refers to positive angles and downtilt refers to negative angles relative to the plane parallel to the floor.	60
Table 3.11 Channel sounder specifications for outdoor propagation measurements.	65
Table 3.12 Summary of the TX and RX locations, environments, and system settings for the outdoor free space and foliage measurements.	67

Table 3.13 The rotation step, sweep type, and initial boresight-to-boresight angles for the free space measurements at receivers RX 1 through RX 4 at the CMN_FS1 TX location. The azimuth angles are with respect to true north. The elevation angles are with respect to horizon where negative angles refer to downtilt and positive angles refer to uptilt.....	67
Table 3.14 The rotation step, sweep type, and initial boresight-to-boresight angles for RX 1 to RX 4 for the CMN TX location. The azimuth angles are with respect to true north. The elevation angles are with respect to horizon where negative angles refer to downtilt and positive angles refer to uptilt.....	70
Table 3.15 Initial TX and RX downtilt angles for different T-R separation distances for measurements 8 through 11, as well as the ground bounce downtilt elevations for measurement 7. ....	70
Table 3.16 TX and RX downtilt angles for different T-R separation distances for measurements 8 through 11. ....	70
Table 5.1 Number of TX-RX location combination used for the V-V and V-H measurement results, and associated environment types whether LOS or NLOS.....	79
Table 5.2 Measurement environment conventions for indoor measurements. ....	80
Table 5.3 Path loss exponents and shadowing factors with respect to a 1 m free space reference distance computed from the 73 GHz indoor office environment directional (unique pointing angle) measurements, computed for both co-polarized (V-V) and cross-polarized (V-H) scenarios. ....	84
Table 5.4 Path loss exponents and shadowing factors with respect to a 1 m free space reference distance synthesized using the 73 GHz indoor office environment directional measurements, computed for both co-polarized (V-V) and cross-polarized (V-H) scenarios. ....	84
Table 5.5 Summary of the mean number of multipath components observed at any unique arbitrary pointing angle (15°) at the RX for different T-R separation distances measured for the 73 GHz indoor office environment measurements, using 20 dBi gain, 15° HPBW antennas. 21 T-R separation distances were tested for V-V antenna polarizations and 9 T-R separation distances were measured for V-H antenna polarizations. The multipath components were detected using a peak detection algorithm. ....	88
Table 5.6 Mean and standard deviation of spatial AOD (lobe) parameters in a LOS and NLOS office environment for the co-polarized scenario (V-V). There were 3 LOS and 18 NLOS environments measured to produce these statistics. ....	99
Table 5.7 Mean and standard deviation of spatial AOA (lobe) parameters in a LOS and NLOS office environment for the co-polarized scenario (V-V). There were 3 LOS and 18 NLOS environments measured to produce these statistics. ....	99
Table 5.8 Mean and standard deviation of spatial AOA (lobe) parameters in a LOS and NLOS office environment for the cross-polarized scenario (VH). There were 3 LOS and 9 NLOS environments measured to produce these statistics. ....	99
Table 5.9 The parameters for the partition-dependent directional antenna model including the T-R separation distance, free space path loss, observed path loss, partition loss, and the partition type and number, for co-polarized antennas. ....	101
Table 5.10 Partition attenuation values for the 73 GHz indoor channel measurements for common office building partitions, using co-polarized antennas, obtained from the directional partition-dependent model.....	103
Table 5.11 The parameters for the omnidirectional antenna partition-dependent model including the T-R separation distance, free space path loss, actual path loss and the partition type and number, for co-polarized antennas.....	103
Table 5.12 Partition attenuation values for 73 GHz indoor measurements for common office building partitions, for co-polarized antennas using the omnidirectional partition-dependent model.....	103

Table 6.1 Path loss exponents and shadowing factors with respect to a 1 m free space reference distance obtained from the 73 GHz outdoor free space directional (unique pointing angle) measurements, computed for both co-polarized (V-V) and cross-polarized (V-H) scenarios. The TX height was at 4.06 meters and RX heights were at 2 meters relative to ground. TX and RX antennas had 27 dBi of gain with 7° HPBW. .... 110

Table 6.2 Omnidirectional path loss exponents and shadowing factors with respect to a 1 m free space reference distance synthesized using the 73 GHz free space directional measurements, computed for both co-polarized (V-V) and cross-polarized (V-H) scenarios. TX and RX antennas had 27 dBi of gain with 7° HPBW..... 110

Table 6.3 Summary of the mean number of multipath components detected at the receiver for any arbitrary unique pointing angle combination between the TX and RX antennas for the outdoor free space 73 GHz unique pointing angle measurements for both co- and cross-polarized antenna configurations. T-R separations distances were for 10, 20, 30, and 40 meters, with the TX antenna at a height of 4.06 meters and the RX antennas at a height of 2 meters. TX and RX antennas had 27 dBi of gain with 7° HPBW. .... 113

Table 6.4 Summary of the mean number of multipath components detected at the receiver for any arbitrary unique pointing angle combination between the TX and RX antennas for the outdoor foliage attenuated 73 GHz unique pointing angle measurements for both co- and cross-polarized antenna configurations. T-R separations distances were for 10, 20, 30, and 40 meters, with the TX antenna at a height of 4.06 meters and the RX antennas at a height of 2 meters. TX and RX antennas had 27 dBi of gain with 7° HPBW. .... 121

Table 6.5 Magnitude of ground bounce reflection coefficients obtained from the 73 GHz measurements through foliage for a ground material of soil, dirt, and gravel, using 27 dBi gain, 7° HPBW directional antennas for co- and cross-polarization configurations. T-R separation distances of 10, 20, 30, and 40 meters with the TX at a height of 4.06 meters and the RX heights at 2 meters relative to ground were measured. Magnitude of theoretical Fresnel reflection coefficient when  $\epsilon_r = 7$ ..... 127

# **Chapter 1 Background on Millimeter-Wave Radio Propagation Channels**

## **1.1 Project Overview**

The goal of this research is to study the indoor and outdoor propagation channel characteristics in the 73 GHz millimeter-wave (mmWave) band in a typical office environment and outdoor courtyard setting for both co- and cross-polarized antenna configurations. To simulate current indoor wireless access networks, the transmitters were elevated to the ceiling (2.5 m) to emulate wireless access routers, and the receivers were at cubicle and human level heights (1.5 m). Along with the indoor study were outdoor free space, ground bounce, and foliage measurement studies for co- and cross-polarized antenna configurations. The outdoor courtyard study had the transmitter at lamppost level (4.06 m) to mimic future mmWave base station deployment, and the receivers were at a common foot traffic height of 2 meters. The four stages necessary for this research work included a thorough measurement plan, the collection of measurements and their configurations, the post-processing and data analysis of collected measurements, and the analysis of results.

The measurement plan consisted of two main parts: the indoor channel propagation measurement plan and outdoor channel propagation measurement plan. The indoor measurement description in Chapter 3 describes the single-floor channel propagation measurements, although future work will include multi-floor measurements. The outdoor propagation measurements that included free-space, foliage, and ground bounce scenarios, are also described in Chapter 3 of this report. Overall, the indoor measurements and results are meant to help us better understand 73 GHz propagation in an office environment, while the outdoor measurements and results are meant to help us understand the 73 GHz propagation channel in a common courtyard area.

For the indoor measurements, the single-floor study considered many transmitter (TX) and receiver (RX) combination links to generate models, in addition to understanding partition losses for common indoor office obstructions (e.g. glass doors, metal doors, elevators, plasterboard walls, etc.). The received power acquired from indoor measurements was used to calculate path loss that can then be compared with theoretical free space path loss in order to compute the penetration loss of different materials and obstructions in a common office environment. These computed results were used to create a partition-based path loss model.

Initial multi-floor channel propagation measurements were conducted on two adjacent floors in the same office building. These measurements were performed to study the floor penetration characteristics at 73 GHz for frequency reuse in an office building environment. However, no results were obtained for these measurements since the power observed at the receiver was too weak for successful signal acquisition. More extensive future work will be done to re-test this scenario.

For the outdoor measurements, four evenly spaced (10 m) receiver locations were tested in free space and four evenly spaced (10 m) receiver locations were tested in cherry tree foliage. The results allowed us to validate 73 GHz free space propagation by generating both directional and omnidirectional models. The foliage measurements allowed us to determine foliage attenuation rates as well as ground bounce reflection coefficients. The results will be helpful for modeling the 73 GHz indoor and outdoor channels with the use of computer simulation tools such as a ray-tracer.

## **1.2 Report Overview**

This technical report contains seven sections. This first Chapter, the Introduction, includes the project and report overview along with the motivation in the following subsection. Chapter

Two is a literature review of previous works used to characterize indoor environments at various frequency bands. The purpose of Chapter 2 is to help understand empirical results from real-world measurements and the subsequent analysis by researchers around the world. It is also meant to provide an understanding of current mmWave research, and specifically E-band specifications and requirements. The literature review additionally includes path loss and partition loss studies, RMS delay spread studies, and material reflection and penetration studies. Chapter Three describes the measurement equipment and hardware used such as the broadband sliding correlator channel sounder, and the corresponding processing algorithms used in recovering total received power and other data. Chapter Three also presents the measurement campaign details for the different indoor and outdoor measurement scenarios and configurations as well as site layouts and locations. Chapter Four explains the post-processing procedure as well as a description of the final data set. Chapter Five and Chapter Six present the data analysis, results, and models for the indoor and outdoor measurements, respectively. Chapter Seven is the conclusion of the project and technical report.

### **1.3 Motivation for Indoor and Courtyard Millimeter-Wave Propagation Channel Modeling**

Wireless communications have in recent years experienced an overwhelming demand for broadband communications, leading to a great demand for higher data rates and reliable wireless networks for various applications. The wireless industry foresees the need for more available spectrum in order to accommodate broadband communications for the next generation of wireless communications and devices. Additional spectrum allocation is one attractive potential solution to meet the rising demand, along with the development of new networks that are more

flexible with the help of small cells and HetNets, to achieve optimal network performance with faster data rates [1].

To meet the ever-increasing market demand, research academics and industry are now considering scaling up to the mmWave spectrum, that is vastly underutilized and can provide a massive amount of raw bandwidth, an attractive solution to today's spectrum congestion [2]. The fourth generation of wireless communication networks, Long-Term Evolution (LTE), has improved the performance in current wireless networks by providing up to 100 Mbit/s data rates via spatial multiplexing access technologies such as Multiple-Input-Multiple-Output (MIMO). It is however clear that 4G LTE will not enable multi-Gbps data rates, thus several research centers around the world are actively investigating the properties of ultra-wideband mmWave channels for broadband mobile, backhaul, and indoor communications.

The mmWave bands correspond to the radio spectrum that spans frequencies between 30 GHz and 300 GHz with wavelengths between 10 mm and 1 mm. The E-band is located between 71 to 76 GHz and 81 to 86 GHz, and has been under the supervision of the Federal Communications Commission (FCC) since 2003 for high-density fixed wireless services in the United States [3]. These light-licensed bands can offer up to 10 GHz of available bandwidth, with two contiguous sections of 5 GHz that can be used to dramatically increase the network capacity. A complete and accurate understanding of the radio propagation characteristics at E-band for indoor and outdoor environments is necessary to design future networks and for the successful deployment of mmWave communication systems. Fig. 1.1 shows the atmospheric attenuation in the microwave and mmWave bands. The first green circle denotes the atmospheric attenuation in the E-band range. At 73 GHz, the atmospheric attenuation is close to 0.45 dB / km, or 0.09 dB / 200 m, which is slightly worse than that of currently used cellular bands with cell

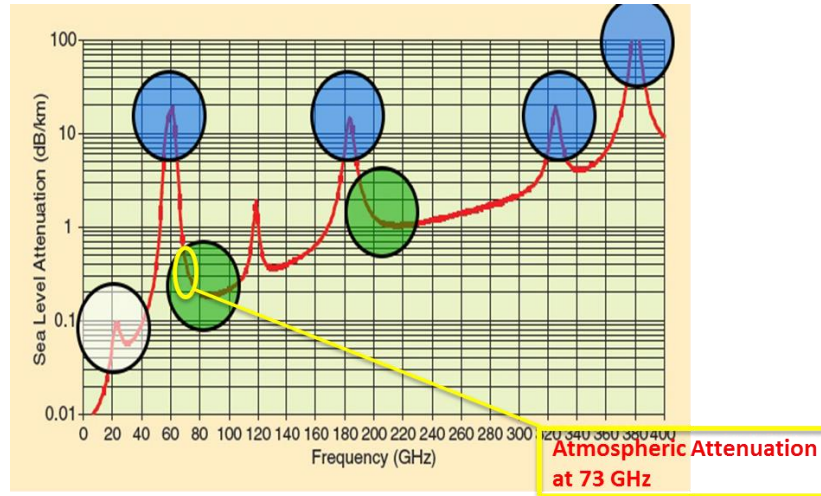


Fig. 1.1 The atmospheric attenuation at microwave and mmWave frequency bands. The white circle denotes frequencies with very low attenuation used for current cellular, the green circles represent frequency bands for potential backhaul and mobile access technologies with low atmospheric attenuation for short cell radii, and the blue circles show higher atmospheric attenuation bands. The yellow circle points out the atmospheric attenuation at 73 GHz and is about 0.09 dB / 200 meters [4].

sizes of several hundred meters. A cell radius of 200 meters is predicted for future small cell networks [5].

The indoor channel propagation characteristics at E-band must be thoroughly studied to help with the design of future indoor and outdoor mmWave communication systems, and these studies will help to predict network capacities and outage probabilities. Channel impulse responses otherwise known as power delay profiles (PDPs) are measured for propagation studies in order to understand the channels of interest, in both indoor and outdoor environments. Thousands of PDPs are normally recorded in order to build a database of measurements for multiple scenarios and settings that are used to build accurate models from the data. The collected measurements and subsequently processed data is used to obtain statistical spatial and temporal channel models that can simulate the indoor or outdoor channel, and are then delivered to radio-system engineers for proper radio-system design. Such models have already been obtained for wideband channels in dense urban environments at 28 GHz and 73 GHz [6] [7].

Office buildings are typically represented by a busy network traffic, which leads to a demand of higher data rates, poor system capacity, and an unstable network connection. Office buildings are usually found to have similar floor layouts and typical construction materials, such as soft partitions, elevators, furniture, etc. To study the propagation channel, we should consider the effects of office obstructions, which may block the free space propagation channel. In addition, office buildings have multiple floors that require careful consideration of interference from adjacent floors. The signal transmission from outdoor-to-indoor environments also needs to be considered as an integral part of the indoor channel modeling process, but is not investigated as part of this study. Understanding propagation in courtyard areas with high levels of foot traffic, obstructions, and foliage is also important for network design, as large crowds of people tend to group in such areas and can result in large bandwidth demands and the need for high data rates. Modeling the free space, foliage, and ground bounce effects of mmWave transmissions in such an environment will help to create robust networks and stable systems that will meet the demand for broadband data.

## **Chapter 2 Literature Review of Past Indoor and Foliage Measurements**

### **2.1 Introduction**

This chapter presents a literature review of previous indoor and outdoor foliage propagation studies performed, that investigated channel characteristics and properties with the goal of producing channel models and statistical distributions that embody the measured channels. The key aspects include indoor single floor propagation measurements, multi-floor propagation measurements, building material reflection measurements, antenna pattern diversity measurements, the study of foliage scattering effects, and the use of ray-tracing methods. The goal of this chapter is to provide a comprehensive literature review of the research on the works and measurements conducted by previous researchers around the world.

### **2.2 Indoor Single Floor Propagation Study**

#### **2.2.1 Path Loss Studies**

Bensebti, McGeehan, and Beach studied indoor multipath radio propagation characteristics at 60 GHz in 1991 [8]. At that time, broadband services via high-speed fiber optics were considered but researchers also started looking into the millimeter wavelength region for potential applications. A 60 GHz channel sounder was used to measure the path loss in typical indoor and outdoor multipath environments at the University of Bristol. The transmitted signal was a pseudorandom binary sequence with a length of 2047 chips, clocked at a rate of 100 MHz and transmitted at a center frequency of 59.9 GHz. At the receiver, the signal was down converted to 1 GHz and passed to a quadrature correlator to extract the in-phase and quadrature components. The time resolution of the channel sounder was 10 ns. The antennas used in the system were narrow beamwidth semi-omnidirectional horn antennas, and bi-reflector omnidirectional

antennas, all set at a height of 1.5 m relative to the ground. Three sites were measured: a 3 m x 30 m corridor, a medium size laboratory, and a large laboratory with 15 m x 30 m dimensions. In the measurements, the receiver remained stationary and the transmitter was moved over a regularly spaced grid. The measured received power along the corridor in the line-of-sight (LOS) environment showed that the narrowband signal attenuated rapidly with occasional deep fades. In severely obstructed areas, the distribution of the propagation paths diverged from simple theoretical models, whereas the propagation power distribution in LOS conditions converged towards an exponential distribution, and the number of paths followed a Poisson distribution. The RMS delay spreads were dependent upon the specific site size, varying from 10 to 40 ns.

They modeled the multipath propagation medium as an absorptive and dispersive time-varying delay line with  $L$  paths as a function of time and location [8]. The time-variant complex discrete impulse response can be written as:

$$h(t) = i(t) + jq(t) = \sum_{k=1}^L a_k \delta(t - \tau_k) \exp(j\theta_k) \quad (2.1)$$

where  $a_k$  is the amplitude,  $\tau_k$  is the delay, and  $\theta_k$  is the relative phase of the  $k^{th}$  path. The signals  $i(t)$  and  $q(t)$  are the in-phase and quadrature components of the complex impulse response.

Motley and Keenan studied the signal coverage at 900 MHz and 1700 MHz inside a building between adjacent floors [9]. They fixed the receiver dipole antenna at the center of the office block and moved the transmitter in the building. They modified the path loss equation by adding a floor factor  $F$  and multiplying the number of floors that the signal traversed,  $k$ , to yield the following path loss equation:

$$PL + k \times F = PL_{free\ space}(d_0) + 10n \log_{10} \left( \frac{d}{d_0} \right) \quad (2.2)$$

Their measurement data showed a 6 dB decay in signal strength per floor, and at 1700 MHz the path loss was 5 dB higher than at 900 MHz, which agrees with the theoretical difference caused by the relationship between frequency and antenna effective area. The transmit power was 22.4 dBm (173.8 mW) and 26.8 dBm (478.6 mW) at 900 MHz and 1700 MHz, respectively.

Motley's model estimated the path loss between transmitter and receiver by a free space component ( $L_0$ ) and additive loss in terms of wall attenuation factors ( $F_{wall}$ ) and floor attenuation factors ( $F_{floor}$ ), which can be expressed as [9]:

$$L = L_0 + 20 \log_{10} \left( \frac{d}{d_0} \right) + n_{wall}F_{wall} + n_{floor}F_{floor} \quad (2.3)$$

The attenuation factor of walls and floors varied largely from 10 to 40 dB, showing a high dependence on indoor construction materials for the model. Seidel and Rappaport [10] expanded the utility of this attenuation factor model, and demonstrated that attenuation factors and floor attenuation factors could be used to very rapidly and accurately predict indoor propagation in a wide range of buildings such as grocery stores, retail stores, and large office buildings. Typical values for partitions at 914 MHz were given in [10].

According to the COST-231 model, some penetration loss factors of the common materials in buildings are shown in Table 2.1. In the table,  $L_e$  is the path loss through the external wall at normal incidence.  $L_g$  is the additional loss due an external wall incurred at a grazing incidence

Table 2.1 Penetration loss factors of some common building materials in the COST-231 model [11] [12].

Material	Frequency	$L_e$	$L_{ge}$	$L'_{ge}$	$L_i$
Wood; Plaster	900 MHz	4	N/A	4	4
Concrete w/ Windows	1.8 GHz	7	~20	6	10
Residential	2.5 GHz	6.2	~10	6.1	3

$(\theta=\pi/2)$  in dB,  $L_{ge} = L_g(1 - \cos \theta)^2$  in dB,  $L'_{ge}$  is the average value in dB, and  $L_i$  is the loss per internal wall in dB [11] [12].

Anderson *et al.* have conducted measurements focused on indoor wideband partition loss at 2.5 GHz and 60 GHz using a broadband vector sliding correlator channel sounder to record power delay profiles [13]. In the 2.5 GHz measurements, both the transmitter and receiver antennas were vertically polarized omnidirectional biconical antennas with 6 dBi of gain. The transmit power before the antenna was 0 dBm in order to emulate the same operating power of 2.4 GHz WLAN networks. In the 60 GHz measurements, vertically polarized pyramidal horn antennas with 25 dBi of gain and a first-null beamwidth of  $50^\circ$  were used at both the transmitter and receiver. The transmit power was -10 dBm in order to maintain the linear operation of the power amplifier at the transmitter and to avoid saturating the low noise amplifier of the receiver at short distances. An EIRP of 15 dBm was comparable to the power of a femtocellular system that allowed for the study of a single-cell-per-room network. Anderson *et al.* selected eight transmitter locations and 22 receiver locations with T-R separation distances ranging from 3.5 to 27.4 meters on the same floor in a modern office building with a variety of obstructions in the signal path [13]. The transmitter and receiver locations were chosen to be representative of a wide range of typical office femtocellular propagation environments. The height of the transmitter and receiver antennas was 1.2 meters relative to the ground, with an exception at one receiver location where the antennas were 2.4 meters above the ground. A linear track was used to measure the received power level at each receiver location. Perpendicular and parallel track measurements were conducted. The perpendicular track measurements were set at each RX location with the track perpendicular to the direction of transmitted energy. The parallel track measurements were set with the track parallel to the direction of transmitted energy [13]. For

both perpendicular and parallel track measurements, power delay profiles were recorded at 40 positions along the track, in steps of  $\frac{\lambda}{4}$  where  $\lambda$  was the wavelength of the frequency measured.

Anderson *et al.* analyzed separately the large-scale path loss and partition-based path loss based on the measured data collected at 22 RX locations [13]. By using a minimum mean square error fit, the path loss exponent at 2.5 GHz was found to be 2.4 with a standard deviation of 5.8, and at 60 GHz the path loss exponent was 2.1 with a standard deviation of 7.9 dB, both with respect to a 1 meter free space reference distance. The site-specific partition-based path loss is an important factor in designing indoor wireless networks. The researchers studied five common types of partitions in an office environment, namely drywall, whiteboards, clear glass, mesh glass, and clutter. All partition attenuation values were normalized to decibels per centimeter of the material thickness for comparison. The results showed that the partition loss is a frequency-dependent parameter and for drywall, whiteboard, clear glass, and clutter, the values of partition loss were lower at 60 GHz than those at 2.5 GHz. However, the partition loss caused by mesh glass is higher at 60 GHz as compared with the value at 2.5 GHz. The reason for the general decrease in partition loss with the increase in frequency is that at 60 GHz the first Fresnel zone is within a closer distance than at 2.5 GHz, thus fewer partitions will perturb the LOS signal.

Skidmore *et al.* developed a software application for indoor channel propagation environment coverage prediction named SMT Plus [14]. SMT plus was developed as a tool for path loss prediction as a function of distance along with the number and type of partitions in an indoor environment [14]. The performance of the simulated wireless communication systems at any location in the environment was judged on the basis of coverage area, signal-to-noise ratio, and signal-to-interference ratio. In an office environment, a LOS path between a transmitter and receiver rarely exists. Instead, signals reach the receiver after reflecting off of walls and other

obstructions such as doors, windows, and office furniture. The movement of equipment and users also affects the propagation channel, resulting in a continually changing and difficult-to-predict propagation environment. Multipath and shadowing effects are among the greatest obstacles that in-building wireless systems need to deal with. In narrowband communication systems, the existence of multipath signal components causes Rayleigh fading to be observed at the receiver. Shadowing is caused by obstructions in the environment, but is generally associated with signal blockage due to large, immobile objects such as walls or large office furniture. The variations in received signal strength due to shadowing tend to occur slowly with changes in receiver location. Interference is another major problem that indoor wireless systems need to overcome. In wideband communication systems, multipath delays affect the received signal quality. Digital wireless communication systems are susceptible to interference as a result of multiple signal components arriving at the same time delays at the RX. A signal component may arrive at the receiver at the same time instant as a component from a previously transmitted signal. The interference between signal components is known as inter-symbol interference (ISI). ISI is known to increase with higher data rates, thus limiting the maximum data rate for any un-equalized wireless communication system. When two users are using the same channel and in relatively close proximity, co-channel interference occurs. Co-channel interference can be reduced during the design phase of in-building systems through optimal channel assignment and access point location strategies. Such strategies aim to minimize the chance that multiple users will interfere with each other.

The Site Modeling Tool (SMT) is a graphical propagation prediction tool relying on actual building layouts and materials, combined with statistical propagation models to gauge wireless system performance [14]. The tool assumes an omnidirectional antenna for performance

prediction. SMT Plus is an upgraded version to the original SMT software. While SMT Plus

Table 2.2 Summary of previous work in indoor millimeter wave channel characterization.

Researcher	Ref.	Freq.	Focus	Measurement Setting	Major Results
Bensebti <i>et al.</i>	[8]	60 GHz	Received power; path loss; RMS delay spread	One corridor; mid-size lab; A large lab.	Narrowband signals attenuate rapidly along corridors; Power in LOS conditions follows an exponential distribution; Delay spread depends on environment sizes.
Motley and Keenan	[9]	900 MHz; 1.7 GHz	Penetration Loss	Office building	$L = L_0 + 20 \log_{10}\left(\frac{d}{d_0}\right) + n_{wall}F_{wall} + n_{floor}F_{floor}$ Attenuation factors highly depend on environment.
Anderson <i>et al.</i>	[13]	2.5 GHz; 60 GHz	Partition loss	Office building	Path loss exponent of 2.4 at 2.5 GHz and 2.1 at 60 GHz.
Skidmore <i>et al.</i>	[14] [15]	914 MHz	Floor attenuation factor; Partition attenuation factor	Office buildings	SMT Plus, a software tool developed for indoor propagation prediction and system design.
Siamarou <i>et al.</i>	[16]	62.4 GHz	RMS delay spread; received signal level	Corridors with different wall materials	Received power decreases as RMS delay spread increases; RMS delay spread increases as T-R separation distance increases.
Durgin <i>et al.</i>	[17]	5.8 GHz	Floor attenuation factor	Offices and houses	MMSE provides optimal prediction of each partition loss. $P_R = P_T + G_T + G_R + 20 \log_{10}\left(\frac{\lambda}{4\pi d}\right) - \sum_{i=1}^N X_i$ where $X_i$ is the attenuation of the $i^{th}$ partition.
Chung and Bertoni	[18]	5.2 GHz	Single floor and multiple floor transmission, outdoor-to-indoor measurements	Office building	$PL = A - 10u \log R,$ where $A$ is a fixed constant, $u$ is the path loss index, and $R$ is the T-R separation distance Horizontal polarization results in a lower path loss exponent than vertical polarization.
Sato <i>et al.</i>	[19]; [20]; [21]	57.5 GHz; 78.5 GHz; 95.9 GHz	Reflection coefficients	Lab, with specific test materials	Transmission coefficients of walls and partitions, with refractive indices given for various frequencies.
Oestges and Paulraj	[11]	2.5 GHz	Wall penetration loss	Outdoor-to-indoor	Determined path loss models similar to the COST-231 approach for various building materials such as wooden walls, concrete, stucco, and mixed materials [11] [22].

provided ways to reconstruct three dimensional radiation patterns of transmit and receive antennas, antenna polarization effects were not included as options with the software package.

Skidmore also proposed four models in his thesis [15]. These were generally referred to as the Distance Dependent Single Floor, Distance Dependent Multi-floor, Partition Dependent, and Distance Dependent with Floor Attenuation models. Each model was a series of point-to-point path loss prediction equations that take into account the operating parameters of transmitting base stations and the physical building environment. Each partition type had an associated partition attenuation factor (*PAF*), which was a measure of the amount of loss in dB that occurs when a signal passes through a single partition of the given type. The larger the *PAF* value, the greater the attenuation of the signal. The distance dependent with floor attenuation model was valid for multi-floor simulations only. The model used an additional parameter known as the floor attenuation factor (*FAF*) to account for floor attenuation. The value of *FAF* depends on the number of floors separating the transmitter and the receiver. In Skidmore's thesis, he lists the *FAF* values for up to five floors. The path loss in dB can be expressed with the floor attenuation factor as [15]:

$$\overline{PL}(d)[dB] = PL(d_0) + 10 \times n \times \log_{10} \left( \frac{d}{d_0} \right) + FAF \quad (2.4)$$

where  $PL(d_0)$  is the free space path loss at a known reference distance  $d_0$ ,  $n$  is the path loss exponent,  $d$  is the T-R separation distance, and *FAF* is the floor attenuation factor in dB. Table 2.2 summarizes the work presented in [15] in addition to the other mmWave channel propagation measurements and results presented in this Chapter.

### 2.2.2 Delay Spread Studies

Siamarou *et al.* measured the 62.4 GHz indoor channel while focusing on RMS delay spread and received signal strength [16]. Measurements were conducted using a vector network

analyzer (VNA) channel sounding system. Six LOS TX-RX location combinations in corridors were tested for these experiments. An external 100 MHz oven-controlled crystal oscillator was used to synchronize the phase of the transmitter and receiver. The two different antenna configurations used consisted of a pair of vertically polarized standard horn antennas with 10 dBi of gain and 55° HPBW and 69° HPBW in the azimuth and elevation planes respectively, at the TX and RX. The second antenna configuration consisted of a standard horn antenna at the TX and an omnidirectional antenna at the RX with 6 dBi of gain and 6.5° HPBW in the elevation plane. Four measurement locations were in corridors with different types of wall materials (e.g. metallic sheet, plasterboard, thin layer foil, unsmooth wooden walls, etc.), and two locations were chosen inside small rooms with brick and concrete block walls, one of which had furniture and the other was empty. The transmitter was fixed at one end of the corridor and the receiver was moved around the measurement environment to record the received signal power and delay spread. To avoid a dynamic time-varying channel where people are moving, researchers performed these measurements at night to ensure channel stability. From the data collected, cumulative probability distribution functions of the multipath delay spreads at each location were

Table 2.3 Summary of measured RMS delay spreads using various antenna configurations [16].

Measurement Environment	Antenna Configurations	Measured RMS Delay Spread (ns)		
		Median	Standard Deviation	Maximum
Corridor A with widows	Horn-Horn	31.59	17.69	63.26
	Horn-Omni	36.75	18.53	67.84
Corridor B with no window	Horn-Horn	31.72	17.70	62.53
	Horn-Omni	32.40	18.55	65.81
Small Room E	Horn-Omni	N/A	5.94	N/A
Small Room F	Horn-Omni	N/A	5.94	N/A
Corridor C	Not Reported in the paper			
Corridor D	Not Reported in the paper			

plotted and Table 2.3 shows the comparison of median and maximum RMS delay spreads measured at each location for the two types of antenna configurations.

The researchers also reported the relationship between the RMS delay spread as a function of the received power and T-R separation distance [16]. It was shown that as the received power decreased, the RMS delay spread increased, which shows an inverse relationship of the two parameters. As the T-R separation distance increased, the RMS delay spread also increased, showing a proportional relationship. Additionally, the researchers concluded that the RMS delay spread data collected from two small rooms (with and without furniture) did not show significant dependence on room furniture and fixtures. Based on measurements reported in other papers, room configurations including furniture and interior constructions can be attributed to differences in delay spread.

### 2.3 Indoor Multi-Floor Studies

In the ITU Recommendation ITU-R P.1238-7 [23], the site-general models briefly describe the loss through multiple floors for the consideration of frequency reuse between floors. The

Table 2.4 Summary of floor penetration factors at various frequency bands [23].

Frequency	Transmission loss through multiple floors in various environment (in dB, $n$ is the number of floors)		
	Residential	Office	Commercial
900 MHz	N/A	9 ( $n = 1$ ) 19 ( $n = 2$ ) 24 ( $n = 3$ )	N/A
1.8-2 GHz	$4n$	$15+4(n-1)$	$6+3(n-1)$
2.4 GHz	10 (per wall in apartment) 5 (in house)	14	N/A
3.5 GHz	N/A	18 ( $n = 1$ ) 26 ( $n = 2$ )	N/A
5.2 GHz	13 (per wall in apartment) 7 (in house)	16 ( $n = 1$ )	N/A
5.8 GHz	N/A	22 ( $n = 1$ ) 28( $n = 2$ )	N/A

recommendation listed several floor penetration loss factors at various frequency bands in residential, office, and commercial scenarios. Table 2.4 shows the penetration losses at microwave frequencies. The floor penetration loss values shown in Table 2.4 were obtained from multiple propagation measurements. Some of the important work behind this is now discussed.

Chung and Bertoni measured the indoor channel frequency response centered at 5.2 GHz using a continuous wave to determine path loss and RMS delay spread [18]. The continuous wave was generated by a signal generator with a transmit power of 10 dBm, and transmitted with a vertically polarized omnidirectional collinear antenna. The receiver antenna was also a vertically polarized omnidirectional collinear antenna, and the received signal was fed into a spectrum analyzer remotely controlled by a laptop computer. In the single floor path loss measurements, both the transmitter and receiver were at a height of 1.5 meters above the floor and the antennas remained vertically polarized, while multi-floor measurements had the antennas horizontally polarized where the center of each antenna was set to 0.95 meters relative to floor level.

In the path loss measurements, the receiver antenna was rotated around the 360° azimuth plane, and received power was measured in angular increments and averaged. Then the data was fit to the path loss formula shown below:

$$PL = A - 10u \log R \quad (2.5)$$

where  $A$  denotes a fixed constant,  $u$  is the path loss index, and  $R$  is the T-R separation distance. This path loss formula is slightly different from the commonly used large-scale path loss equation in [24]. However, the path loss exponent values agreed well with the theoretical free space path loss index. Horizontal polarization results showed a slightly lower value in path loss index than results obtained from vertically polarized antennas.

## 2.4 Outdoor-to-Indoor Propagation Studies

Chung and Bertoni also conducted outdoor-to-indoor measurements in a modern office building and several houses using a continuous wave signal with a transmit power of 10 dBm, using a pair of vertically polarized omnidirectional collinear antennas at 5.2 GHz [18]. The measurement results showed that the path loss from outdoor-to-indoor was not dependent on the polarization, and the exterior wall usually caused greater attenuation than interior walls.

Durgin and Rappaport also conducted outdoor-to-indoor measurements around houses at 5.85 GHz using a spectrum analyzer with a transmitter and receiver at different heights [17]. The transmitter consisted of a signal generator, an amplifier, and a discone antenna, while the receiver consisted of an omnidirectional quarter-wave monopole antenna. A partition-based outdoor-to-indoor path loss model for received power was extracted as follows:

$$P_R = P_T + G_T + G_R + 20 \log_{10} \left( \frac{\lambda}{4\pi d} \right) - \sum_{i=1}^N X_i \quad (2.6)$$

where  $P_R$  is the received power,  $P_T$  is the transmitted power,  $G_T$  and  $G_R$  are the gains of the transmit and receive antennas, respectively.  $X_i$  is the attenuation value computed for the  $i^{\text{th}}$  partition intersected from a straight line between the transmitter and receiver,  $d$  is the T-R separation distance, and  $\lambda$  is the wavelength of the transmitted signal. The model worked well for T-R separation distances less than 50 meters. However, a site-specific database is needed in order to predict the outdoor-to-indoor transmission loss.

Oestges and Paulraj performed outdoor-to-indoor measurements at 2.5 GHz in two cities, Seattle and San Francisco, with the focus on wall material penetration loss with respect to angle of incidence, and receiver height [11]. Their measurements produced results displayed in Table 2.1 that were generated similar to the COST-231 approach [22]. Their model showed the significance of the incidence angle and the access point height on the measured path loss.

## 2.5 Reflection, Refractive, and Transmission Coefficient Studies

In 1997, researchers in Japan studied the reflection and transmission characteristics of typical office interior structures at 57.5 GHz [19]. They measured the reflection and transmission coefficients of two types of walls, the floor, the ceiling, windows, and other partitions. A comparison was made between the measured results and the reflection characteristics estimated using the Fresnel reflection coefficients assuming multilayered structures. The measurement system in this study included a transmitter, a receiver, and a vector network analyzer that operated in the 57 GHz to 58 GHz frequency range. Both linearly and circularly polarized antennas were used during measurements. In the paper the researchers did not supply any additional information regarding the transmitter and the receiver, nor did they provide the gains of the antennas used. The transmit and receive antennas used each had a beamwidth of 5°. A common 55 GHz reference signal was used to phase-lock the transmitter and receiver, while the intermediate frequency between 2-3 GHz was generated by a VNA that was able to detect the relative amplitude and phase of the received IF signal.

The reflection coefficient measurements were conducted in the specular reflection direction at which the angle of incidence equals the angle of reflection. The value of the reflection coefficient was obtained by comparing the received amplitude from the surface of the test material with the received amplitude from an aluminum plate that had an absolute reflection coefficient value of one.

In the transmission coefficient measurements, the transmitter and receiver were placed on the opposite sides of the test materials each at a distance of 1.5 meters. The direction of propagation was perpendicular to the surface of the test material and the transmission coefficient was calculated based on the comparison of received amplitude with and without the test material.

In the study, two types of walls were selected to represent the typical wall structure of an indoor environment. The measured results of reflection coefficients for perpendicular and parallel polarization scenarios showed that the variation of the reflection coefficient as a function of incidence angle resulted from the multilayered structure. Since the interior structure of the indoor environment often involves multilayered obstructions, it is important to use a multilayer model as a function of the wavelength, the thickness of the material, the number of layers, and the refractive index of each layer. The refractive index is an intrinsic property of a medium, and is given by the ratio of the speed of a propagating electromagnetic wave in free space to the speed of that same propagating wave in the medium. The reflection coefficient describes the reflected E-field in terms of the incident E-field of a propagating wave, and always has a magnitude value that is between 0 and 1. A negative value implies a phase shift of 180° on reflection, but the magnitude is always less than or equal to 1, and is expressed in [19] as:

$$R_{S_{i,i+1}} = \frac{\sqrt{n_i^2 - \sin^2 \theta} - \sqrt{n_{i+1}^2 - \sin^2 \theta}}{\sqrt{n_i^2 - \sin^2 \theta} + \sqrt{n_{i+1}^2 - \sin^2 \theta}} \quad (2.7)$$

or

$$R_{p_{i,i+1}} = \frac{n_{i+1}^2 \sqrt{n_i^2 - \sin^2 \theta} - n_i^2 \sqrt{n_{i+1}^2 - \sin^2 \theta}}{n_{i+1}^2 \sqrt{n_i^2 - \sin^2 \theta} + n_i^2 \sqrt{n_{i+1}^2 - \sin^2 \theta}} \quad (2.8)$$

where  $R_{S_{i,i+1}}$  and  $R_{p_{i,i+1}}$  are the Fresnel reflection coefficients for the interface between the  $i^{th}$  and the  $i^{th} + 1$  dielectric medium when the electric field is perpendicular or parallel to the medium.

Table 2.5 Transmission coefficients of inner building wall partitions and movable partitions at 57.5 GHz [19].

<b>Material Type</b>	<b>Polarization</b>	<b>Transmission Coefficients (dB)</b>
Interior building wall	Vertical	-5.4 to -8.1
Interior building wall	Horizontal	-5.1 to -7.8
Movable partition with plywood and glass wool	Vertical	-9.2 to -10.1
Movable partition with plywood and glass wool	Horizontal	-7.9 to -8.3
Low partition made of cloth-covered plywood surface	Vertical	-3.9 to -8.7
Low partition made of cloth-covered plywood surface	Horizontal	-3.4 to -8.4

For the penetration measurements of different wall types, the researchers measured the same wall *A* using circular polarization and compared it with the received amplitude measured for perpendicular and parallel polarization configurations [19]. The results showed that the reflection coefficients for circular polarization were much lower than under linear polarization scenarios when the incident angles were relatively small. The results indicated that circular polarization could greatly reduce the reflection in multilayered structures.

The interior wall *B* was also measured but different reflection characteristics were obtained as compared to wall *A*. The difference was caused by the different measurement positions and the inner structure of the test material for wall *B*. The transmission coefficients computed for wall *B* showed that plasterboard had a transmission loss of a few decibels for both vertical and horizontal polarization scenarios. Table 2.5 displays the transmission coefficients determined from the measurements in [19].

Office partitions are another type of structure that contribute to shadowing and that influence the indoor propagation channel [20]. The configuration of partition measurements is shown in Fig. 2.1. The transmitter and receiver were separated by 3 meters with the tested partition placed

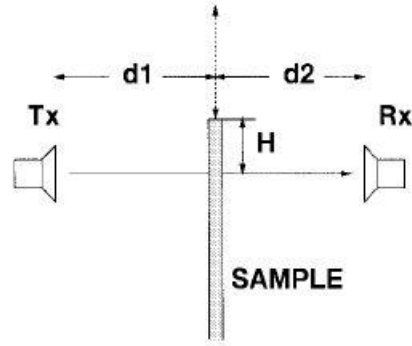


Fig. 2.1 The configuration of partition loss measurements.  $d_1$  and  $d_2$  are separation distances from the tested material to the transmitter and receiver, respectively.  $H$  is the distance from the direct propagation line to the edge of the tested partition [20].

between the two. The two antennas were pointing towards each other on boresight and perpendicular to the surface of the tested material. The two distances  $d_1$  and  $d_2$  are the separation distances from the tested material to the transmitter and receiver, respectively.  $H$  is the distance from the direct propagation line to the edge of the tested partition. The parameter  $\nu$  defined below is the clearance of the LOS path:

$$\nu = H \sqrt{\frac{2(d_1+d_2)}{\lambda d_1 d_2}} \quad (2.9)$$

where a positive value of  $\nu$  indicates LOS propagation between the TX and RX, and a negative value refers to the partition creating a non-line-of-sight (NLOS) environment between the TX and RX. The measured results were consistent for both perpendicular and parallel polarization scenarios, indicating that polarization will not have a major influence on shadowing. As the shadowing region became deeper ( $\nu$  increased) for metallic objects, the received power decreased monotonically. For wooden partitions there was a local minimum in the shadowed region ( $\nu < 0$ ), where the shadowing became deeper as the received power increased. The received power levels were lower than predicted in the knife-edge diffraction regions because the

edges of the tested partitions were not ideal knife-edges. Table 2.6 summarizes the complex refractive indices determined in [20].

Researchers at the University of Manitoba have conducted measurements to study the reflection coefficients for common floor materials in the 57-64 GHz frequency band [25]. Three common floor materials were considered for these measurements and study: hardwood, vinyl, and carpet, along with the influence of supporting materials (e.g. plywood and underpad). An unclipped continuous wave was generated by a signal generator as the transmitted signal with a power of 10 dBm, and a spectrum analyzer was used to measure power at the receiver. Pyramidal V-band horn antennas with 23.5 dBi of gain at 60 GHz and 11.3°-11.8° half-power beamwidths were used at the transmitter and receiver. The reflection coefficients for incident angles from 10° to 65° as well as transmission loss for face-to-face antenna directions were measured. The measurements were conducted with perpendicularly polarized antennas, that is, the electric field

Table 2.6 Complex refractive indices of various test materials in office buildings at 57.5 GHz, 78.5 GHz, and 95.9 GHz [20].

Tested Material	Frequency (GHz)		
	57.5	78.5	95.9
Concrete	2.55-j0.084	N/A	2.49-j0.068
Floor board	1.98-j0.083	1.91-j0.096	1.78-j0.11
Plasterboard A	1.76-j0.016 1.58-j0.010	N/A	N/A
Plasterboard B	1.77-j0.054 1.54-j0.039	N/A	N/A
Plasterboard C	1.74-j0.023 1.50-j0.010	1.73-j0.028 1.54-j0.033	1.65-j0.023 1.50-j0.020
Ceiling board with rock wool	1.26-j0.005	1.25-j0.009	1.25-j0.016

was perpendicular to the plane of incidence. The test material sizes were chosen based on the antenna specifications (i.e. antenna aperture, half-power beamwidth).

The reflection coefficient measurements were based on the specular reflection scenario. Therefore, the reflection coefficient for a single layer sample can be expressed as:

$$\Gamma = \frac{1 - e^{-j2\delta}}{1 - \Gamma_i'^2 e^{-j2\delta}} \Gamma_i' \quad \text{for } i \in \{\perp, \parallel\} \quad (2.10)$$

where  $\delta = \frac{2\pi d}{\lambda} \sqrt{\epsilon_r - \sin^2 \theta}$ ,  $\lambda$  is the wavelength in free space,  $d$  is the thickness of the tested material,  $\epsilon_r$  is the relative permittivity of the tested material, and  $\theta$  is the angle of incidence.  $\Gamma_{\perp}'$  and  $\Gamma_{\parallel}'$  represent the Fresnel reflection coefficients when the electric field is perpendicular and parallel to the plane of incidence, respectively. The coefficients are further given in [18] as:

$$\Gamma_{\perp}' = \frac{\cos \theta - \sqrt{\epsilon_r - \sin^2 \theta}}{\cos \theta + \sqrt{\epsilon_r - \sin^2 \theta}} \quad (2.11)$$

and

$$\Gamma_{\parallel}' = \frac{\epsilon_r \cos \theta - \sqrt{\epsilon_r - \sin^2 \theta}}{\epsilon_r \cos \theta + \sqrt{\epsilon_r - \sin^2 \theta}} \quad (2.12)$$

The absolute value of the reflection coefficient was calculated by computing the ratio of the received power reflected from the same plate to the reflected power from an aluminum plate, whose reflection coefficient is assumed to be -1. The measured results showed that cut-pile type carpets are poor reflectors due to their high transmission loss. However, favorable reflection became noticeable when the carpet was supported by a plywood layer.

The transmission loss was measured by comparing the received power with and without the test material. The researchers used electromagnetic absorbers to suppress the undesired diffracted and reflected wave components from the material surface. The measured results showed that the transmission loss increased as the thickness of the material increased. The carpet material

showed the lowest transmission loss and the hardwood had the largest loss regardless of the thickness.

## 2.6 Antenna Pattern Diversity Studies

Researchers in the Netherlands performed measurements to investigate the impact of antenna patterns and the reflective properties of the indoor channel environment in both LOS and NLOS scenarios at 60 GHz [26]. Fig. 2.2 shows the floor layout of the measurement scenarios. The channel sounding system used for measurements employed a vector network analyzer with the  $S_{21}$  transmission parameter in the frequency range from 57 GHz to 59 GHz. Complex channel impulse responses were obtained by taking the inverse Fourier transform of the  $S_{21}$  parameter after applying a Kaiser window, with a side lobe level of -44 dB. The channel impulse response resolution was 1 ns. Vertically polarized biconical antennas with 9 dBi of directivity were used at both the transmitter and receiver. These antennas were omnidirectional in the azimuth plane and the half-power beamwidth in the elevation plane was  $9^\circ$ . The TX antenna was fixed at a position in the test room with three adjustable heights of 1.4, 1.9, and 2.4 meters, whereas the RX antenna was at a height of 1.4 meters above ground and could be moved to different receiver locations around the indoor environment.

The researchers defined normalized received power (NRP) as the received power divided by the transmit power within the considered bandwidth between 57-59 GHz. In decibel scale, NRP is the inverse of the path loss. NRP can be expressed as:

$$NRP_d(dB) = NRP_{d_0} - 10n \log_{10} \left( \frac{d}{d_0} \right) + X_\sigma(dB) \quad (2.13)$$

where  $NRP_{d_0}$  is the NRP at the reference distance  $d_0 = 1$  m,  $n$  is the path loss exponent, and  $X_\sigma$  is a zero-mean lognormal random variable with standard deviation  $\sigma$ .

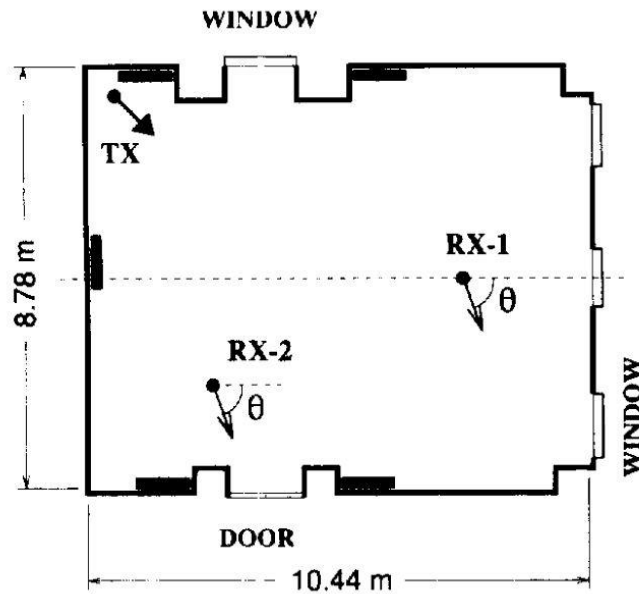


Fig. 2.2 Floor layout of polarization dependent measurements at 60 GHz [26].

In 1994 researchers in Japan studied the polarization dependence of indoor channel propagation at 60 GHz [21]. They conducted measurements in an empty modern office environment using a vector network analyzer, with a transmitter and receiver centered at 60 GHz. They measured the complex frequency transfer functions and computed the impulse response by applying the inverse Fourier transform. The transmitter antenna was a wide-beam scalar horn antenna with a  $60^\circ$  half-power beamwidth, and the receiver antenna was a narrow-beam scalar lens-horn antenna with a  $4.6^\circ$  half-power beamwidth. The polarizations of both the transmitter and receiver antenna were switchable among vertical, horizontal, and right-handed circular polarization, by linear-circular switchable polarizers. The cross-polarization discrimination (XPD) was larger than 17 dB at both transmitter and receiver antennas.

The researchers measured the impulse responses of the channel by changing the azimuth angle of the receiver antenna. The measurement results showed that using circularly polarized antennas could effectively reduce the multipath delay spread. The researchers also reported a

comparison of RMS delay spread measured with circular and linear polarizations. It was found that the RMS delay spread measured with circularly polarized antennas was only about half of that found when using linearly polarized antennas. Similar results were also found by Rappaport *et al.* as presented in [27].

Researchers also created a computer-based simulation on indoor BPSK modulation channel performance by analyzing bit error rate (BER) using different antenna polarizations. The simulation results showed that the BER improved significantly when circular polarization was employed [21]. Table 2.7 shows common antennas and their corresponding antenna gain, half-power beamwidth, and effective aperture area calculations.

Table 2.7 Common antenna comparisons [28].

Antenna Type	Antenna Gain	Beamwidth	Effective Aperture
Half wave dipole	2.15 dBi, where: $G_{\frac{\lambda}{2}} = \frac{60^2}{30R_{\frac{\lambda}{2}}} = \frac{4}{\text{Cin}(2\pi)}$	78° Formula not applicable	$e = 0.1305\lambda^2$
Microstrip patch antenna (2 × 2)	9.5 dBi $g(\theta, \phi) = (\cos^2\theta \sin^2\phi + \cos^2\phi) F(\theta, \phi) ^2$	65° Formula not applicable	Formula not applicable
Horn antenna	24.5 dBi $G = \frac{4\pi A}{\lambda^2} e_A$	$\theta_{3dB} = 70^\circ \frac{\lambda}{D}$ D is the dimension	0.49 $e_A(\sigma_a, \sigma_b) = \frac{1}{8}  F_1(0, \sigma_a) F_0(0, \sigma_b) ^2$
Parabolic antenna	$G = \frac{\pi^2 d^2}{\lambda^2} e_A$	$\theta_{3dB} = k\lambda/d$	0.55 ~ 0.65 $e_A = 40 \cot^2(\psi_0/2) [\sin^4(\psi_0/2) + \ln(\cos(\psi_0/2))]^2$ $\psi_0 = 53.31^\circ$

## 2.7 Indoor Channel Models and E-band Regulations

### 2.7.1 ITU Recommendation ITU-R P.1238-7

The ITU Recommendation ITU-R P.1238-7 provides information on seven aspects over the frequency range from 900 MHz to 100 GHz for the consideration of potential applications in a short-range indoor environment [23]. The local area radio network should be compatible with current wireless and wired networks, and should also provide low power consumption for personal and mobile environments. The seven aspects of design guidance are as follows: path loss models, delay spread models, antenna polarization and radiation patterns, effects of transmitter and receiver location, effects of various building materials, effects of moving objects, and a static usage model.

The path loss models are classified as site-general models and site-specific models in this recommendation. Site-general models represent models that do not require much knowledge of the path of a propagating wave or site-specific information. The model in this section accounts for the path loss through multiple floors, for the consideration of frequency reuse in multi-floor scenarios. The basic model has the following form:

$$PL_{total} = 20 \log_{10} f + N \log_{10} d + L_f(n) - 28 \quad (2.14)$$

where  $N$  is the distance power loss coefficient,  $f$  is the frequency in MHz,  $d$  is the T-R separation distance in meters (usually greater than 1 m).  $L_f$  is the floor penetration loss factor in dB, and  $n$  is the number of floors between the transmitter and the receiver, and is greater than or equal to 1. According to the table in ITU Recommendation ITU-R P.1238-7, at 60 and 70 GHz due to higher atmospheric attenuation, the power loss coefficient  $N$  is 22 in office buildings, and is much smaller than those reported at lower frequencies [23].

Table 2.8 FCC E-band regulations [30].

<b>Bandwidth</b>	5 GHz
<b>Maximum Allowable EIRP</b>	+85 dBm (Fixed) +85 dBm (Mobile)
<b>Minimum Antenna Gain</b>	+43 dBi
<b>Maximum Beamwidth</b>	1.2°

The floor penetration loss factor  $L_f$  does not have statistics for the 60 and 70 GHz bands; however, the value of this factor increases as the frequency increases so it is predictable that at 60 and 70 GHz, the floor penetration loss factor would be much larger than 22 dB as noticed at 5.8 GHz for penetration through one floor and 28 dB through two floors. Different floor construction materials also cause additional penetration loss, and is added to the general floor penetration loss factor  $L_f$ , creating a site-specific model.

## 2.7.2 E-Band Regulations in the United States and Europe

### 2.7.2.1 FCC Regulation

The Federal Communications Commission (FCC) established service rules in Code of Federal Regulations, Title 47, Part 15 (47 CFR 15) and Part 101 (47 CFR 101) to regulate the use of E-band spectra in fixed wireless communications [3] [29]. For the frequency range spanning 71-76 GHz and 81-86 GHz, the bandwidth is 5 GHz, and in these bandwidths, the maximum effective isotropic radiated power (EIRP) for both fixed and mobile systems is +85 dBm. Additionally, the maximum transmit power is +35 dBm, the maximum HPBW is 1.2°, and the minimum antenna gain is 43 dBi [30]. Transmitter locations are not specified in the regulation for the 72-76 GHz bands. Table 2.8 displays the general conclusion of regulations provided by the FCC.

- a) Emission limitations

Emission limitations exist for frequencies above 15 GHz, where the attenuation must follow the following equation [30]:

$$A = 11 + 0.4(P - 50) + 10 \log_{10} B \quad (2.15)$$

where  $A$  is the attenuation below the mean output power level such that greater than 56 dB is not required.  $G$  is the percent of bandwidth removed from the carrier frequency, and  $B$  is the authorized bandwidth in megahertz [30].

The emission mask for the 71-76 GHz, 81-86 GHz, 92-94 GHz, and 94.1-95 GHz bands used in (2.15) applies only to the edge of each channel, but not to sub-channels established by licensees. The value of  $P$  in the equation is for the percentage removed from the carrier frequency and assumes that the carrier frequency was the center of the actual bandwidth used. The value of  $B$  will always be 500 MHz. In the case where a narrower sub-channel is used within the assigned bandwidth, the sub-carrier will be located sufficiently far from the channel edges to satisfy the emission levels of the mask. The mean output power used in the calculation is the sum of the output power of a fully populated channel [30].

#### b) Antenna polarization

Table 2.9 provides detailed specifications for antenna beamwidth and gain. In subpart 101.117, the regulation states, “Stations operating in the radio services included in this part are not limited as to the type of polarization of the radiated signal that may be employed. However, in the event that interference in excess of permissible levels is caused by the operation of other stations as a result of employing other than linear polarization, the Commission may order a licensee to change its system polarization to mitigate the interference. No change in polarization may be made without prior authorization from the Commission. Unless otherwise allowed, only linear polarization (horizontal and vertical) shall be used. For LMDS systems,

Table 2.9 Antenna standards [29].

Freq. (GHz)	Maximum beamwidth to 3 dB points (degrees)	Minimum antenna gain (dBi)	Minimum radiation suppression to angle in degrees from centerline of main beam in decibels						
			5° ~10°	10° ~15°	15° ~20°	20° ~30°	30° ~ 100°	100° ~140°	140° ~180°
71-76 (co-polar)	1.2	43	35	40	45	50	50	55	55
71-76 (cross-polar)	1.2	43	45	50	50	55	55	55	55

unless otherwise authorized, system operators are permitted to use any polarization within its service area, but only vertical and/or horizontal polarization for antennas located within 20 kilometers of the outermost edge of their service area” [29].

Note: Antenna gains less than 50 dBi (but greater than or equal to 43 dBi) are permitted only with a proportional reduction in maximum authorized EIRP in a ratio of 2 dB of power per 1 dB of gain, so that the maximum allowable EIRP (in dBW) for antennas of less than 50 dBi gain becomes  $+55-2(50-G)$ , where G is the antenna gain in dBi [29]. In addition, antennas in these bands must meet two additional standards for minimum radiation suppression: At angles between 1.2 and 5° from the centerline of the main beam, co-polar discrimination must be  $G-28$ , where G is the antenna gain in dBi; and at angles of less than 5° from the centerline of the main beam, the cross-polar discrimination must be at least 25 dB.

c) Frequency assignments

The frequency bands at 71-76 GHz and 81-86 GHz are shared with stations in the fixed-satellite service and Government fixed stations in the Private Operational Fixed Point-to-Point Microwave Service.

Table 2.10 The ETSI EN 302 217-3 EIPR limit and minimum antenna gain [31].

<b>EIRP limit (dBm)</b>	$\leq +85$ (Radio Regulation Art 21)	for $G_{\text{ant}} \geq +55$ dBi
	$\leq +85 - (55 - G_{\text{ant}})$	for $+55 \text{ dBi} > G_{\text{ant}} \geq +45$ dBi
	$\leq +75 - 2 \times (45 - G_{\text{ant}})$	for $+45 \text{ dBi} > G_{\text{ant}} \geq +38$ dBi
<b>Minimum <math>G_{\text{ant}}</math> (dBi)</b>	$\geq +38$	
	$\geq P_{\text{out}} \text{ (dBm)} + 15$ or $+38$ dBi (whichever is the greater) $\leq +85 - P_{\text{out}} \text{ (dBm)}$	

### 2.7.2.2 European ETSI Regulation

The Electronic Communication Committee (ECC) Recommendation 05 (07) contains channel arrangements for a fixed service system operating at 71-76 GHz in Europe. The ECC/REC/(05)07 is based on a LOS scenario with point-to-point transmission. The European Telecommunications Standards Institute (ETSI) EN 302 217-3 describes the characteristics and requirements for point-to-point equipment and antennas. The maximum EIRP for antennas with a gain higher than +55 dBi is +85 dBm, the same as the FCC standard. The minimum antenna gain is +38 dBi [31] [32].

According to ETSI EN 302 217-3, for frequency bands ranging from 71-76 GHz and 81-86 GHz, emissions of equipment in the scope of the document are limited as follows: For equipment offering external antenna connectors, the limitation should be translated in terms of range of antenna gain that the manufacturer shall state for the use with the equipment for not exceeding the EIRP limitations in Table 2.10. In Table 2.10  $P_{\text{out}}$  is the maximum possible power, including tolerances, delivered to the antenna connector.

As additional provisions, equipment implementing ATPC as a permanent feature, linearly activated only by the drop of RSL in the corresponding far end receiver, while complying with the requirements 1a and 2a (or 1b and 2b as appropriate) when operating in nominal unfaded

conditions, are permitted to raise their emission, during rain induced fading periods, up to a level of:

1) Equipment with integral antennas:

$$\begin{aligned} \text{EIRP (dBm)} &\leq +35 + G_{\text{ant}} \text{ (dBi) or} \\ &\leq +85 \text{ dBm (whichever is the lower)} \end{aligned}$$

2) Equipment offering external antenna connectors:

$$P_{\text{out}} \text{ (dBm)} \leq +35$$

## 2.8 Foliage Studies

The influence of foliage and vegetation is a very important factor to consider when designing wireless systems because of the attenuation that propagating waves experience. Different types of vegetation affect propagation in various ways, and the season and state of the vegetation have different influences as well. Studies done in [33] showed that the Hata model could be used for path loss estimation in forested terrain, although at 1800 MHz, damp forests incurred an additional attenuation of about 5 dB [34]. Other researchers considered forest and foliage environments to be modelled by a dielectric layer such that the two layers are air and ground [35].

Table 2.11 Antenna regulations provided by the FCC, ETSI, and those used by NYU WIRELESS in the E-band [5] [29] [30] [31].

	<b>FCC (United States)</b>	<b>ETSI (Europe)</b>	<b>NYU WIRELESS</b>
<b>Maximum EIRP</b>	+85 dBm	+85 dBm	+42 dBm
<b>Transmit Power</b>	+35 dBm	Not Applicable	+14.6 dBm
<b>Minimum Antenna Gain</b>	+43 dBi	+38 dBi	+27 dBi and +20 dBi
<b>Maximum Beamwidth</b>	1.2°	Not applicable	7° and 15°

Wang and Sarabandi estimated attenuation through dense foliage with multiple scatterers at 35 GHz based on the analysis of electromagnetic radiation theory [36]. The model treats a forest canopy as a random medium that consists of many dielectric objects (e.g. branches, twigs, and leaves, etc.). The foliage causes attenuation and scattering on incident electromagnetic waves and the attenuation varies with the size of leaves, foliage density, and polarization of the radiated electromagnetic wave. One of the widely used methods for estimating attenuation rate in foliage is Foldy's approximation because of its simplicity [37]. However, as the frequency bands increase to millimeter-waves, the single scattering theory is no longer sufficiently accurate in predicting the scattering effect from induced from foliage. Thus, more real-world propagation measurements must be done in order to model mmWave foliage effects.

## **2.9 Ray-tracing and Modeling for Wireless Channels**

Ray-tracing and modeling is an important component of predicting and simulating wireless communication channels. Ray-tracing tools and software are generally built based on real-world measurements conducted both indoors and outdoors. Modeling indoor environments with ray-tracing is usually simpler than outdoor scenarios because the environment is more controlled. Many propagation studies have been performed at lower UHF band frequencies to understand indoor wireless channels and to create ray-tracing software and simulations to model such environments.

Many different ray-tracing models have been studied in the past. One such model based on geometric optics was used for propagation prediction in buildings for PCS network design [38] [39]. The simulator modeled each source ray as in ideal wavefront and included both transmitted, reflected, and scattered rays in the indoor environment. The model helped to determine quantitative differences between observed and predicted PDPs, but also provided accurate

predictions of impulse responses, path loss, and delay spread when using site-specific knowledge [39].

Another indoor wireless prediction model was developed using an image-based ray tracing method / algorithm. The algorithm uses a blueprint plan of the indoor environment to determine reflected and transmitted multipath components that are separated into parallel and perpendicular polarizations during processing [40]. The model also incorporates the dielectric constants of in-building obstructions for scattering and transmission effects. The image-based ray-tracing method had reasonable results with predicted PDPs to those actually recorded, but not enough statistics were presented in [40] for an overall assessment of the model.

Ray-tracing computer simulations generally use empirical measurement results and various parameters determined from real-world data in order to create prediction models. The effects of different antenna patterns and polarization settings are usually programmable options and inputs to the simulators. Ho and Rappaport measured the effects of antenna polarization and beam patterns on delay spread and path loss of an obstructed indoor channel to show the prominence of vertical polarization in regards to strong received power and low delay spreads [41]. The results of this had the potential to help develop wireless systems in the early 1990's, and could also be used in robust ray-tracing simulations. Similar works showed that use of linearly polarized antennas helped to mitigate multipath components; however, multipath in future systems will be an advantage rather than a disadvantage [42]. Using image theory and the geometry of indoor building construction, a propagation prediction model was created by Ho *et al.* that took into account the effects of antenna polarization, antenna patterns, and other building properties [42]. Prediction results were reasonable when compared to true observed measurements and results. A previous measurement campaign at 60 GHz, much higher in frequency than the UHF/Microwave

bands was conducted by Xu *et al.* in order to analyze PDPs and their spatial/temporal properties for the indoor environment as well [43]. The extensive measurement campaign was able to produce results that showed a strong relationship between multipath and the different indoor environments tested. Some of the spatial and temporal statistics computed could be used as a basis for a 60 GHz ray-tracing computer simulator for indoor coverage prediction.

A similar model to [39] used modified geometrical optics to predict path loss and delay spread by using building information including location, height, and electrical properties for accurate predictions, but for an outdoor microcellular environment [43]. The results from this work were used in the development of a commercial style ray-tracing and propagation prediction tool, with accurate results. Durgin *et al.* also created a ray-tracing method and simulation for the outdoor wireless channel [45] [46]. Their method presented a new 3D ray tracing launching technique that had speed and accuracy unlike any other at the time. Instead of a planar wavefront and image-based theory, they used a geodesic ray launching method, and also improved ray-reception using a weighting function. In addition, the improved 3D ray launching method had the ability to model phasor-summed fields and could produce accurate fading profiles, unlike the reception sphere model [46]. While these models and simulators have been created for UHF/Microwave bands, the measurements in this report and others by the NYU WIRELESS team can be used to create models and ray-tracing simulators for future mmWave propagation and wireless networks.

## Chapter 3 Indoor and Outdoor Measurement Campaign Overview

### 3.1 Channel Sounder System and Hardware

In this chapter, the sliding correlator channel sounder system used for the 73 GHz indoor and outdoor measurements is described in detail. The theory of sliding correlation was originally introduced by Donald Cox in 1972 [47]. The basic principle of sliding correlation is to cross-correlate a known transmitted sequence (that experiences power attenuation through the wireless channel) that is detected at a receiver, with an identical reference sequence clocked at a slightly lower rate at the receiver, yielding a sharp impulse or spike that is recorded, every time the identical sequences align with one another. The capture of this cross-correlation is otherwise known as a PDP, and contains many sharp peaks (over the duration of one sequence frame) due to copies and reflections that the transmitted signal encountered in the channel before reaching the receiver. These extra copies observed are known as multipath. PN sequences are typically used for cross-correlation in channel sounding systems due to the large peak observed during maximal alignment, and a weak, noisy-like signal observed when the sequences are out of phase. The cross-correlation output recorded during measurements is “time-dilated” due to the offset in clock rates, but is easily rescaled to produce a true un-dilated PDP using the slide factor as presented and explained in [24]. The time dilation eases the hardware requirement of the digitizer in that the frequency content is collapsed to a narrow bandwidth, and therefore a sampling rate much lower than the transmitted clock rate can be used to acquire channel impulse responses (PDPs).

As discussed in Chapter Two, previous researchers used vector network analyzers (VNA) at the receiver to measure received power levels at various frequencies. The disadvantages of using a VNA are as follows: 1) the equipment is bulky and heavy, making it difficult to move around

to multiple receiver locations, 2) the VNA and other impulse-based channel sounders are sensitive to interference; and 3) the available bandwidth provided by a VNA is often much smaller than the desired wide bandwidths to be studied at mmWave. In contrast, our channel sounding system offers a direct spread spectrum sliding correlator method, with a system bandwidth specified by the PN sequence clock rate. For the 73 GHz indoors and outdoors measurements, a 400 mega-chip-per-second (Mcps) PN sequence was transmitted, resulting in an 800 MHz null-to-null RF bandwidth spread spectrum signal centered around the 73.5 GHz center frequency. The following sections describe the transmitter and receiver, as well as major components used in the channel sounding system.

### 3.1.1 Transmitter Hardware Descriptions

Fig. 3.1 shows the block diagram of the transmitter of the 73 GHz channel sounder system. The baseband signal is generated from a digital logic board to generate a length 2047 PN sequence that is clocked at 400 MHz, producing a 400 Mcps PN sequence. The baseband signal is mixed with an intermediate frequency (IF) at 5.625 GHz. The spread spectrum IF signal at  $5.625 \text{ GHz} \pm 0.4 \text{ GHz}$  is the IF input to the up-converter. A local oscillator (LO) signal, generated at 22.625 GHz is tripled in the up-converter and then mixed with the  $5.625 \text{ GHz} \pm 0.4$

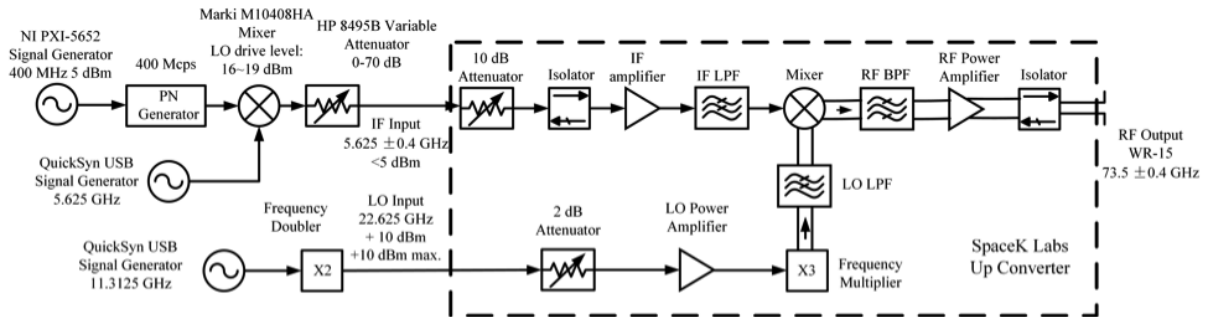


Fig. 3.1 Block diagram of the transmitter for the 73 GHz channel sounder. The transmitter consists of the following critical components: a pseudorandom noise sequence generating PCB board; an intermediate frequency synthesizer; a local oscillator frequency synthesizer; an up-converter RF front end box; and a narrowbeam directional horn antenna.

GHz signal to generate the  $73.5 \text{ GHz} \pm 0.4 \text{ GHz}$  spread spectrum RF signal that has a null-to-null bandwidth of 800 MHz. A pair of vertically polarized antennas with 20 dBi of gain and  $15^\circ$  HPBW was used at both the transmitter and receiver for indoor measurements. For outdoors free space, foliage, and ground bounce measurements, a pair of 27 dBi gain horn antennas ( $7^\circ$  HPBW) was used.

### 3.1.1.1 Pseudorandom Noise Sequence Generating PCB Board

The PCB board shown in Fig. 3.2 generates the pseudorandom noise (PN) sequence using two-cascaded 8-bit shift registers produced by ON Semiconductor to realize the function of an 11-bit shift register. The total length of the PN sequence is 2047 ( $2^{11}-1 = 2047$ ). The 9<sup>th</sup> and 11<sup>th</sup> shift registers are fed back to create the maximal-length sequence.

### 3.1.1.2 Intermediate Frequency Synthesizer

The intermediate frequency (IF) synthesizer is provided by National Instruments. Fig. 3.3 is the front view of the frequency synthesizer (Model No. FSW-0010). The left most port of the

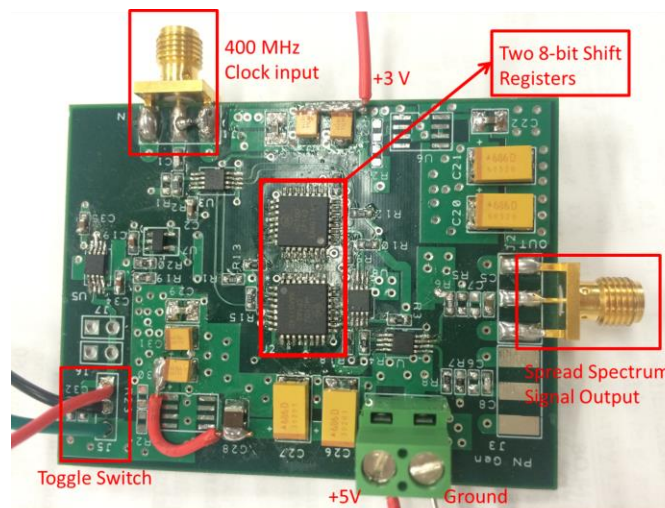


Fig. 3.2 The layout of the PN sequence generating board.



Fig. 3.3 Phase Matrix QuickSyn frequency synthesizer for the IF.

device is the CW signal output at 5.625 GHz. The white connector supplies power and the blue cable is the USB connector used for controlling the frequency synthesizer via a laptop. The frequency synthesizer covers a wide range of frequency bands (0.1~10 GHz) with high frequency resolution (0.001 Hz). Table 3.1 lists the specifications of the intermediate frequency synthesizer.

The baseband PN sequence signal is mixed with the IF signal using a mixer (Marki M10408HA). Table 3.2 lists the specifications of the mixer. The LO input of the mixer is the IF

Table 3.1 Specifications of the Phase Matrix QuickSyn frequency synthesizer for the IF.

<b>Name</b>	QuickSyn Microwave Frequency Synthesizer
<b>Model No.</b>	FSW-0010
<b>Frequency Range</b>	0.1 to 10 GHz
<b>Frequency Resolution</b>	0.001 Hz
<b>Maximum Output Power</b>	+15 dBm
<b>Supply Voltage</b>	+12.0 to +12.6 V DC
<b>Power Consumption</b>	20 W nominal
<b>Size</b>	12.7×17.78×2.54 cm
<b>Weight</b>	1.13 kg

Table 3.2 Marki mixer (M10408HA) operating specifications and requirements.

<b>Name</b>	Marki Mixer
<b>Model No.</b>	M1-0408
<b>LO Range</b>	4 to 8 GHz
<b>RF Range</b>	4 to 8 GHz
<b>IF Range</b>	DC to 4 GHz
<b>Conversion Loss</b>	5.5 dB
<b>LO to RF Isolation</b>	35 dB

CW signal at 5.625 GHz generated by the IF frequency synthesizer QuickSyn, and the IF input of the mixer is the baseband PN signal. The output signal of the mixer is a spread spectrum modulated signal at  $5.625 \text{ GHz} \pm 0.4 \text{ GHz}$ . The most important characteristic of a mixer is the conversion loss. Conversion loss is defined as the ratio of the output frequency power to the input frequency power for a given LO (local oscillator) power level. The mixer used in this system has a conversion loss of 5.5 dB. Another important parameter is isolation which is defined as the amount of power that leaks from one mixer port to another. The higher the value is, the less the RF output will be affected by the LO power. The Marki mixer provides a 35 dB LO to RF isolation, which is sufficiently high to guarantee high performance of the RF output.



Fig. 3.4 Phase Matrix QuickSyn frequency synthesizer for the LO signal. The top box is a model FSW-0020 digital frequency synthesizer and the bottom box contains a frequency doubler and amplifier.

### 3.1.1.3 Local Oscillator Frequency Synthesizer

The local oscillator (LO) input to the up-converter is obtained from a frequency doubler and amplifier mounted on a heat sink, below a QuickSyn digital frequency synthesizer operating at 11.3125 GHz, resulting in a CW signal at 22.625 GHz. Fig. 3.4 shows the combination of the synthesizer and the frequency doubler. The frequency doubler allows us to reach the 22.625 GHz LO frequency requirement and the internal amplifier allows for a constant 10 dBm of LO drive power for the up-converter to make up for cable loss incurred in the long cable required to reach the TX height of 2.5 meters. The specifications for the LO synthesizer are similar to the IF frequency synthesizer and are shown in Table 3.3.

### 3.1.1.4 Up-Converter Box

The up-converter is produced by Spacek Labs in Santa Barbara, California. It consists of three input ports: the power supply input, the IF input, and the LO input. The IF and LO input power levels of the up-converter should not exceed 5 dBm and 10 dBm, respectively. The LO

Table 3.3 Specifications of the Phase Matrix QuickSyn frequency synthesizer for the LO.

<b>Name</b>	QuickSyn Microwave Frequency Synthesizer
<b>Model No.</b>	FSW-0020
<b>Frequency Range</b>	0.2 to 20 GHz
<b>Frequency Resolution</b>	0.001 Hz
<b>Maximum Output Power</b>	+13 dBm
<b>Supply Voltage</b>	+12.0 to +12.6 V DC
<b>Power Consumption</b>	20 W nominal
<b>Size</b>	12.7×17.78×2.54 cm
<b>Weight</b>	1.13 kg

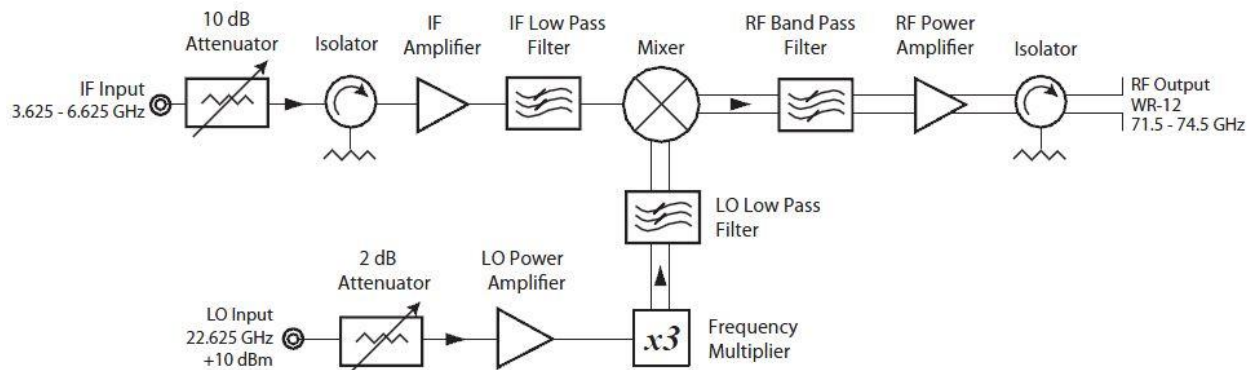


Fig. 3.5 Block diagram of the 73 GHz channel sounder up-converter.

input frequency of 22.625 GHz is tripled inside the up-converter to obtain a 67.875 GHz center frequency which is mixed with the wideband IF frequency of 5.625 GHz  $\pm$  0.4 GHz to obtain the RF transmitted spread spectrum signal of 73.5 GHz  $\pm$  0.4 GHz. With a LO input power of 10 dBm and an IF input power of -40 to -20 dBm, the up-converter has an overall frequency flat gain of 32.3 dB at 73.5 GHz. Fig. 3.5 shows the block diagram of the transmitter RF front-end up-converter and Table 3.4 describes the up-converter specifications and requirements.

### 3.1.1.5 Transmitter Antennas

The transmit antennas were produced by MI-WAVE. For indoor measurements the transmit antenna had a gain of 20 dBi with a HPBW of 15°, and the model number is 261V-20/385. For the outdoor measurements the transmit antenna had a gain of 27 dBi with a HPBW of 7°, and the

Table 3.4 73 GHz channel sounder up-converter specifications and requirements.

<b>Name</b>	73 GHz Transmitter
<b>Model No.</b>	T73-5B
<b>RF Output Frequency</b>	73.5 GHz $\pm$ 0.4 GHz
<b>LO Frequency (GHz)</b>	67.875
<b>IF Input Frequency</b>	5.625 GHz $\pm$ 0.4 GHz
<b>RF to IF Gain (dB)</b>	32.3 (at 73.5 GHz when LO power is 10 dBm and IF power is -40 to -20 dBm.)
<b>Maximum IF Input Power (dBm)</b>	+5
<b>Maximum LO Input Power (dBm)</b>	+10
<b>1 dB Compression (dBm)</b>	+14.4

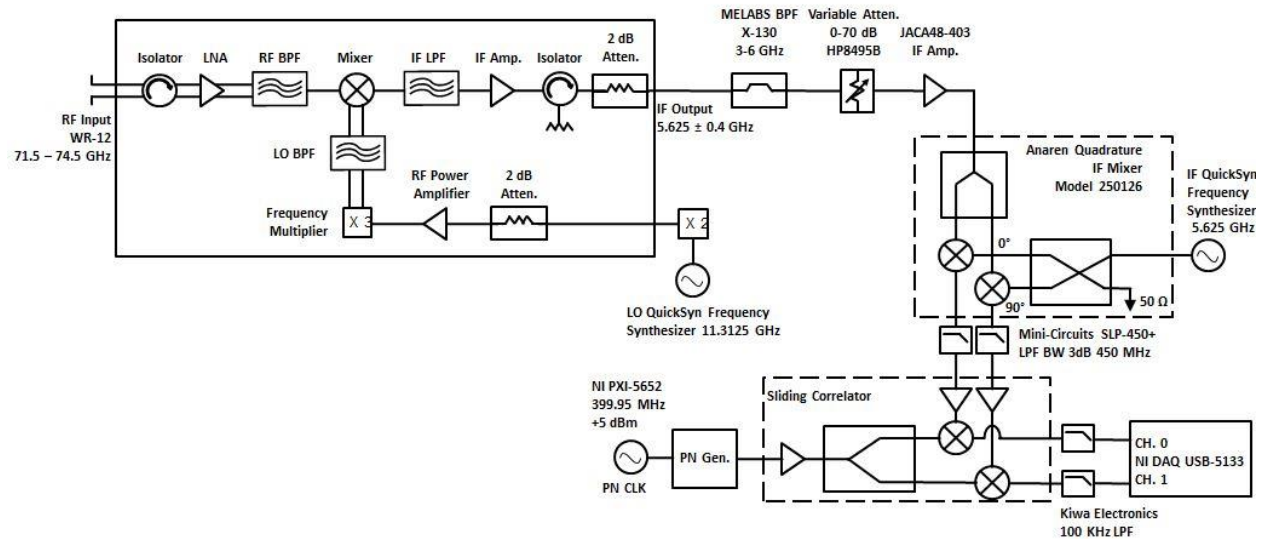


Fig. 3.6 Block diagram of the receiver for the 73 GHz channel sounder system. The receiver consists of the following critical components: a pseudorandom noise sequence generating PCB board; an intermediate frequency synthesizer; a local oscillator frequency synthesizer; a down-converter RF front end box; a narrowbeam directional antenna; a low noise amplifier (LNA); a bandpass filter; a quadrature mixer; low pass filters; sliding correlator mixers; and a 2 port digitizer.

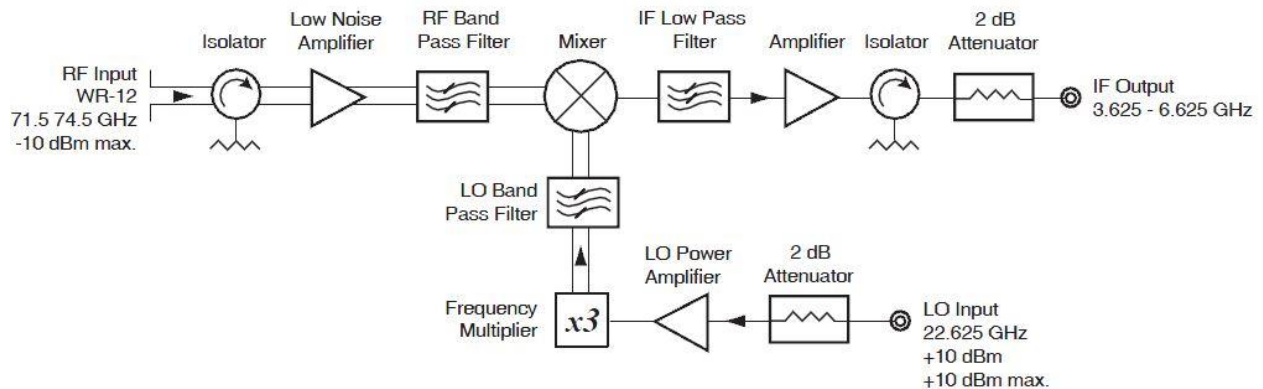


Fig. 3.7 Block diagram of the 73 GHz channel sounder down-converter.

model number is 261V-27/385.

### 3.1.2 Receiver Hardware Descriptions

This section describes the down-converter and the sliding correlator since the LO frequency synthesizer, IF frequency synthesizer, and PN sequence generating board are identical to the transmitter hardware. Fig. 3.6 and Fig. 3.7 show the block diagram of the 73 GHz channel sounder receiver and down-converter, respectively. The RF signal is captured by a narrowbeam

directional 20 dBi gain, 15° HPBW RX antenna for indoor measurements, and a narrowbeam directional 27 dBi gain, 7° HPBW RX antenna for the outdoor measurements. These antennas are identical to the transmit antennas. The captured signal is down-converted to IF via the down-converter box built by Spacek Labs. The specifications for the 73 GHz down-converter box are described in Table 3.5. The signal then goes through a bandpass filter to reduce out-of-band noise, and is subsequently amplified by a Low Noise Amplifier (LNA). The IF signal is then further down-converted into its baseband in-phase and quadrature components that are then correlated with a slightly lower clocked identical PN sequence on the receiver side in order to be digitized to create a PDP. The PN sequence at the receiver is identical to the transmitted sequence; however, it is clocked at 399.95 MHz, resulting in a time-dilated cross-correlation of the two PN sequences. The in-phase and quadrature cross-correlated outputs are then sampled via a National Instruments NI USB 5133 digitizer at a sampling rate of 2 MSamples/s.

### **3.1.1 20 dBi Antenna Pattern Characteristics**

#### ***3.1.1.1 Antenna Pattern Basics***

The antenna is a critical part of the measurement system in this project. Knowledge of the performance of the antenna is essential for understanding the channel sounder system as a whole, and also for post-processing and analysis of the data collected, as our measurements are completely related to the antennas used for measurements. Thus, it is important to characterize and know the antenna pattern, a graphical representation of the radiation characteristics of the antenna in space. Several important antenna parameters can be drawn from the antenna pattern, such as lobes, gain, half-power beamwidth, front-to-back ratio, and polarization, etc. The following subsections describe the key parameters of antenna characteristics [28].

##### **a. Lobes**

Table 3.5 73 GHz channel sounder down-converter specifications and requirements.

<b>Name</b>	73 GHz Receiver
<b>Model No.</b>	R5-73B
<b>RF Input Frequency (GHz)</b>	73.5 GHz $\pm$ 0.4 GHz
<b>LO Frequency (GHz)</b>	67.875
<b>IF Output Frequency (GHz)</b>	5.625 GHz $\pm$ 0.4 GHz
<b>RF to IF Gain (dB)</b>	28.1 (at 73.5 GHz when LO power is 10 dBm and IF power is -40 to -20 dBm.)
<b>Noise Figure (dB)</b>	5.22
<b>Maximum RF Input Power (dBm)</b>	-10
<b>Maximum LO Input Power (dBm)</b>	+10

An antenna pattern usually consists of directional lobes at different angles, displaying the directional distribution of the radiated and received signal by the antenna. In general, a lobe is defined as “a portion of the radiation pattern bounded by regions of relatively weak radiation intensity” [28]. For a directional antenna, the main lobe is expected to have much higher energy radiation than side lobes. Given an antenna pattern plot of a directional antenna, one should easily identify the main lobe, which radiates the strongest energy.

b. Gain

Antenna gain is another important parameter to describe the performance of an antenna. It is defined as the ratio of intensity in a given direction to the radiation intensity accepted by a theoretical lossless isotropic antenna. In this project, we used pyramidal horn antennas with 20 dBi of gain and 27 dBi of gain for indoor measurements and outdoor measurements, respectively. The gain can be expressed using the following equation [28]:

$$Gain = 4\pi \frac{\text{radiation intensity}}{\text{total input power}} = 4\pi \frac{U(\theta, \phi)}{P_{in}} \quad (3.1)$$

where  $U(\theta, \phi)$  is the direction intensity.

c. Half-Power Beamwidth

The half-power beamwidth (HPBW) is defined as the angle between the 3 dB point below the maximum point on either side of the main lobe. The maximum point is the peak of the

effective radiated power. The antenna HPBW specifications provided by the manufacturer were  $15^\circ$  and  $7^\circ$  for the indoor and outdoor propagation measurements, respectively.

#### d. Front-to-Back Ratio

The front-to-back ratio is the ratio of power between the front lobe and the back lobe of the antenna. This is a characteristic only for directional antennas. Antennas with good performance usually have a higher front-to-back ratio. In the specification of the antennas used in the indoor measurements, the front-to-back ratio is 25 dB. The antenna radiation pattern measurements allowed us to verify the front-to-back ratio to make sure that the antennas have acceptable or predicted performance. However, it is quite difficult to measure the true front-to-back ratio using the channel sounder system. The back of the antenna is directly attached to the converter box that has a much larger dimension than the flange of the antenna itself; causing the problem that when the antenna is rotated by  $180^\circ$  to receive the signal from its back lobe, the transmitted signal will encounter the back of the down-converter box which can result in scattering and a more highly attenuated received signal for measuring the actual front-to-back ratio. The results to follow will show such observations.

#### e. Cross-Polarization Discrimination

Cross-polarization discrimination (XPD), also known as isolation, is another important factor to understand for antennas. It describes the difference in power observed between a pair of co- and cross-polarized antennas. The larger the XPD factor is (in dB), the greater isolation between antenna polarizations. The use of different antenna polarization schemes is important because propagating waves can change polarization in environments that induce multipath. In addition, frequency reuse can be employed in LOS environments while using two different polarization schemes for communications systems. XPD factors were computed from antenna measurements for the 20 dBi antennas and are presented below.

### 3.1.1.2 Antenna Measurement Procedures

In the 73 GHz indoor measurement campaign, transmit and receive pyramidal horn antennas were used with a specification of 20 dBi of gain and  $15^\circ$  HPBW provided by the manufacturer for vertical polarization. The manufacturer does not provide any antenna pattern plots, so a procedure and experiment were developed to understand the antenna radiation pattern and to help verify several parameters such as HPBW, cross-polarization discrimination (XPD), etc. For the aforementioned purposes, we performed the antenna radiation pattern measurements under four antenna polarization scenarios, namely vertical to vertical, vertical to horizontal, horizontal to horizontal, and horizontal to vertical (V-V, V-H, H-H, H-V).

The antenna radiation pattern measurements were conducted in an indoor environment in a relatively large open space among medium-size cubicles. The height of the cubicle panels is



Fig. 3.8 Transmitter setup for the antenna pattern measurements. The height of the transmit antenna is 2 meters relative to ground.

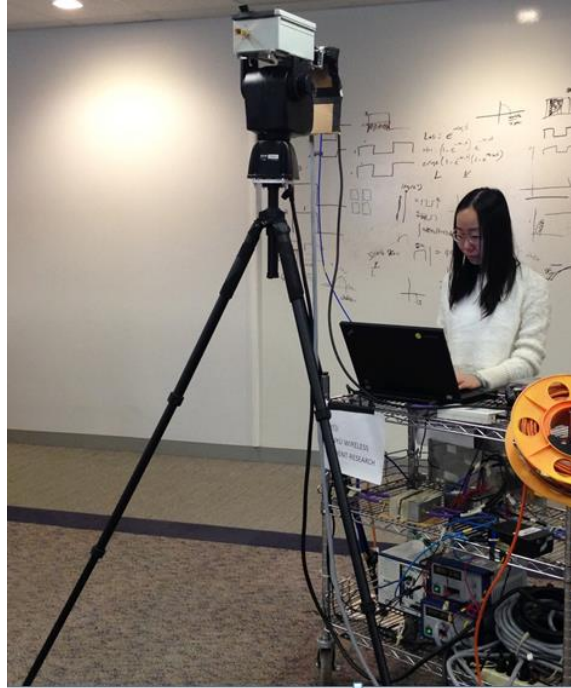


Fig. 3.9 Receiver setup for the antenna pattern measurements. The height of the receive antenna is 2 meters relative to ground.



Fig. 3.10 Antenna pattern measurement environment. The majority of surrounding furniture was at a height lower than the TX and RX antennas.

around 1.6 meters relative to the ground. Both the transmitter and receiver antennas were elevated to a height of two meters above ground, so as to conduct the measurements in a line-of-

sight environment. The wall located behind the receiver can cause relatively strong reflected multipath components perceived on recorded PDPs, thereby influencing the antenna pattern measurements. However, all recorded multipath components (originating from reflections) other than the main LOS peak, were disregarded in post-processing when recovering the antennas patterns. Only 20 dBi gain horn antennas for indoor measurements were characterized for this report.

#### a. Vertical-to-Vertical Antenna Pattern Measurements

In the vertical-to-vertical antenna pattern measurements, both the transmitter and receiver antennas were attached to the UG-385/U waveguide flanges on the up- and down-converters, already orientated for vertical polarization. Fig. 3.13 shows the 20 dBi antenna on the down-converter box with a waveguide twist, displaying how the converter boxes can affect the back-lobe measurements. At the beginning of the measurements, the transmitter and receiver antennas were pointed perfectly towards each other on boresight, in the azimuth and elevation planes with a T-R separation distance of four meters. Perfect boresight-to-boresight orientation was possible with the use of a high-powered laser pointer. The TX antenna remained fixed while the RX antenna was swept in the azimuth plane to determine the antenna azimuth HPBW. When the RX antenna is perfectly facing the TX antenna on boresight, the angle of arrival is  $0^\circ$ . Positive and negative measured angles correspond to the clockwise and counterclockwise azimuth directions of motion of the receiver antenna, respectively. For RX antenna azimuth ranges between  $-20^\circ$  and  $+20^\circ$ , PDPs were acquired in  $1^\circ$  azimuthal increments, resulting in 41 total PDPs for this angular range. From  $+25^\circ$  to  $+165^\circ$  and from  $-25^\circ$  to  $165^\circ$ , PDPs were recorded in  $5^\circ$  azimuthal increments, resulting in 58 additional PDPs. Then from  $+166^\circ$  to  $+180^\circ$  and from  $-166^\circ$  to  $-179^\circ$ , PDPs were recorded in  $1^\circ$  azimuthal increments, resulting in 29 more PDPs to carefully measure the back lobe properties of the antenna. Overall, 128 PDPs were

**V-V Radiation pattern for 73 GHz Indoor 20 dBi 15 ° HPBW antenna**

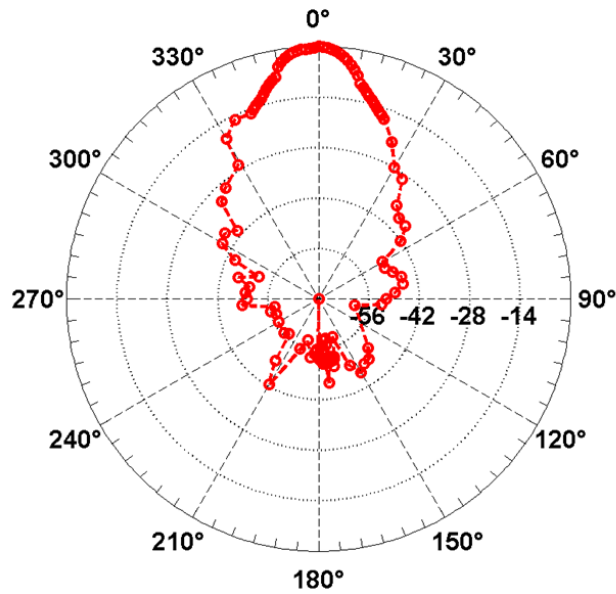


Fig. 3.11 Normalized antenna radiation pattern for vertical-to-vertical polarization. The estimated front-to-back ratio is around 40 dB. However, the converter box blocks some of the power to the back of the antenna, so the actual front-to-back ratio will realistically be lower than that measured.

**V-H Radiation pattern for 73 GHz Indoor 20 dBi 15 ° HPBW antenna**

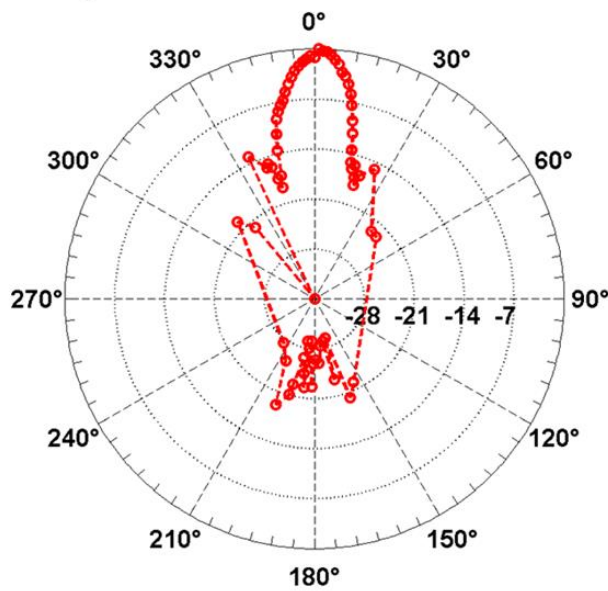


Fig. 3.12 Normalized antenna radiation pattern for vertical-to-horizontal polarization using 20 dBi gain pyramidal horn antennas at 73 GHz. The XPD for V-H polarization is 31 dB.

recorded over the entire 360° azimuth span for determining the antenna properties. Fig. 3.8, Fig. 3.9, and Fig. 3.10 display the measurement setup for the antenna pattern measurements for all

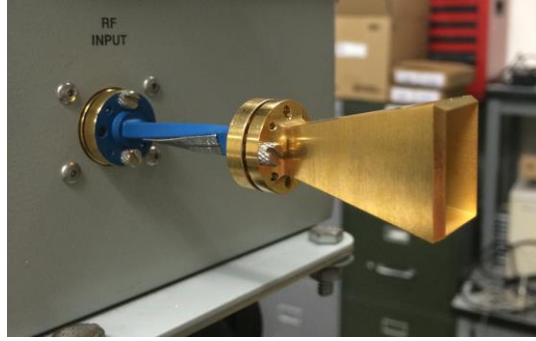


Fig. 3.13 The 20 dBi receive antenna for antenna pattern measurements attached to a 90° waveguide twister to change the antenna polarization to horizontal. The waveguide twister is attached to a UG-385/U flange on the down-converter box.

H-H Radiation pattern for 73 GHz Indoor 20 dBi 15 ° HPBW antenna

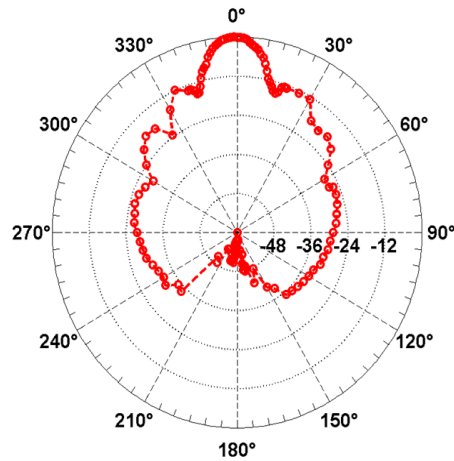


Fig. 3.14 Normalized antenna radiation pattern for horizontal-to-horizontal polarization using 20 dBi gain pyramidal horn antennas at 73 GHz.

Table 3.6 Dimensions of waveguide flange and the flared horn antenna used for antenna pattern measurements.

	Waveguide Flange (Model UG-385/U)	Pyramidal Horn Antenna (Model 261V)	Size Ratio
<b>Length</b>	3.759 mm $\approx 0.921\lambda$	20.638 mm $\approx 5.056\lambda$	5.49
<b>Width</b>	1.880 mm $\approx 0.460\lambda$	14.288 mm $\approx 3.500\lambda$	7.60

four scenarios tested. Fig. 3.11 shows the resulting antenna radiation pattern when the TX and RX antennas are vertically polarized. The front-to-back ratio was computed to be approximately 40 dB, a little larger than the manufacturer’s specification. Realistically the front-to-back ratio is lower due to the converter box obstructions that cannot be removed during these measurements.

#### b. Vertical-to-Horizontal Antenna Pattern Measurements

H-V Radiation pattern for 73 GHz Indoor 20 dBi 15 ° HPBW antenna

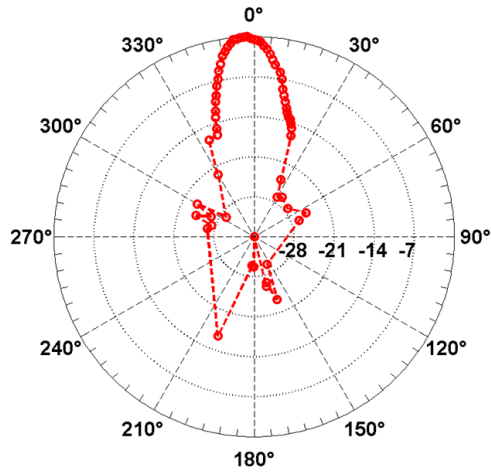


Fig. 3.15 Normalized antenna radiation pattern for horizontal-to-vertical polarization using 20 dBi gain pyramidal horn antennas at 73 GHz.

In the vertical-to-vertical antenna pattern measurements, the two antennas were co-polarized. For the vertical-to-horizontal antenna pattern measurements, the antenna pattern combination is considered cross-polarized. The cross-polarization pattern and subsequent measurements are important because in normal outdoor and indoor wireless communications, the polarization of a propagating wave may change due to encounters with obstructions in the channel. Cross-polarization measurements will allow us to determine the cross-polarization discrimination (XPD) factor, a critical property of antennas and isolation characteristics.

In order to have the receiver antenna horizontally polarized a 90° twisted waveguide is attached to the UG-385/U on the down-converter box, and the receiver antenna is attached to the other end of the waveguide. The transmit antenna remained vertically polarized. The procedure for recording PDPs for the vertical-to-horizontal antenna pattern measurements is identical to the procedure for measuring V-V polarization. As predicted, the received signal strength at identical angular increments is weaker for V-H polarization. Fig. 3.12 shows the vertical-to-horizontal

antenna pattern plot. Results indicated that the XPD factor for V-H as compared to V-V is approximately 31 dB.

#### c. Horizontal-to-Horizontal Antenna Pattern Measurements

After the vertical-to-horizontal measurements, an additional 90° waveguide twister was attached to the up-converter's UG-385/U flange to which the transmit antenna was attached to change the transmit antenna polarization to horizontal, for horizontal-to-horizontal antenna polarization measurements. Fig. 3.14 shows the radiation antenna pattern observed for H-H antenna polarizations. The same procedure was performed as done for the V-V case.

In the two co-polarization scenarios, V-V and H-H, the resulting antenna pattern plots show different lobe shapes. The rectangular waveguide flange type of the antenna is UG-385/U with an internal dimension of  $3.759 \times 1.880$  mm, and the horn antenna is flared in both directions. However, the horn antenna flares more in the direction of the E-plane than in the H-plane. Thus, the V-V polarization antenna pattern plot showed higher directivity than the H-H polarization antenna pattern. Table 2.1 lists the measured physical aperture of the antenna and the physical internal dimension of the waveguide flange.

#### d. Horizontal-to-Vertical Antenna Pattern Measurements

The final antenna pattern measurements were for the horizontal-to-vertical polarization scenario. The transmitter antenna was kept horizontally polarized with the use of a 90° waveguide twister, while the 90° waveguide twister was removed between the RX antenna and down-converter box so that the RX antenna was vertically polarized. The measurement procedure for the H-V scenario was identical to the previous three scenarios. Fig. 3.15 shows the antenna pattern for the H-V polarization scenario. Results indicated that the XPD factor for H-V as compared to H-H is approximately 27 dB. The measured HPBW from the previous four studies for V-V, V-H, H-H, and H-V were 15°, 13°, 14°, and 16°, respectively.

## 3.2 Measurement Descriptions

### 3.2.1 Indoor Measurement Environment and System Specifications

A sliding correlator channel sounder that consisted of 20 dBi gain transmit and receive antennas, each with 15° half power beamwidth (HPBW), was used for conducting the indoor office environment measurements. The specifications of the channel sounder system and some of the hardware used for the indoor measurements can be found in Table 3.7. The indoor measurements consisted of the TX equipment, specifically the up-converter and horn antenna at a height of 2.5 meters relative to the ground (near the ceiling), mounted on top of an electronically-controlled gimbal that was mounted to a pneumatic mast, in order to emulate



Fig. 3.16 Transmitter located at the indoor MTC1 location with the antenna attached to the up-converter box that is mounted on top of a steerable gimbal, which is mounted on top of a pneumatic mast to reach the height of 2.5 meters.



Fig. 3.17 Receiver location for one of the MTC1 TX site measurements with the antenna attached to the down-converter box that is mounted on top of a steerable gimbal that is mounted on top of a tripod to reach a height of 1.5 meters.

Table 3.7 Channel sounder specifications and settings for the indoor measurements.

<b>Carrier Frequency</b>	73.5 GHz
<b>Pseudorandom Noise (PN) Sequence Length</b>	$2^{11}-1 = 2047$
<b>PN Sequence Clock Rate at TX</b>	400 MHz
<b>PN Sequence Clock Rate at RX</b>	399.95 MHz
<b>Slide Factor</b>	8000
<b>RF Null-to-Null Bandwidth</b>	800 MHz
<b>TX/RX IF Frequency</b>	5.625 GHz
<b>TX/RX LO Frequency</b>	22.625 GHz
<b>Multipath Time Resolution</b>	2.5 ns
<b>Transmitter Power</b>	- 7.9 / 2.1 dBm
<b>TX IF power</b>	- 40.2 / -30.2 dBm
<b>TX/RX LO power</b>	10 dBm
<b>Noise Floor</b>	-110 dBm
<b>Maximum Measurable Path Loss</b>	152 dB
<b>TX/RX Antenna</b>	20 dBi horn antenna with 15° HPBW
<b>Polarization</b>	V-V and V-H
<b>RX Azimuth Angular Steps</b>	15° increments for 20 dBi horn antenna
<b>TX-RX Synchronization</b>	Unsupported
<b>TX Antenna Height</b>	2.5 meters
<b>RX Antenna Height</b>	1.5 meters

typical access point heights and locations of typical office buildings. Fig. 3.16 shows the transmitter setup for the MTC1 transmitter location. The receiver was at a height of 1.5 meters relative to the floor level in order emulate cubicle heights and human heights, typical levels of where desktop and mobile equipment are located.

During measurements, the receiver was located around the office space at a height of 1.5 meters relative to the ground. The horn antenna at the receiver was attached to the down-converter box that was mounted to a steerable gimbal that was fixed to a tripod. Fig. 3.3 shows the receiver setup at one of the RX locations for the MTC1 measurements.

The 9<sup>th</sup> floor of 2 MetroTech Center is a typical indoor office environment that contains cubicle walls, wooden walls, doors, offices, and closets. Two TX locations (MTC1 and MTC2) and 21 RX locations (RX 1 to RX 22, excluding RX 10) were chosen for LOS and NLOS measurement scenarios. There are only 21 RX locations, as the RX 10 location resulted in faulty data and therefore was not included for results and analysis. The map of the TX and RX locations of the 73 GHz indoor measurement campaign is shown in Fig. 3.18. The T-R separations and propagation environments of the indoor measurements are summarized in Table

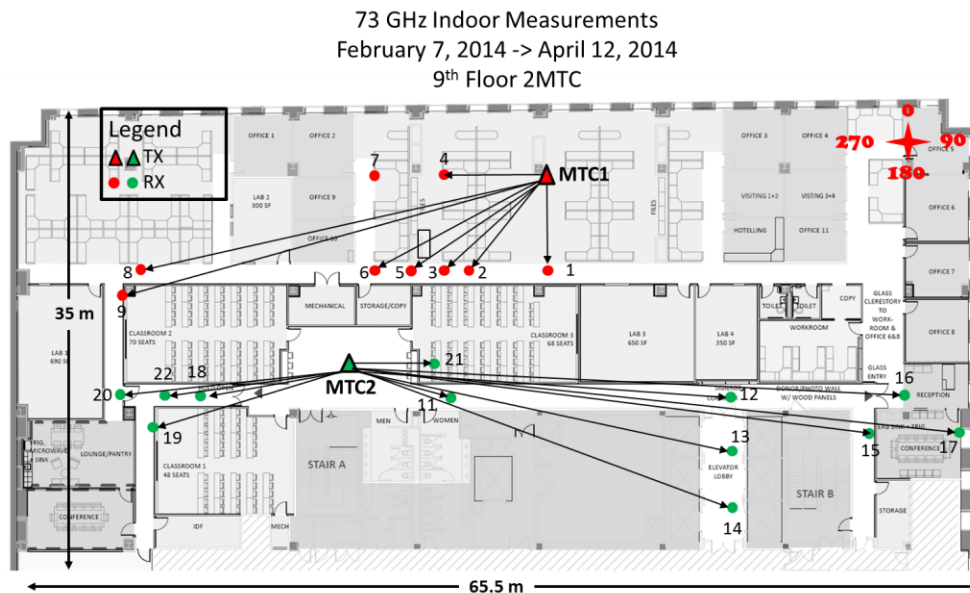


Fig. 3.18 Map of the indoor measurement office environment layout on the 9th floor of 2 MetroTech Center with transmitter locations represented as triangles and receiver locations represented as dots. The first TX location is MTC1 in the map and is marked in red. The red dots 1 to 9 represent RX locations for RX1 to RX9 for the measurements conducted with MTC1 as the TX location. The second TX location is MTC2 and is marked in green. The green dots 11 to 22 represent RX locations for RX 11 to RX 22 for the measurements conducted with MTC2 as the TX location. Note that RX 10 does not appear on this map as those measurements were invalid and thus not used for results and analysis.

3.8. In Table 3.8 a LOS environment describes a scenario where there are no obstructions between the TX and RX antenna, even if the antennas were not perfectly facing each other boresight-to-boresight. If obstructions existed between the transmitter and receiver such that no LOS path existed between the two, then that TX-RX combination was considered a NLOS environment.

For the MTC1 TX location, 9 RX locations (including both LOS and NLOS environments) were selected to study the reflection and penetration properties of indoor materials and the overall channel characteristics of the 73 GHz frequency band in an office building. The LOS locations included RX 1, RX 4 and RX 7. While cubicle walls separated the MTC1 TX location from RX 4 and RX 7, no obstructions exist between the TX and RX antennas as the cubicle wall height is only 1.6 m whereas the TX antenna was at 2.5 m relative to ground and the RX antenna was at 1.5 m relative to ground. Therefore, RX 4 and RX 7 were considered LOS environments. RX 2 was behind one cubicle, RX 3 was behind two cubicles. RX 5 was located along the hallway behind two cubicle walls and one wooden wall. RX 6 was behind three cubicle walls and one wooden wall along the hallway. RX 8 was at the far end of the hallway, and RX 9 was located at the corner of the hallway.

For the MTC2 TX location, 12 RX locations were selected to study the reflection and penetration properties of indoor materials as well as channel characteristics of the 73 GHz frequency band in a typical office environment. RX 11 and RX 12 were located in a long corridor hallway. RX 13 and RX 14 were located in a side hallway off the main corridor separated by a wooden door with glass windows. RX 15 was located around the corner at the far end of the long corridor down a small hallway. RX 16 was behind a glass at the far end of the corridor hallway, and RX 17 was located in a conference room. RX18 and RX 22 were behind a

Table 3.8 TX-RX location combination environment descriptions, T-R separation distances, and calibration and measurement powers used for the indoor measurements.

TX ID	RX ID	Transmit Power for Calibration (dBm)	Transmit Power for Measurements (dBm)	T-R Separation Distance (m)	Propagation Environment
MTC1	1	-7.9	-7.9	6.4	LOS
	2		-7.9	7.8	NLOS
	3		-7.9	10.1	NLOS
	4		-7.9	7.9	LOS
	5		-7.9	11.9	NLOS
	6		-7.9	14.4	NLOS
	7		-7.9	12.9	LOS
	8		-7.9	29.5	NLOS
	9		-7.9	32.9	NLOS
MTC2	11	-7.9	2.1	9.0	NLOS
	12		2.1	28.5	NLOS
	13		2.1	29.2	NLOS
	14		2.1	30.4	NLOS
	15		2.1	39.2	NLOS
	16		2.1	41.9	NLOS
	17		2.1	45.9	NLOS
	18		2.1	12.1	NLOS
	19		2.1	15.5	NLOS
	20		2.1	17.1	NLOS
	21		2.1	6.7	NLOS
	22		2.1	14.8	NLOS

metal door along the main hallway, and RX 19 was behind the same metal door and around a corner in the hallway. RX 20 was behind two metal doors, and RX 21 was in a classroom very close to the MTC2 transmitter.

### 3.2.1.1 Measurement Descriptions for the MTC1 Transmitter

The measurements for the MTC1 transmitter location were conducted on February 7<sup>th</sup>, March 1<sup>st</sup>, April 4<sup>th</sup>, 5<sup>th</sup>, and 11<sup>th</sup> in the year 2014. On February 7<sup>th</sup> 2014, RX measurement sweeps were performed at RX locations 1 through 9. Initially, the TX and RX antennas were set to face boresight-to-boresight in the azimuth and elevation planes and with the TX antenna vertically polarized and the RX antenna horizontally polarized. The initial boresight-to-boresight angles relative to the compass on the map in Fig. 3.18 are listed in Table 3.9. On March 1<sup>st</sup> 2014, measurement sweeps were performed at RX locations 1 through 9 for both vertically polarized

TX and RX antennas and the same initial boresight-to-boresight angle settings explained in Table 3.9.

On April 4<sup>th</sup>, 5<sup>th</sup>, and 11<sup>th</sup> 2014, 11 different measurement sweep configurations were conducted for each TX-RX location combination for RX locations 1 through 9. The TX and RX antennas were both vertically polarized for all configurations. Measurements 1 and 2 were RX azimuth sweeps with the RX antenna elevation 5° above and below the initial boresight-to-boresight elevation angle found with the TX antenna, while the TX antenna remained fixed,

Table 3.9 Initial boresight-to-boresight azimuth angles and elevation angles for the MTC1 transmitter and corresponding receiver locations RX 1 through RX 9. The azimuth angles are relative to the compass shown in Fig. 3.18. The elevation angles are relative to a plane parallel to the floor of the measurement environment, where uptilt refers to positive angles and downtilt refers to negative angles relative to the plane parallel to the floor.

<b>RX ID</b>	<b>TX Azimuth (°)</b>	<b>TX Elevation (°)</b>	<b>RX Azimuth (°)</b>	<b>RX Elevation (°)</b>
1	180	-10	0	10
2	216	-10	36	8
3	236	-10	53	5
4	270	-7	90	7
5	238	-5	58	5
6	244	-4	64	4
7	270	-5	90	5
8	258	-2	78	2
9	256	-2	76	2

Table 3.10 Initial boresight-to-boresight azimuth angles and elevation angles for the MTC2 transmitter and corresponding receiver locations RX 11 through RX 21. The azimuth angles are to the compass shown in Fig. 3.18. The elevation angles are relative to a plane parallel to the floor of the measurement environment, where uptilt refers to positive angles and downtilt refers to negative angles relative to the plane parallel to the floor

<b>RX ID</b>	<b>TX Azimuth (°)</b>	<b>TX Elevation (°)</b>	<b>RX Azimuth (°)</b>	<b>RX Elevation (°)</b>
11	108	-6	288	6
12	96	-2	276	2
13	104	-2	284	2
14	111	-2	191	2
15	99	-1	279	1
16	94	-1	274	1
17	96	-1	276	1
18	257	-5	77	5
19	250	-4	70	4
20	262	-3	82	3
21	90	-9	270	9
22	261	-4	81	4

pointing at the initial boresight-to-boresight angle in the azimuth and elevation planes towards the RX. Measurements 3 and 4 consisted of RX sweeps with the RX antenna elevation at the boresight-to-boresight angle relative to the TX antenna, while the TX antenna remained fixed, pointing in the boresight-to-boresight azimuth direction, but with the elevation angle  $5^\circ$  above and below the initial boresight-to-boresight elevation angle. Measurement 5 was a TX azimuth sweep with the TX antenna elevation fixed at the boresight-to-boresight elevation angle, where the RX antenna remained fixed, pointing at the initial boresight-to-boresight angle in the azimuth and elevation planes. Measurement 6 was a RX azimuth sweep with the RX antenna elevation pointing at the initial boresight-to-boresight elevation angle, but now the TX antenna azimuth remained fixed at a second strong angle of departure (AOD) noticed during the Measurement 5 TX sweep, but with the same antenna elevation fixed at the boresight-to-boresight elevation angle. Measurements 7 and 8 were RX sweeps with the RX elevation angle fixed  $15^\circ$  above and below the boresight-to-boresight elevation angle, with the TX antenna pointing in the initial boresight-to-boresight angle in the azimuth and elevation planes. Measurements 9 and 10 were RX azimuth sweeps with the RX antenna azimuth set at the boresight-to-boresight elevation angle while the TX antenna remained fixed in the boresight-to-boresight azimuth plane but the elevation angle was set to  $15^\circ$  above and below the boresight-to-boresight elevation angle. Measurement 11 consisted of a TX azimuth sweep with the elevation angle pointing in the strongest elevation plane determined during measurements 9 and 10. For measurement 11, the RX antenna remained fixed at the initial boresight-to-boresight angles in the azimuth and elevation planes. Polarization diversity measurements were only conducted for the MTC1 transmitter and receiver combinations.

### ***3.2.1.2 Measurement Descriptions for the MTC2 Transmitter***

The measurements for the MTC2 transmitter location were conducted on February 28th and April 12th 2014. All of the measurements for the MTC2 transmitter location consisted of vertically polarized TX and RX antennas. On February 28th 2014, point-to-point measurements at receiver locations RX 11 through RX 22 were performed. The TX and RX antennas were pointed perfectly boresight-to-boresight in the azimuth and elevation planes. For each of these point-to-point TX-RX location combinations, three PDPs were acquired for analysis. The initial boresight-to-boresight azimuth angles and elevation angles for MTC2 transmitter measurements for RX 11 through RX 22 are listed in Table 3.10.

On April 12<sup>th</sup> 2014, eight different measurement configurations were performed for receiver locations RX12, RX13, RX15, RX16, RX21, RX22 corresponding to the MTC2 transmitter location. Measurement 1 was a RX azimuth sweep with the TX and RX antennas initially pointed at each other perfectly boresight-to-boresight in the azimuth and elevation planes. Measurements 2 and 3 were RX azimuth sweeps with the RX antenna elevation 15° above and below the initial boresight-to-boresight elevation angle set during measurement 1, while the TX antenna remained fixed, pointing at the initial boresight-to-boresight angle in the azimuth and elevation planes towards the RX. Measurements 4 and 5 consisted of RX sweeps with the RX antenna elevation set to the boresight-to-boresight angle relative to the TX antenna, while the TX antenna remained fixed, pointing in the boresight-to-boresight azimuth direction, but with the elevation angle 15° above and below the initial boresight-to-boresight elevation angle. Measurement 6 was a TX azimuth sweep with the TX and RX antennas initially pointing at each other perfectly boresight-to-boresight in the azimuth and elevation planes. Measurement 7 was a RX azimuth sweep with the RX antenna initially pointed at the boresight angles in the azimuth

and elevation planes while the TX antenna remained fixed, pointing at the strongest receive power in the azimuth and elevation plane determined during measurement 6. Measurement 8 consisted of another TX azimuth sweep with the RX antenna pointing at the initial boresight-to-boresight angles in the azimuth and elevation planes, while the TX antenna swept in the azimuth plane, but set to the strongest elevation angle determined during measurements 4 and 5. Polarization diversity measurements were *NOT* conducted for the MTC2 transmitter and receiver combinations

### **3.2.2 Outdoor Measurement Campaign**

The 73 GHz outdoor measurements consisted of free space, foliage, and ground bounce in foliage measurements that were conducted in the MetroTech Commons Courtyard in Downtown Brooklyn on January 13<sup>th</sup> and 15<sup>th</sup>, and May 2<sup>nd</sup> and 11<sup>th</sup> in the year 2014. Both the free space and foliage measurements were performed for V-V and V-H antenna polarizations. All outdoor measurements employed 27 dBi gain, 7° HPBW directional pyramidal horn antennas, different than those used during indoor measurements. The free space and foliage measurements each consisted of four TX-RX location combinations for T-R separation distances of 10, 20, 30, and 40 meters. For the foliage measurements, the foliage consisted of cherry trees, with common cherry tree leaves and blossoms. The height of the trees was approximately 6 meters relative to the ground. The length of the leaves was between 7-14 cm when the trees were fully blossomed, and the cherry blossom size ranged from 6 -12 cm in size.



Fig. 3.19 Photo of the free space measurement layout in front of the Bern Dibner Library on the MetroTech Commons Courtyard.

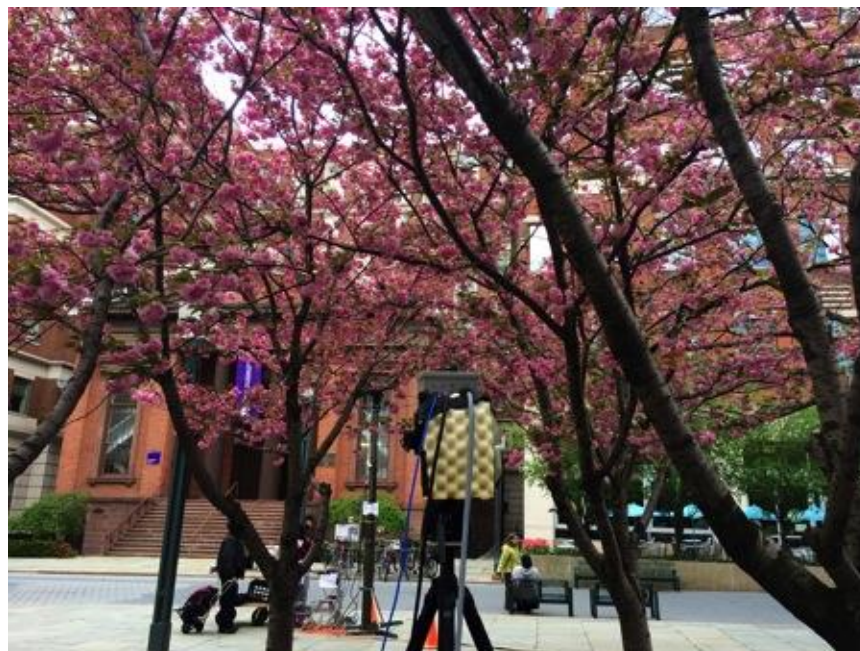


Fig. 3.20 Photo of a foliage measurement with the receiver located under the canopy of the cherry tree branches and leaves. The cherry tree leaves are about 7-14 cm when fully blossomed and the cherry flower blossoms had a diameter of 6-12 cm when fully blossomed.



Fig. 3.21 Photo of the foliage measurement ground bounce surface (soil / dirt / gravel) at the MetroTech Commons Courtyard, located between the trees and beneath the branch canopy.

Table 3.11 Channel sounder specifications for outdoor propagation measurements.

<b>Carrier Frequency</b>	73.5 GHz
<b>Pseudorandom Noise (PN) Sequence Length</b>	$2^{11}-1 = 2047$
<b>PN Sequence Clock Rate at TX</b>	400 MHz
<b>PN Sequence Clock Rate at RX</b>	399.95 MHz
<b>Slide Factor</b>	8000
<b>RF Null-to-Null Bandwidth</b>	800 MHz
<b>TX/RX IF Frequency</b>	5.625 GHz
<b>TX/RX LO Frequency</b>	22.625 GHz
<b>Multipath Time Resolution</b>	2.5 ns
<b>Transmitter Power</b>	- 7.9 dBm
<b>TX IF power</b>	- 40.2 dBm
<b>TX/RX LO power</b>	10 dBm
<b>Noise Floor</b>	-110 dBm
<b>Maximum Measurable Path Loss</b>	156 dB
<b>TX/RX Antenna</b>	27 dBi horn antenna with 7°HPBW
<b>Polarization</b>	V-V and V-H
<b>RX Azimuth Angular Steps</b>	10° / 8° for 27 dBi horn antenna
<b>TX-RX Synchronization</b>	Unsupported

For both the free space and foliage measurements, the receivers were set to heights of 2 meters relative to ground to simulate mobile users. The transmitter height was set to 4.06 meters relative



Fig. 3.22 Map of the TX and RX locations for the outdoor free space measurements. The T-R separation distance between TX1 and RX1 is 10 meters, and an additional 10 meters separation exists for each subsequent RX location.



Fig. 3.23 Map of the TX and RX locations for the outdoor foliage and ground bounce measurements. The T-R separation distance between TX1 and RX1 is 10 meters, and an additional 10 meters separation exists for each subsequent RX location. The foliage type is cherry trees with leaves and flower blossoms.

to ground in order to simulate a lamppost level access point in a common courtyard setting in a dense urban downtown environment.

### 3.2.2.1 Measurement Environment and System Specifications

The channel sounding system specifications used in the outdoor measurements are shown in Table 3.11 and are almost identical to the settings for the indoor measurements, the main

difference being the use of higher gain, more narrowbeam directional horn antennas. The map of the TX and RX locations of the 73 GHz outdoor (free space and foliage) measurements is shown in Fig. 3.22. Although from Fig. 3.22 and Fig. 3.23 it appears that the TX and RX locations for located in free space environments, the RX locations are covered by foliage in Fig. 3.23 and are not in Fig. 3.22, whereas the TX is never covered by foliage. The TX and RX locations for free space measurements were in an open area in front of the Bern Dibner building. The TX location for the foliage measurements was located in an open area while the RX locations were located underneath the cherry tree canopies. As previously described, The T-R separation distances were the same for both the free space and foliage measurements. For each scenario, the TX and 4 RX locations were aligned with the TX location with T-R separation distances of 10, 20, 30 and 40 meters. Fig. 3.22 and Fig. 3.23 show the relative position of the TX and RX in the courtyard for

Table 3.12 Summary of the TX and RX locations, environments, and system settings for the outdoor free space and foliage measurements.

<b>TX ID</b>	<b>RX ID</b>	<b>Polarization Type</b>	<b>Transmit Power In Calibrations (dBm)</b>	<b>Transmit Power In Measurements (dBm)</b>	<b>T-R Separation (m)</b>	<b>Propagation Environment</b>
CMN_FS1	1	V/H	-17.9	-7.9	10	LOS
	2				20	LOS
	3				30	LOS
	4				40	LOS
CMN1	1	V/H	-17.9	-7.9	10	NLOS
	2				20	NLOS
	3				30	NLOS
	4				40	NLOS

Table 3.13 The rotation step, sweep type, and initial boresight-to-boresight angles for the free space measurements at receivers RX 1 through RX 4 at the CMN\_FS1 TX location. The azimuth angles are with respect to true north. The elevation angles are with respect to horizon where negative angles refer to downtilt and positive angles refer to uptilt.

<b>RX ID</b>	<b>Rotation step for VV/VH (°)</b>	<b>Sweep Type</b>	<b>TX Azimuth (°)</b>	<b>TX Elevation (°)</b>	<b>RX Azimuth (°)</b>	<b>RX Elevation (°)</b>
1	8/10	RX Sweep	273	-10	93	10
2	10/10	RX Sweep	273	-6	93	6
3	10/10	RX Sweep	273	-4	93	4
4	10/10	RX Sweep	273	-3	93	3

both scenarios. The T-R separation distances, propagation environments, and antenna polarizations of the outdoor measurements are summarized in Table 3.12. The same rules for LOS and NLOS environments apply here such that an environment is LOS when no obstructions exist between the point-to-point path from the TX to RX. In NLOS environments, obstructions such as trees or lampposts exist between the straight point-to-point path between the TX and RX.

### ***3.2.2.2 Free Space Measurement Descriptions for the CMN\_FS1 Transmitter***

The free space measurements were conducted for the CMN\_FS1 TX location on January 13<sup>th</sup> and 15<sup>th</sup> 2014. Vertical-to-vertical polarization measurements were conducted on January 13<sup>th</sup> 2014 and V-H polarization measurements were performed on January 15<sup>th</sup> 2014. During measurements, the TX was lifted to the height of a common lamppost (about 4.06 m) and the RX remained at 2 meters above ground. Only one RX sweep was performed with the initial TX and RX antennas facing perfectly towards each other on boresight in the azimuth and elevation planes. For the RX sweeps, the TX antenna remained fixed in the azimuth and elevation planes, while the RX antenna swept in the azimuth plane in specific angular increments as specified in Table 3.13. The rotation step size, sweep type, and initial boresight-to-boresight angles for the free space measurements conducted for the CMN\_FS1 TX location and RX 1 through RX 4 receiver locations are described in Table 3.13.

### ***3.2.2.3 Foliage and Ground Bounce Descriptions for the CMN1 Transmitter***

The foliage measurements for the CMN1 TX were conducted on May 2<sup>nd</sup> and 11<sup>th</sup> 2014. Vertical-to-vertical polarization measurements were conducted on May 2<sup>nd</sup> 2014 and Vertical-to-horizontal measurements were performed on May 11<sup>th</sup> 2014. During measurements, the TX was lifted to the height of a common lamppost (about 4.06 m) and the RX remained 2 meters above ground, but covered by the foliage. 11 measurement configurations were conducted for the

foliage campaign for both the V-V and V-H antenna polarization settings. Perfect ground bounce measurements were recorded through the foliage between the TX and RX for Measurement 7 described below. The following is the description of each of the 11 measurements performed.

- *Measurement 1:* TX and RX antennas initially pointed towards each other perfectly on boresight in the azimuth and elevation planes. With the TX antenna fixed, the RX antenna was swept in the azimuth plane in  $10^\circ$  increments.
- *Measurement 2:* From the initial boresight elevation angle the RX antenna is uptilted  $7^\circ$  and swept in the azimuth plane in  $10^\circ$  increments while the TX antenna remained fixed in the same azimuth and elevation orientation from Measurement 1.
- *Measurement 3:* From the initial boresight elevation angle the RX antenna is downtilted  $7^\circ$  and swept in the azimuth plane in  $10^\circ$  increments while the TX antenna remained fixed in the same azimuth and elevation orientation from Measurement 1.
- *Measurement 4:* The RX antenna is initially set back to the original boresight-to-boresight azimuth and elevation orientation and swept in the azimuth plane in  $10^\circ$  increments while the TX antenna was fixed in the same azimuth plane as Measurement 1, however the elevation angle was uptilted  $7^\circ$  relative to the elevation in Measurement 1.
- *Measurement 5:* The RX antenna is initially set back to the original boresight-to-boresight azimuth and elevation orientation and swept in the azimuth plane in  $10^\circ$  increments while the TX antenna was fixed in the same azimuth plane as Measurement 1, however the elevation angle was downtilted  $7^\circ$  relative to the elevation in Measurement 1.
- *Measurement 6:* The TX and RX antennas are initially set back to the perfect boresight-to-boresight orientations in the azimuth and elevation plane, and the TX antenna is swept in the azimuth plane in  $10^\circ$  increments.
- *Measurement 7:* Both the TX and RX antennas were downtilted such that the transmitted signal reflected on the ground and bounced back into the receive antenna (a ground bounce propagation scenario). The downtilted angles were calculated for measurements and are in Table 3.15. A depiction of the ground bounce scenario is in Fig. 3.24.
- *Measurement 8 to 11:* With the TX azimuth angles fixed to those described in Table 3.14 and the TX elevation angles fixed to those described in Table 3.15 and Table 3.16. RX elevation sweeps were performed in  $7^\circ$  uptilted increments below the horizon for each measurement such that RX 1 had five sweeps, RX 2 had three sweeps, RX 3 had two sweeps, and RX 4 had two sweeps.

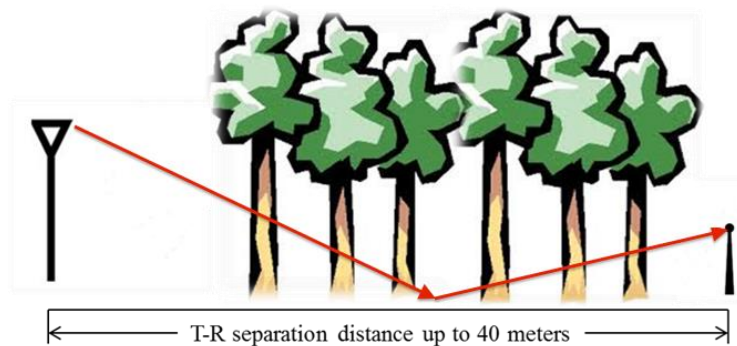


Fig. 3.24 Depiction of the ground bounce scenario through foliage between a TX and RX.

Table 3.14 The rotation step, sweep type, and initial boresight-to-boresight angles for RX 1 to RX 4 for the CMN TX location. The azimuth angles are with respect to true north. The elevation angles are with respect to horizon where negative angles refer to downtilt and positive angles refer to uptilt.

RX ID	Rotation step for VV/VH (°)	TX Azimuth (°)VV/VH	TX Elevation (°)VV/VH	RX Azimuth (°)VV/VH	RX Elevation (°) VV/VH
1	10/10	260/263	-11	80/83	-11
2	10/10	270/270	-6	90/90	6
3	10/10	271/271	-4	91/91	4
4	10/10	272/272	-3	92/92	3

Table 3.15 Initial TX and RX downtilt angles for different T-R separation distances for measurements 8 through 11, as well as the ground bounce downtilt elevations for measurement 7.

RX ID	T-R Separation Distance (m)	TX Downtilt Angle(°)	RX Downtilt Angle(°)
1	10	-30	-30
2	20	-17	-17
3	30	-11	-11
4	40	-9	-9

Table 3.16 TX and RX downtilt angles for different T-R separation distances for measurements 8 through 11.

RX ID	T-R Separation Distance (m)	Measurement Number	TX Downtilt Angle (°)	RX Downtilt Angle (°)
1	10	8	-30	-30
		9	-23	-30
		10	-16	-30
		11	-9	-30
2	20	8	-17	-17
		9	-10	-17
		10	-6	-17
3	30	8	-11	-11
		9	-4	-11
4	40	8	-9	-9
		9	-2	-9

## **Chapter 4 Data Post-Processing**

### **4.1 Overview of Data Acquisition**

As previously described, individual PDPs were recorded for many T-R separation distances, environments, polarizations, and angular settings, resulting in the processing of a few thousand PDPs to produce results and analysis. The receiver system consists of many different amplifiers attenuators, and other components, as well as processes such as the cross-correlation that provide an overall RX system gain to the recorded signal. Therefore it is essential for us to be able to recover the true received power and subsequent PDP for each measurement, based on the RX system gain, since the RX system gain has a specific linear range of operation where an input signal attenuated by 1 dB results in an observed signal that is 1 dB lower. A calibration routine was performed daily before and after measurements to ensure that PDPs were recorded within the operating linear range of the RX system and also in order to determine the RX system gain of that day to recover true received power. Calibration routines were performed in a LOS environment at a known distance in the far-field so as to accurately determine the RX system linear range and gain. The calibration routine will be discussed next.

### **4.2 Calibration Routine**

The calibration routine performed at the beginning and end of every measurement day allowed us to determine the linear range and gain of the RX system in order to recover true received power for each PDP recorded. The calibration routine was performed for a T-R separation distance of 4 meters in a LOS environment with the TX and RX antennas pointing perfectly boresight-to-boresight in the azimuth and elevation planes. The T-R separation distance is close enough for accurate point-to-point measurements and also far enough such that the TX

and RX antennas are both operating in the Fraunhofer far-field regions. During the calibration routine, a power delay profile was acquired for eight different RX variable attenuator settings, ranging from 0 dB to 70 dB in steps of 10 dB. For each acquired profile, the measured received powers in the LOS component are computed and plotted against the corresponding variable attenuator setting, as shown in Fig. 4.1.

The LOS component in the acquired PDP should experience the theoretical free space path loss observed at 4 meters with the induced attenuation setting.

The linear range is then determined from Fig. 4.1 and is approximated using a linear fit, whose slope should theoretically be -1. In the plot below, the slope was found to be -1.01, which is very close to the theoretical value. The slope of the line is found using MATLAB's *polyfit* command for all possible RX attenuator setting ranges between 0 dB and 70 dB. The *polyfit* line that produces a slope closest to -1 is used to determine the RX system gain for recovering true

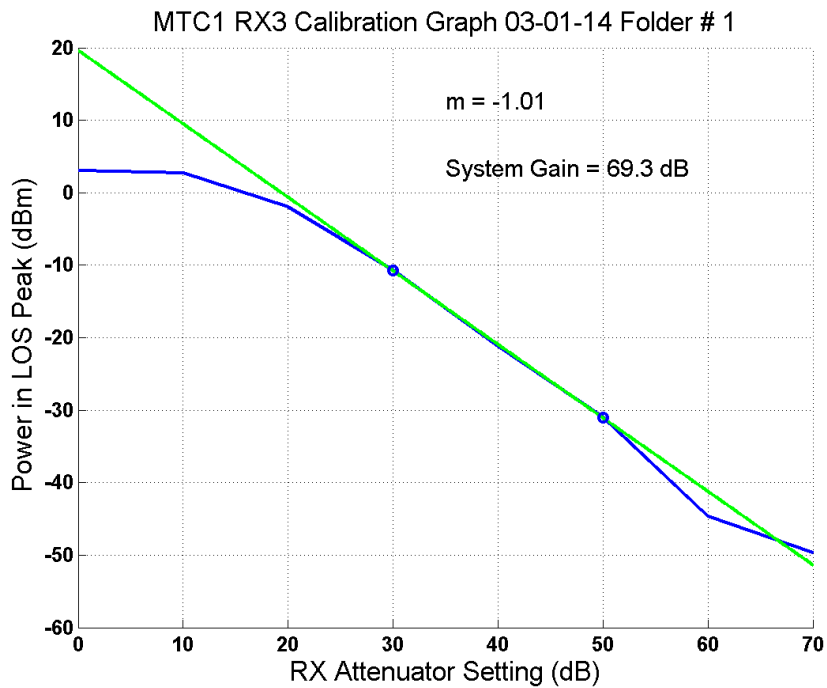


Fig. 4.1 Sample calibration graph.

received power for the measurements of that day. From the linear equation, the RX system gain is easily recovered by taking the difference between the theoretical free space received power at the calibration distance, and the intercept of the linear fit. The difference between the received power in calibration and intercept value is the RX system gain, which can be expressed as the following formula,

$$G_{RX} = Int - P_{cal} \quad (4.1)$$

where  $Int$  represents the intercept value obtained from the fit line, and  $P_{cal}$  is the received power at  $d_0$  computed from the free space path loss formula. The resulting gain  $G_{RX}$  of the RX system is then removed from every raw PDP recorded from that day in order to recover true received power, and RF PDPs. Overall, it should be noted that this RX system gain includes gains from amplifiers as well as the processing gain induced by the sliding correlator operation.

### 4.3 PDP Thresholding Algorithm

Each recorded raw PDP was thresholded so as to only keep observable multipath components above the noise floor for further processing and analysis. The first step was to find the mean noise floor in mW of each individual PDP, convert that to log scale and then set a threshold of 5 dB above the mean noise floor such that all signal components kept, have at least 5 dB of SNR. The mean noise floor was obtained by taking the mean of the samples located between 1600 and 1800 ns of the recorded time arrays. All samples of the PDP below this threshold were manually given a low value of -200 dBm. (effectively setting them to 0 power). All sample points above this 5 dB SNR threshold were considered valid signals. After thresholding, all valid signal samples above the threshold had the RX calibration gain in dB subtracted from them so as to recover the true RF PDP.

## 4.4 Measurement Log Sheets

Log sheets were an essential part of every measurement and recorded PDP. Log sheets were used to keep track of measurement dates, measurement times, hardware and software settings, power levels, calibration information, as well as acquisition trigger levels, and azimuth and elevation angles of each measurement. Fig. 4.2 is an example of a handwritten *calibration* log sheet, and Fig. 4.3 is an example of a handwritten *measurement* log sheet. The measurement log sheets have similar sections, although the measurement log sheets contain more information for each individual measurement.

The measurement number was used to identify each measurement. For each TX-RX location combination, different measurements were performed such as TX and RX sweeps for different angle conventions. Thus, the log sheets helped in organizing information for post-processing

Calibration Log Sheet

Date	03.01.2014		Time	10:45	
Folder #	1				
TX ID	MTC1		RX ID	1	
TX-RX Combined Antenna Gain (dBi)	40		TX-RX Distance (m)	4	
TX Attenuation (dB)	30	TX IF Power (QuickSyn) (dBm)	9.6	TX RF Power (dBm)	-7.87
RX Attenuation (dB)	Trigger Level (V)	Vertical Range	Linear Range (dB)		
0	0.1	0.3	20-50		
10	0.1	0.3			
20	0.06	0.18			
30	0.02	0.07			
40	0.0063	0.023			
50	0.002	0.02			
60	0.001	0.02			
70	0.0006	0.02			
Power	-19.6787				
Slope	-0.9440				
Intercept	15.049				
Notes					

Fig. 4.2 Sample calibration log sheet.

purposes.

In this project, a pair of horn antennas with 20 dBi of gain were used in indoor measurements, which had a combined gain of 40 dB. This value is important in the calculation of theoretical received power during calibration, and is:

$$P_{cal} = P_t + G_t + G_r - PL_{ref} \quad (4.2)$$

where  $P_t$  is the transmitted power in calibration,  $G_t$  and  $G_r$  are the transmit and receive antenna gains, and  $PL_{ref}$  is the free space path loss reference at four meters.

Measurement Log Sheet

RX Azimuth Sweep

Date	03.01.2014		Time	12:52	
Measurement #	1		Track #	1	
TX RF Power (dBm)	-78.7		Combined Antenna Gain (dBi)	40	
	Latitude		Longitude		
TX					
RX					
TX ID	Azimuth	Elevation	RX ID	Azi (0°)	Elevation
1	151°	-5°	5	331°	5°
Zero Position of Gimbal			0°		
Linear Range Trigger Level (V)					
Rotation #	Displayed Azi	Actual Azi	Trigger Level	Notes	
Steps: 15°					
0			0.018		
1			0.018		
2			0.0063		
3			0.0041		
4			0.0034		
5			0.0047		
6			0.0019		
7			0.0038		
8			0.0041		
9			0.0039		
-1			0.02		
-2			0.036		
-3			0.005		
-4			0.0062		
-5			0.011		
-6			0.0037		
-7			0.0018		
-8			0.0037		
-9			0.0023		
-10			0.006		

Fig. 4.3 Sample measurement log sheet.

The transmit power was also a very important parameter in data processing. In this project, the indoor measurements used -7.9 dBm and +2.1 dBm transmit power for two sets of measurements, and foliage measurements used -7.9 dBm as the transmit power level. The initial pointing angles of the TX and RX antennas in the azimuth plane are also important parts of the log sheets, as this assists in post-processing for determining the exact pointing angles of the TX and RX antennas with respect to true north. For example, if the initial pointing angle of the RX antenna with respect to true north is denoted as  $\theta_0$ , which is the rotation 0 pointing direction, then the  $n^{\text{th}}$  rotation will generate a pointing angle with respect to north as:

$$\theta_{RX} = \theta_0 - 15n \quad (4.3)$$

where  $n$  is the rotation number of a measurement and can be either positive or negative. When  $n$  is positive, the rotation direction is counterclockwise; when  $n$  is negative, the antenna is rotated clockwise. The number 15 is the antenna rotation step increment in degrees, which is the same as the antenna's HPBW for the 20 dBi gain antennas used for the indoor measurements.

## 4.5 Hierarchical Structure of Raw Data

Due to the complexity of the measurements performed at each receiver location (various angle combinations and measurement configurations, etc.), the collected data needs to be organized in a hierarchy structure for clear identification and easy access. In this section, the hierarchical structure of the raw collected data is described in detail.

Each day's measurement set is named by the date the measurements were recorded. For example, "03.01.14" represents a set of measurement data that was collected on March 1st, 2014. Inside the date folder is a subfolder representing the environment setting for the measurements conducted. Three built-in options were "Indoors", "Brooklyn", and "Manhattan". In this project, measurements were performed in indoor and outdoor foliage environments in Brooklyn. The

office and foliage measurements are found under the “Indoors” and “Brooklyn” folders, respectively. Inside the environment folder is a subfolder titled with the name of the transmitter location used for those measurements. For indoor measurements, the name “MTC” represents MetroTech Center. For outdoor foliage measurements, the name “CMN” represents the MetroTech Commons Courtyard.

Inside the transmitter location folder is a subfolder with the name of the RX location used for measurements. There are generally multiple RX locations used for one day of measurements. For example, “RX1” represents the RX 1 receiver location corresponding to the “MTC1” TX location for indoor measurements. Inside the receiver location folder are measurement subfolders along with up to two other folders starting with “Folder Number”. The “Folder Number” folders are the calibration folders from the beginning of the day, end of the day, or both. Inside the calibration folders are a series of folders with names from “0 dB” to “70 dB”, representing the data obtained during the calibration routine for the specified RX attenuation setting. Inside the

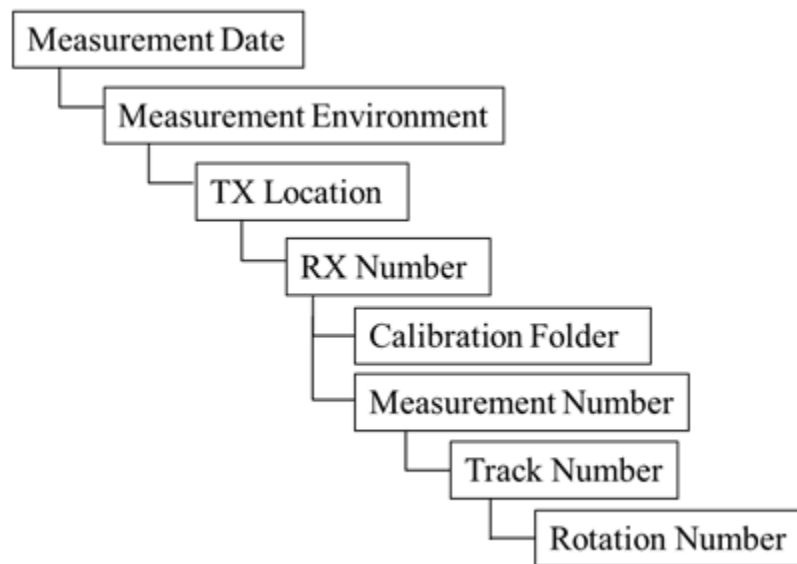


Fig. 4.4 Hierarchy structure of the raw measurement data collected during the campaign.

measurement folders is a track number folder which contains rotation number subfolders. Inside the rotation number subfolders is where the raw collected PDP measurement text files exist for each individual rotation or angular measurement recorded. Four such files exist in the rotation subfolder, one file for the in-phase data, one file for the quadrature data, one file for the  $I^2+Q^2$  PDP data, and a log file. An example of an  $I^2+Q^2$  file name is as follows:

`“IQsquared_MTC1_1_4.000000m_Tx(Az0.0)(EL0.0)_Rx(Az-0.0)(EL10.0)_1.txt”`

The folder subsets form a hierarchy structure of the raw data collected which help specify the measurement date, environment, transmitter location, RX location, measurement number, and rotation number. Fig. 4.4 shows a depiction of the raw data file structure hierarchy. For each data file, there are two columns of data that are comma-separated. The first column is the sample time in nanoseconds and the second column is the power level in dBm. It should be noted that each  $I^2+Q^2$  PDP file is an average of 20 consecutive and instantaneous PDPs in order to reduce noise and to account for any sudden variations in the channel during recording.

## Chapter 5 73 GHz Indoor Measurement Analysis

This Chapter presents newly generated results pertaining to the 73 GHz indoor measurements conducted in a typical office environment on the 9<sup>th</sup> floor of 2 MetroTech Center, using a 400 Mcps broadband sliding correlator channel sounder. In these measurements, the 20 dBi (15° HPBW) TX and RX antennas were set at 2.5 m and 1.5 m above ground level, respectively, to emulate typical office access points and devices. Multiple antenna pointing angle combinations and sweeps were measured as previously described in Chapter 3. The results from those measurements and configurations are presented in this Chapter. At each tested azimuth and elevation combination, a power delay profile was acquired to generate path loss models and spatial characteristics of the indoor channel. The results shown here include directional (unique pointing angle) and omnidirectional path loss models, propagation characteristics of the indoor channel such as the RMS delay spread as a function of the T-R separation distance, spatial (lobe) statistics, and a partition-dependent path loss model. Table 2.1 explains the number of TX-RX combinations used for V-V and V-H measurement results.

### 5.1 Path Loss Models for the 73 GHz Indoor Channel

Fig. 5.1 shows all 73 GHz indoor path loss values at the tested receiver locations while using 20 dBi gain TX and RX antennas. Each individual marker on the plot represents a unique pointing angle between the TX and RX antennas for both the azimuth and elevation planes, at

Table 5.1 Number of TX-RX location combination used for the V-V and V-H measurement results, and associated environment types whether LOS or NLOS.

<b>Antenna Polarization Configuration</b>	<b>LOS Environments</b>	<b>NLOS Environments</b>	<b>TX Site(s) used</b>
Vertical-to-Vertical	3	18	MTC1; MTC2
Vertical-to-Horizontal	3	6	MTC1

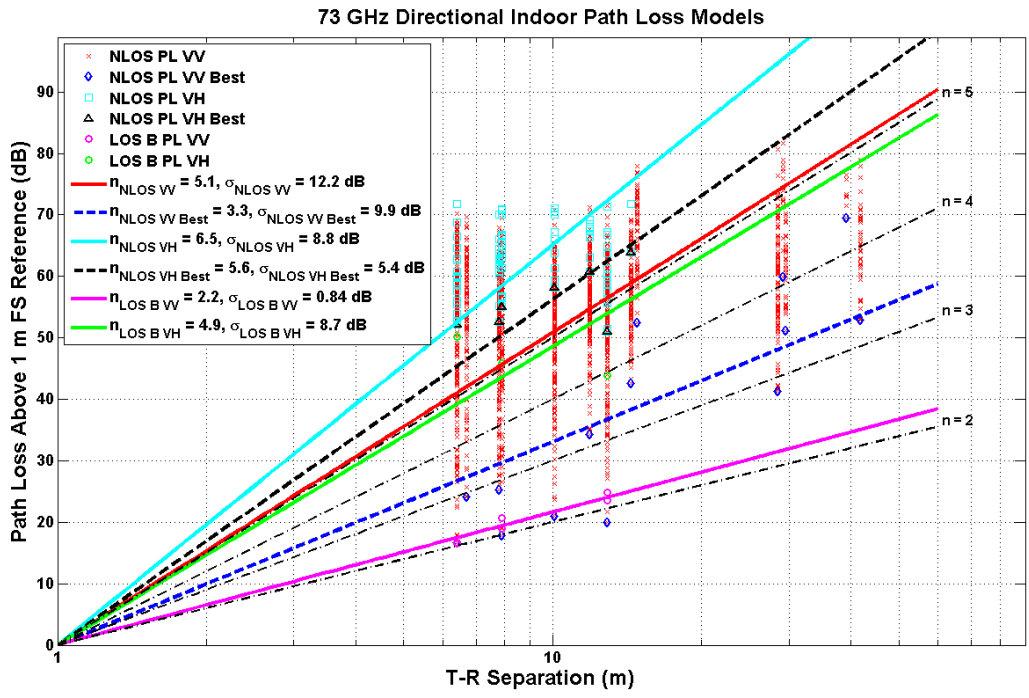


Fig. 5.1 73 GHz indoor single beam path losses with respect to a 1 meter free space reference distance as a function of T-R separation using 20 dBi (15° HPBW) gain antennas at both the TX and RX. NLOS path losses include LOS NB and truly NLOS measurements. Co-polarized and cross-polarized LOS measured path losses are also shown. The corresponding  $n = 2, 3, 4,$  and  $5$  path loss exponent path loss models with respect to a 1 meter reference distance are shown for comparison purposes.

Table 5.2 Measurement environment conventions for indoor measurements.

Setting	Description
LOS B	Environment where there are no obstructions between the TX and RX sites and the TX and RX antennas are pointed perfectly at each other on boresight in the azimuth and elevation planes.
LOS NB	Environment where there are no obstructions between the TX and RX sites but when the TX and RX antennas are <i>NOT</i> perfectly facing each other on boresight in the azimuth and elevation planes.
NLOS	Environment where there are obstructions between the TX and RX sites.

each T-R separation, and for NLOS and LOS environments. Since each measurement sweep consisted of rotating either the RX or TX antenna in 15° step increments in the azimuth plane, a maximum of 24 possible PDPs and subsequent path loss values could be recorded for each antenna sweep, with up to 264 measured channel impulse responses when considering all 11 sweep configurations for a given MTC1 RX location.

The path loss models displayed in Fig. 5.1 are for unique pointing angle combinations between the TX and RX. There were three conventions used for determining the scenario type of a unique pointing angle measurement. These conventions are: ‘LOS B’; ‘LOS NB’; and ‘NLOS’. Table 5.2 describes the different conventions for measurements. It is important to understand that for unique pointing angle path loss models as described here, ‘LOS NB’ measurements are grouped with ‘NLOS’ measurements to form the ‘NLOS’ models, whereas the ‘LOS B’ measurements are used to make up the ‘LOS’ path loss models. This is only holds for unique pointing angle models. The NLOS path loss exponent  $\bar{n}$  and shadowing factor  $\sigma$  for vertically polarized TX and RX antennas with respect to a 1 m free space reference distance were found to be 5.1 and 12.2 dB over all NLOS measurements. Again, ‘NLOS’ refers to LOS NB and NLOS measurements. When considering the strongest TX-RX link with the lowest path loss for each T-R separation distance, the best angle path loss exponent and shadowing factor were reduced to 3.3 and 9.9 dB, respectively, indicating the advantage of employing beamforming and beam combining techniques at the receiver to significantly improve link margin and SNR. It must be emphasized that beamforming and beam combining technologies using electrically-phased on chip antennas will combine received energy from multiple incoming directions to improve signal quality or to increase coverage distances, as demonstrated in [49] [50]. The same types of models were computed for the V-H antenna polarization configuration and the corresponding NLOS path loss exponent and shadowing factor with respect to a 1 m free space reference distance were found to be 6.5 and 8.8 dB, respectively when considering arbitrary pointing angles, and thus offering on average a cross polarization isolation of 14 dB/decade as compared to V-V. When considering the azimuth/elevation angle combinations at each T-R separation distance that provided the lowest path loss in the cross-polarized scenario, the path loss exponent and

shadowing factor with respect to a 1 m free space reference distance were reduced to 5.6 and 5.4 dB, respectively, thus providing on average a cross-polarization isolation of 23 dB/decade when considering the best angles as compared to the co-polarized antenna setting. In a perfect LOS environment with antennas perfectly on boresight for the co-polarized (V-V) configuration, the path loss exponent and shadowing factor were found to be 2.2 and 0.84 dB, respectively, and is very close to ideal theoretical free space propagation. The same boresight measurements were performed for the cross-polarized V-H antenna configuration, where the TX antenna remained vertically polarized and the RX antenna was horizontally polarized, resulting in a path loss exponent and shadowing factor of 4.9 and 8.7 dB in reference to a 1 meter free space distance, respectively. The cross-polarization isolation as compared to the co-polarized LOS scenario was found to be 27 dB / decade.

The path loss model results obtained for unique pointing angles in the indoor environment show that LOS free space propagation in indoor environments for the 73 GHz band is favorable and close to theoretical free space path, and even shows improvements with the help of ground bounces and constructive interference. While the NLOS path loss experienced is greater than 50 dB / decade, the use of multiple antenna elements can significantly decrease the path loss experienced when considering the best possible paths. Beamforming and beam combining technologies can be used to take advantage of such improvements. The cross polarization measurements also show the potential for antenna polarization diversity systems in indoor mmWave communications systems. Multipath in indoor environments may change polarization as the propagating wave reflects and encounters obstructions, and the use of polarization diversity can help to improve SNR and link margin in such environments.

In addition to the unique pointing angle path loss models, omnidirectional path loss models with respect to a 1 meter free space reference distance were also created. The models were created using methods similar to those used in [51]. Fig. 5.2 shows the omnidirectional path loss scatter plot for the 73 GHz indoors measurements that were synthesized from the unique pointing angle (directional) path loss data presented in Fig. 5.1. These models were created by summing the received power at all measured unique pointing azimuth and elevation angle combinations for each TX-RX location combination tested. Both TX and RX sweep measurements were used to recover the total omnidirectional received power, while taking caution not to double count duplicate angles measured. The corresponding path loss was obtained by removing the antenna gains, thereby simulating two 0 dBi isotropic omnidirectional TX and RX antennas. The measurement scenarios differ for the omnidirectional models as compared to the directional models such that LOS describes an environment where the TX and RX sites have an unobstructed view of one another, whereas a NLOS environment describes a situation where the TX and RX sites do not have a clear path between the two, due to obstructions. The omnidirectional LOS path loss exponent and shadowing factor for vertically polarized TX and RX antennas with respect to a 1 m free space reference distance were found to be 1.5 and 0.76 dB respectively. The corresponding omnidirectional LOS path loss exponent and shadowing factor for the cross-polarized antenna V-H scenario were 4.5 and 6.6 dB respectively. The co-polarized NLOS omnidirectional path loss exponent and shadowing factor were found to be 3.1 and 8.9 dB respectively, which are typical of current UHF/Microwave channels. Note that the omnidirectional path loss models in LOS and NLOS for the co-polarized scenario used only a sub-set of the acquired directional data. Indeed, many antenna pointing combinations were performed with RX elevation spacings of  $5^\circ$  which is not enough to assume independence

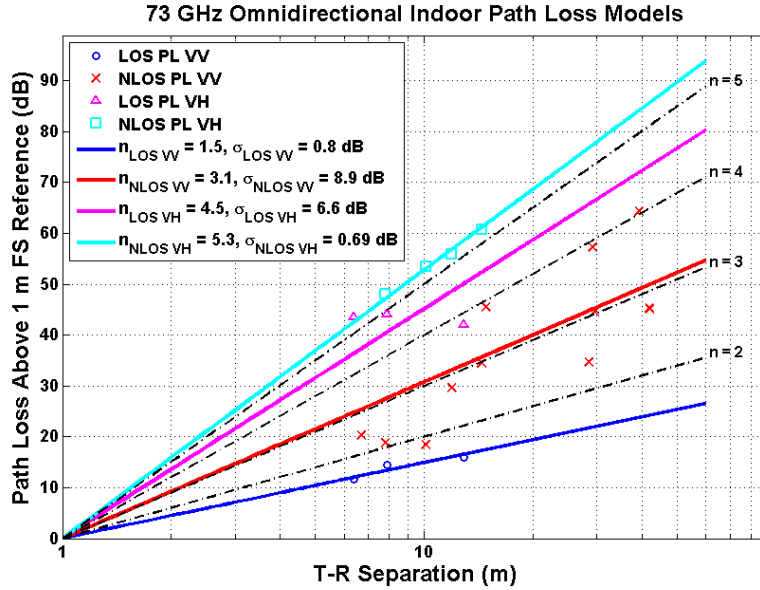


Fig. 5.2 73 GHz omnidirectional path loss models with respect to a 1 meter free space reference distance for a typical indoor office environment, synthesized from the 73 GHz directional measurements, using a pair of 20 dBi gain horn antennas with a 15° HPBW.

Table 5.3 Path loss exponents and shadowing factors with respect to a 1 m free space reference distance computed from the 73 GHz indoor office environment directional (unique pointing angle) measurements, computed for both co-polarized (V-V) and cross-polarized (V-H) scenarios.

Directional Parameters		TX-RX Polarization			
		V-V		V-H	
TX-ID	Environment Type	PLE	$\sigma$ (dB)	PLE	$\sigma$ (dB)
MTC1 & MTC2	LOS-B	2.2	0.84	4.9	8.7
	NLOS	5.1	12.2	6.5	8.8
	NLOS Best	3.3	9.9	5.6	5.4

Table 5.4 Path loss exponents and shadowing factors with respect to a 1 m free space reference distance synthesized using the 73 GHz indoor office environment directional measurements, computed for both co-polarized (V-V) and cross-polarized (V-H) scenarios.

Omnidirectional Parameters		TX-RX Polarization			
		V-V		V-H	
TX-ID	Environment Type	PLE	$\sigma$ (dB)	PLE	$\sigma$ (dB)
MTC1 & MTC2	LOS	1.5	0.76	4.5	6.6
	NLOS	3.1	8.9	5.3	0.69

between antenna sweeps, and so only the antenna pointing angle combinations with RX elevation spacings of 15° (exactly one HPBW) for both the TX and RX antennas were considered for

recovering omnidirectional models. Table 5.3 and Table 5.4 summarize the various directional and omnidirectional path loss exponents and shadowing factors measured for the 73 GHz indoor office environment for both co-polarized and cross-polarized antenna configurations. For directional path loss results, there is approximately 27 dB and 14 dB of isolation noticed between the co-polarized and cross-polarized antenna measurements respectively. This type of loss is expected due to the antenna polarization mismatch between the TX and RX antennas used. The shadowing factor for co-polarized path loss results is larger than the cross-polarized path loss results, and this can be attributed to fewer measurements obtained for the cross-polarized configuration where many signals were either close to or at the noise floor and therefore not recordable or not considered during post-processing. The indoor omnidirectional co-polarized path loss results are very promising for an indoor environment, as the LOS path loss value is greater than true free space, due to ground bounces and constructive interference from reflections. In addition, the NLOS PLE of 3.1 shows that the signal attenuates by only 31 dB / decade, and is reasonable for an indoor wireless network. The cross-polarization results are also promising as the PLE is similar to recent outdoor mmWave measurements conducted in New York City [52] [54], but fortunately for the indoor environment, the T-R separation distances are much shorter and the environment also includes more smooth surface reflectors.

## **5.2 Propagation Characteristics of the 73 GHz Indoor Channel**

Fig. 5.3 shows the RMS delay spread CDF for the 73 GHz directional measured data obtained for each unique pointing angle combination for both co-polarized (V-V) and cross-polarized (V-H) antenna configurations. The mean and standard deviation of the RMS delay spreads in the co-polarized scenario were measured to be 11.8 ns and 12.9 ns respectively, with the 50% and 90% probabilities occurring for RMS delay spreads of 7.3 ns and 31.5 ns,

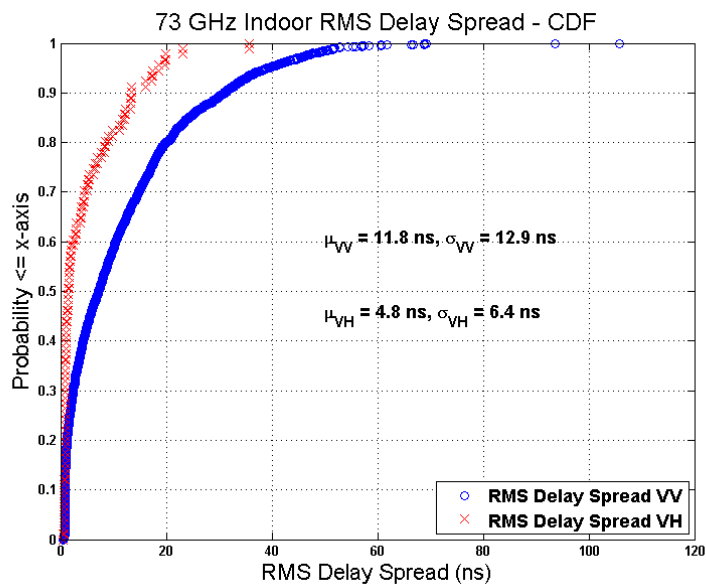


Fig. 5.3 Cumulative distribution function of the RMS delay spreads measured in the 73 GHz indoor channel for each unique pointing angle combination, using 20 dBi gain, 15° HPBW antennas.

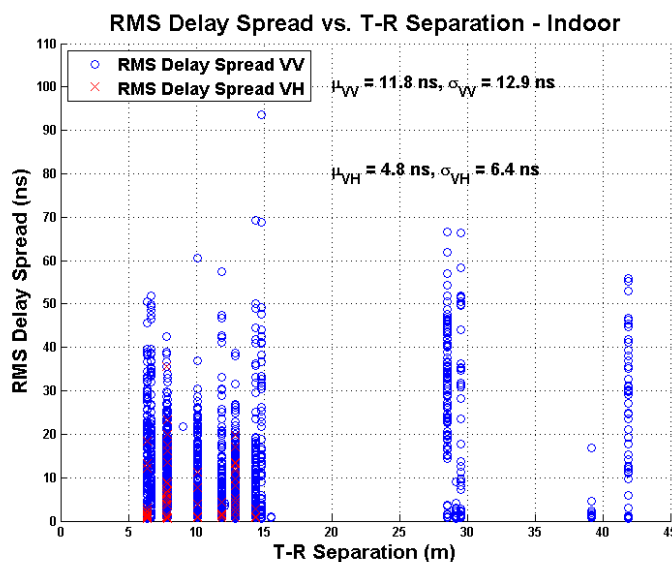


Fig. 5.4 The RMS delay spreads as a function of T-R separation distance obtained for the 73 GHz indoor channel using 20 dBi gain, 15° HPBW antennas. The RMS delay spread is independent of distance. 21 T-R separations distances were measured for V-V antenna polarizations and 9 T-R separation distances were measured for the V-H antenna polarizations.

respectively. 99% of all measured RMS delay spreads were below 52 ns. The maximum RMS delayed spread was measured to be 105.6 ns for V-V antenna polarization.

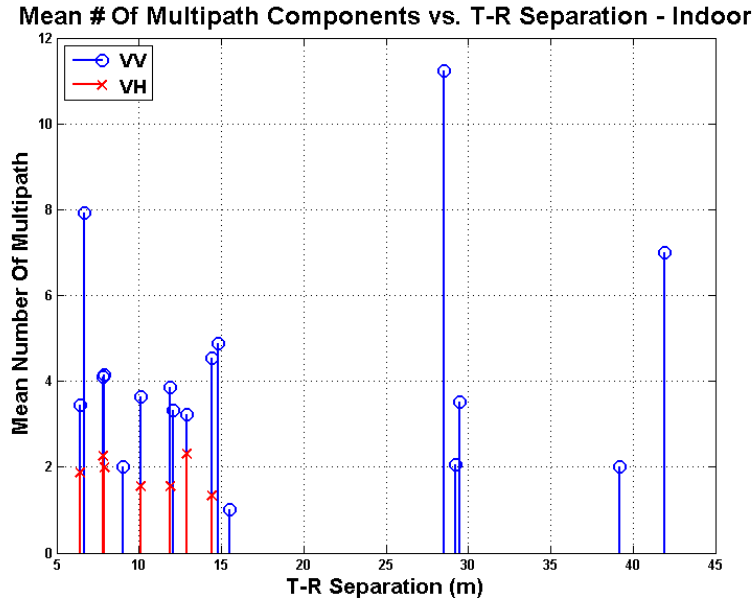


Fig. 5.5 The mean number of multipath components observed at any unique arbitrary pointing angle ( $15^\circ$ ) at the RX for different T-R separation distances measured for the 73 GHz indoor office environment measurements using 20 dBi gain,  $15^\circ$  HPBW antennas. 21 T-R separation distances were tested for V-V antenna polarizations and 9 T-R separation distances were measured for V-H antenna polarizations. The multipath components were detected using a peak detection algorithm.

In the cross-polarized scenario (V-H), the mean and standard deviation of the RMS delay spreads were measured to be 4.8 ns and 6.4 ns respectively, indicating that the cross-polarization discrimination mitigates the propagation of multipath components. In addition, the maximum RMS delay spread for V-H antenna polarization was 35.7 ns. Fig. 5.5 and Table 5.5 show and summarize the mean number of multipath components observed at unique pointing angles in  $15^\circ$  windows at the RX for the co- and cross-polarized antenna configurations, conditioned upon the existence of received power. The number of multipath components was determined by implementing a peak detection algorithm that is able to pick up the multipath peak values. Both LOS and NLOS measurements scenarios were combined to determine the multipath number statistics. The mean and standard deviation of the number of multipath components for an arbitrary pointing angle combination over all 21 RX locations measured for the co-polarized antenna configuration was 4.2 and 2.5, respectively. The mean and standard deviation of the

Table 5.5 Summary of the mean number of multipath components observed at any unique arbitrary pointing angle ( $15^\circ$ ) at the RX for different T-R separation distances measured for the 73 GHz indoor office environment measurements, using 20 dBi gain,  $15^\circ$  HPBW antennas. 21 T-R separation distances were tested for V-V antenna polarizations and 9 T-R separation distances were measured for V-H antenna polarizations. The multipath components were detected using a peak detection algorithm.

Location	Environment Type	T-R Separation (m)	Mean Number of Multipath Components	
			VV	VH
Office Indoor	LOS	6.4	3.4	1.9
	NLOS	7.8	4.1	2.3
	NLOS	10.1	3.6	1.6
	LOS	7.9	4.1	2.0
	NLOS	11.9	3.9	1.6
	NLOS	14.4	4.5	1.3
	LOS	12.9	3.2	2.3
	NLOS	29.5	3.5	-
	NLOS	9.0	2.0	-
	NLOS	28.5	11.2	-
	NLOS	29.2	2.1	-
	NLOS	39.2	2.0	-
	NLOS	41.9	7.0	-
	NLOS	12.1	3.3	-
	NLOS	15.5	1.0	-
	NLOS	6.7	7.9	-
	NLOS	14.8	4.9	-

number of multipath components for an arbitrary pointing angle combination over all 9 RX locations measured for the cross-polarized antenna configuration was 1.8 and 0.4, respectively. The results indicate that many multipath components can reach the receiver in small directional windows in an office environment for 73 GHz millimeter-wave propagation. The results also show the reflective nature of the indoor environment and the need for equalization algorithms at the receiver to increase the received signal strength and to mitigate inter-symbol interference.

PDPs with typical and maximum RMS delay spreads for different indoor environments with vertical-to-vertical antenna polarization are shown in Fig. 5.6. The PDP in Fig. 5.6 (a) was recorded at RX1 for MTC1 for a LOS\_B environment. When the TX and RX antennas were perfectly pointed towards each other with a 6.4 meter T-R separation distance, only the dominant LOS component is apparent. Fig. 5.6 (b) shows the PDP acquired for the same TX-RX combination as that in Fig. 5.6 (a), but with the RX antenna  $60^\circ$  off the boresight angle in the azimuth plane. There were six multipath components, the first and also strongest was the LOS component, and the other components came from the reflections of the walls and office partitions in the surrounding areas. Fig. 5.6 (d) shows the PDP obtained in a NLOS environment (MTC1 and RX6) with a wall and two office partitions between the direct path of the TX and RX. The first arriving peak penetrated and was attenuated by the wall and office partitions. The strongest peak came from multiple reflections off the wall behind the transmitter and receiver. Fig. 5.6 (c) shows the largest observed RMS delay spread obtained in the co-polarization indoor measurements, at RX1 for MTC1 with 6.4 meters T-R separation distance, the same location as that in (a) and (b). Since the pointing directions of TX and RX antenna were perpendicular to each other, the received power of the first arriving peak was relatively lower with other multipath components arising from multiple reflections off the walls and office partitions. The presence of obstructions in the environment (walls, doors, office partitions etc.), act as reflective surfaces for the indoor millimeter wave channel. For the largest RMS delay of 105.6 ns, the maximum traveling distance of the multipath is about 300 meters. Considering the closed indoor environment, this multipath more than likely reflected multiple times before reaching the receiver.

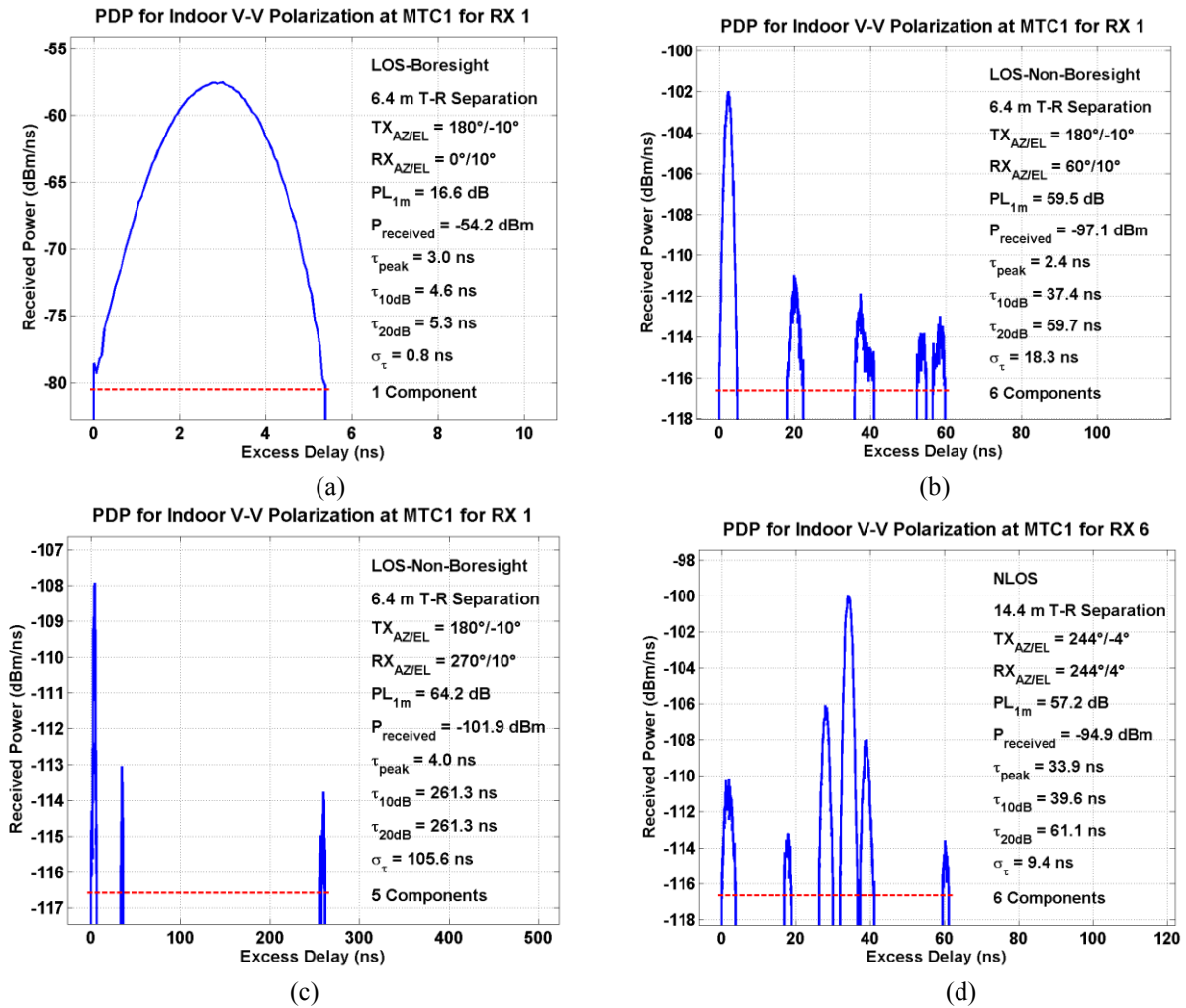


Fig. 5.6 (a), (b) and (d) show typical power delay profiles (PDP) measured in the indoor environment with vertical-to-vertical polarization. (c) shows the PDP with maximum RMS delay spread. The horizontal red line on each PDP represents the computed noise threshold level. Because of the absence of GPS synchronization between the TX and RX, the excess delay is relative to the first arriving multipath above the threshold level. The received power is in dBm / nanosecond. Each PDP corresponds to a recording for a specific TX-RX antenna angle combination in the azimuth and elevation planes. The measurement information including environmental type, T-R separation distance, TX and RX azimuth and elevation, path loss with respect to 1 meter, received power, maximum peak delay, excess delay 10 dB and 20 dB down from the maximum peak, RMS delay spread, and number of multipath components are shown on the right of each PDP.

PDPs with typical and maximum RMS delay spreads for different indoor environments with vertical-to-horizontal antenna polarization are shown in Fig. 5.7. The PDP in Fig. 5.7 (a) was recorded at RX1 for MTC1 for a LOS\_B environment with 6.4 meter T-R separation distance. When the TX and RX antenna were perfectly pointed towards each other, the first and strongest

arriving component was the LOS component. By comparing Fig. 5.7 (a) with Fig. 5.6 (a), the received power for cross-polarization was 30 dB lower than the received power for co-polarization. The other four multipath components resulted from reflections off of the walls behind the TX and RX, respectively. Fig. 5.7 (b) shows the PDP acquired at the same TX and RX location as in (a), but with the RX antenna 50° off of the boresight angle in the azimuth plane. There was only one component, the LOS component captured by the RX antenna at an off-boresight angle. Fig. 5.7 (c) shows the PDP obtained in a NLOS environment (MTC1 and RX2) with an office partition (cubicle) between the LOS path of the TX and RX. The first arriving peak penetrated and was attenuated by the cubicle. The second multipath component, which was close to the first peak, resulted from a reflection off of the wall in front of the TX and RX. The traveling distance was within 20 meters with respect to the first arriving peak. Fig. 5.7 (d) shows the largest observed RMS delay spread in the cross-polarization indoor measurements, at RX1 for MTC1 with a 6.4 meter T-R separation distance, at the same location as in (c). The first arriving peak resulted from a reflection off the nearby wall and the last arriving peak that was 1 dB lower, resulted from multiple reflections, traveling a distance of about 100 meters before reaching the receiver.

### **5.3 73 GHz LOS and NLOS Spatial (Lobe) Statistics**

The 73 GHz mmWave indoor channel was found to be a very directional channel whereby energy departs and arrives in very narrow directions, as a result of using highly directional

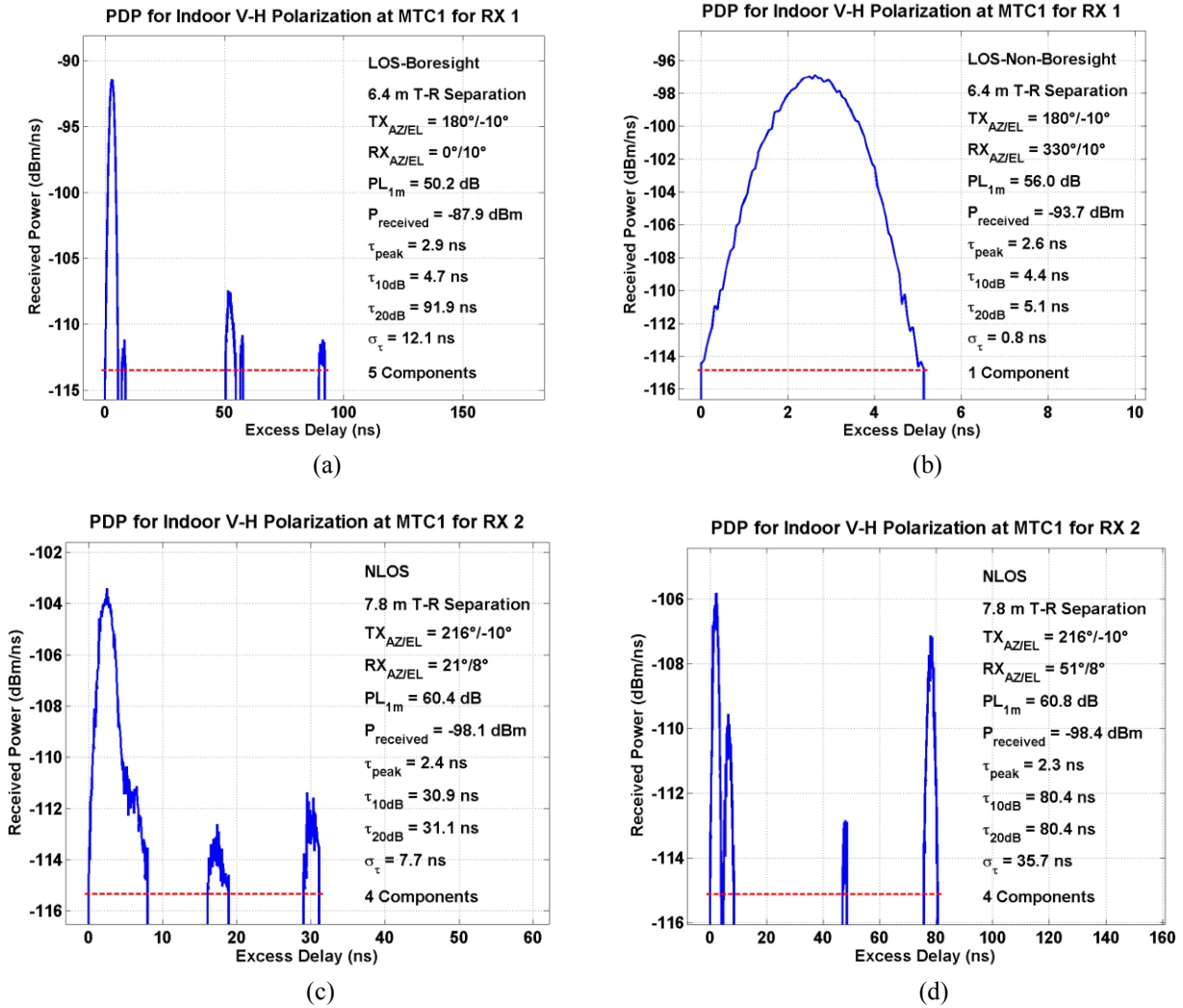


Fig. 5.7 (a), (b) and (c) show typical power delay profiles (PDP) measured in the indoor environment with vertical-to-horizontal polarization. (d) shows the PDP with maximum RMS delay spread. The horizontal red line on each PDP represents the computed noise threshold level. Because of the absence of GPS synchronization between the TX and RX, the excess delay is relative to the first arriving multipath above the threshold level. The received power is in dBm / nanosecond. Each PDP corresponds to a recording for a specific TX-RX antenna angle combination in the azimuth and elevation planes. The measurement information including environmental type, T-R separation distance, TX and RX azimuth and elevation, path loss with respect to 1 meter, received power, maximum peak delay, excess delay 10 dB and 20 dB down from the maximum peak, RMS delay spread, and number of multipath components are shown on the right of each PDP.

narrowbeam antennas. The spatial characteristics of the indoor channel are easily understood by analyzing lobe statistics, as described in [6] and [54], providing a simple framework to characterize indoor spatial directionality. In addition to spatial statistics, temporal cluster statistics also offer an important aspect that help understand the wideband characteristics of the indoor channel. However, the lack of TX-RX synchronization did not allow us to recover omnidirectional power delay profiles, and so ray-tracing techniques must be used to synthesize absolute timing, that will then allow us to analyze and extract temporal statistics to build a statistical simulator that can recreate the indoor measured channels, as performed in [6] for the 28 GHz outdoor wideband dense urban channel. The diagram below from [6] illustrates both temporal and spatial parameters. A time cluster is defined as a group of cluster sub-paths (i.e., multipath components) traveling close in time and space. A time cluster is identified by nine

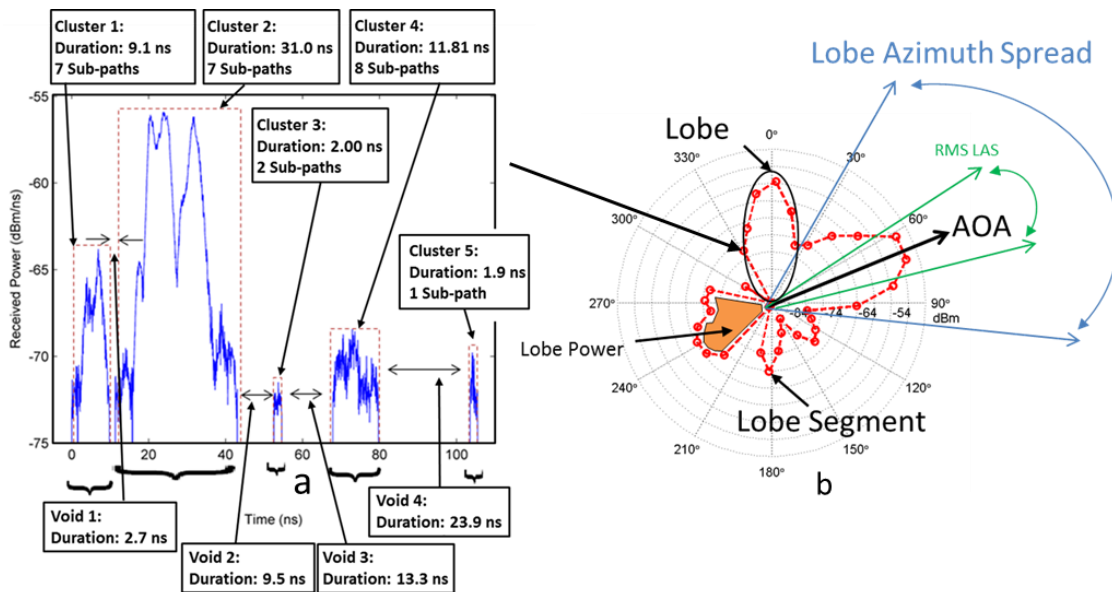


Fig. 5.8 (LEFT): Diagram showing typical power delay profile measured in Manhattan at 28 GHz with energy arriving from a particular AOA, obtained directional 24.5 dBi gain antennas (10.9° HPBW), where cluster terminology is illustrated. Four time clusters may be seen with time durations ranging from 2 ns to 31 ns. (RIGHT): Diagram showing a polar plot measured in Manhattan at 28 GHz, where lobe terminology is illustrated. Five distinct lobes may be seen with various lobe azimuth spreads and AOAs. Each 'dot' is a lobe angular segment, and represents the total integrated received power over a 10° angle [6].

principal cluster parameters: the absolute time of arrival at the receiver, the azimuth/elevation angles of departure, the azimuth/elevation spreads of departure, the azimuth/elevation angles of arrival, and the azimuth/elevation spreads of arrival [6]. A spatial lobe is defined as a departing or incoming direction of contiguous energy over the azimuth and/or elevation planes. A spatial lobe is identified by eight principal lobe parameters: the azimuth/elevation angles of departure, the azimuth/elevation spreads at the transmitter, the azimuth/elevation angles of arrival, and the azimuth/elevation spreads at the receiver [6].

Fig. 5.8 shows sample measurements obtained from a 28 GHz wideband outdoor measurement campaign in New York City, and are meant to illustrate the terminology. In the polar plot in Fig. 5.9, we can identify 4 distinct lobes, and each lobe has well defined characteristics, such as its lobe azimuth spread, its RMS lobe azimuth spread, and its mean angle of departure or arrival [6].

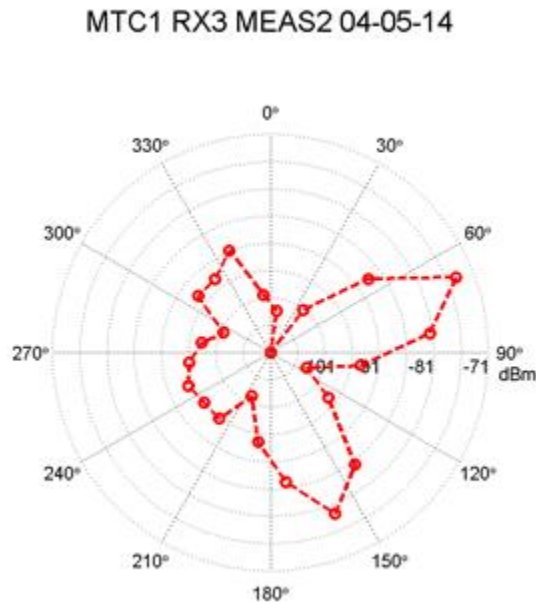


Fig. 5.9 Typical polar plot measured at 73 GHz at a RX in a NLOS indoor environment using a pair of 20 dBi (15° beamwidth) gain antennas at the. Multiple lobes can be observed where energy arrives in very tight directions over a wide angular spread. This polar plot was obtained from an RX sweep at receiver RX 3 for the MTC 1 transmitter.

The parameters defined for a lobe are described below:

1. The number of lobes in a polar plot:

The number of lobes in a polar plot corresponds to the number of outgoing or incoming energy directions at the transmitter or receiver, respectively.

2. The azimuth spread of a lobe.

The azimuth spread of a lobe is defined as the azimuth angle span over which the lobe exists, and is obtained from the following equation:

$$\Delta\theta = |\theta_K - \theta_1| + \Theta_{3\text{dB}} \quad (5.1)$$

where  $\theta_1$  and  $\theta_K$  are the first and last azimuth angles composing the lobe, and  $\Theta_{3\text{dB}} = 15^\circ$  for the TX and RX antennas used during indoor measurements.

3. The angle of departure/angle of arrival of a lobe

The AOD/AOA of a lobe is defined as the power weighted mean angle of the lobe power azimuth spectrum, as is shown below:

$$\bar{\theta} = \frac{\sum \theta_k P(\theta_k)}{\sum P(\theta_k)} \quad (5.2)$$

where  $P(\theta_k)$  is the total received power (i.e., area underneath measured PDP) in linear units at azimuth angle  $\theta_k$ . The sub-index  $k$  runs through all angles belonging to the same lobe.

4. The RMS azimuth spread of a lobe

The lobe azimuth RMS spread  $\sigma_\theta$  is the second moment of the lobe power azimuth spectrum, and is computed as follows:

$$\sigma_\theta = \sqrt{\bar{\theta}^2 - \bar{\theta}^2} \quad (5.3)$$

where

$$\bar{\theta} = \frac{\sum \theta_i P(\theta_i)}{\sum P(\theta_i)} \quad (5.4)$$

$$\overline{\theta^2} = \frac{\sum \theta_i^2 P(\theta_i)}{\sum P(\theta_i)} \quad (5.5)$$

where  $P(\theta_i)$  is the total integrated received power (in linear units) at azimuth angle  $\theta_i$ , and the sub-index  $i$  runs over all angles belonging to a lobe. The lobe azimuth RMS spread indicates the azimuth range over which most of the power is contained in the lobe. This quantity will be important for future electrically steered phased antenna arrays, in which on-chip antennas will be able to steer their antenna pattern towards the strongest directions of arrival to improve received signal levels. It is important to estimate the azimuth range over which to spread the antenna pattern in order to match the antenna to the incoming energy spread at the receiver.

In this work, polar plots for indoor RX locations were thresholded using a 10 dB and 15 dB down from the maximum received power threshold for LOS and NLOS spectra, respectively. The following tables summarize the statistics of the spatial channels for AOD and AOA power azimuth spectra in both LOS and NLOS environment.

For co-polarized antennas, 3 LOS and 18 NLOS TX-RX combinations were measured. In a LOS environment, the mean and standard deviation of the number of AOD lobes were measured to be 1.2 and 0.4 respectively, and for AOA lobes, the respective values were found to be 2 and 1.2. In the NLOS environment, the mean and standard deviation of the number of AOD lobes were 1.9 and 0.7 respectively, and for AOA lobes, the respective values were found to be 2.4 and 1.2. Fig. 5.10 shows the histogram of the number of AOA lobes measured in NLOS environments. The mean AOAs in the NLOS co-polarized scenario were found to be uniformly distributed between  $0^\circ$  and  $360^\circ$ , as shown in Fig. 5.11. The mean AODs in LOS and NLOS, as well as AOAs in LOS environment may assumed to be also uniformly distributed between  $0^\circ$  and

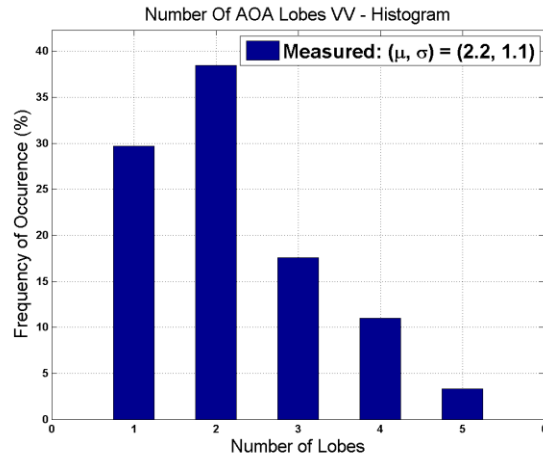


Fig. 5.10 Histogram of the number of AOA lobes measured in a NLOS office indoor environment for the co-polarized scenario (V-V). The mean and standard deviation for the number of AOA lobes were 2.2 and 1.1, respectively. The number of AOA lobes in a NLOS environment was determined by thresholding the AOA NLOS polar plots using a 15 dB down from maximum peak threshold. 18 TX-RX combinations were measured for these results.

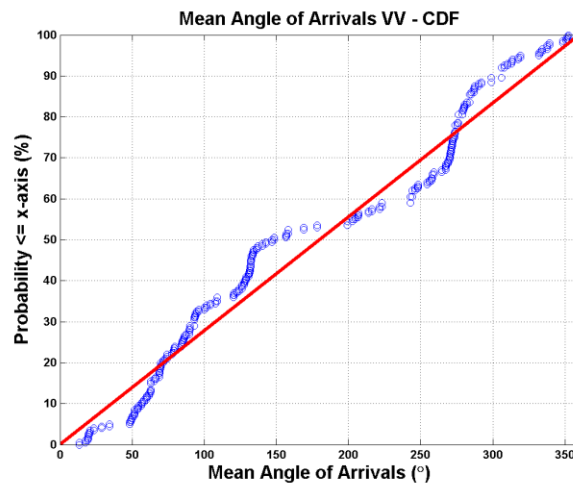


Fig. 5.11 The cumulative distribution function of the mean AOAs in a NLOS environment for the co-polarized scenario. The measured data points are blue circles, and the red line is the cumulative distribution function of a uniformly distributed random variable between 0° and 360°. 18 TX-RX combinations were measured for these results.

360°, however due to the small number of data points, this trend was not readily observable (see Table 5.6, Table 5.7, and Table 5.8 for the number of measurement points collected).

For the co-polarization antenna configurations, the mean and standard deviation of the AOD lobe azimuth spreads (LAS) in LOS environments were measured to be  $27.5^\circ$  and  $11.3^\circ$  respectively, and for AOA LAS, they were found to be  $20.4^\circ$  and  $7.3^\circ$ . For NLOS, the AOD LAS mean and standard deviation were  $51.5^\circ$  and  $27.5^\circ$  respectively, and the AOA LAS mean and standard deviation were measured as  $35.2^\circ$  and  $19.7^\circ$  in the co-polarized scenario, indicating that the 20 dBi TX antenna can cover a relatively large section of the azimuth plane, and the RX antenna can receive energy from a relatively large section of the azimuth plane in NLOS environments.

The RMS lobe azimuth spreads indicate the angular span over which most of the energy is received (analogous to the RMS delay spread in the time domain). For the co-polarization antenna configurations, in LOS environments the RMS lobe azimuth spread was measured to be  $3.7^\circ$  and  $2.1^\circ$  for AODs and AOAs respectively in the co-polarized scenario, indicating that energy arrives in very narrow directions. However, in NLOS environments, the RMS lobe azimuth spreads were measured to be between  $8.8^\circ$  and  $6.3^\circ$ , indicating that energy departs and arrives in wider angular spreads than in LOS environments.

Table 5.6 and Table 5.7 summarize the spatial statistics for both AOD and AOA statistics in LOS and NLOS environments for the co-polarized scenario (V-V). The mean and standard deviation of the AOA lobe azimuth spreads (LAS) in LOS were measured to be  $27^\circ$  and  $28.1^\circ$  respectively for the cross-polarized scenario (V-H). In NLOS, the AOA LAS mean and standard deviation were  $30.9^\circ$  and  $24.6^\circ$  respectively, in the cross-polarized scenario.

For LOS and NLOS environments, the RMS lobe azimuth spread was measured to be  $4.5^\circ$  for AOAs in the cross-polarized scenario. Table 5.8 summarizes the spatial statistics for AOAs in LOS and NLOS environments for the cross-polarized scenario (V-H). Note that cross-

Table 5.6 Mean and standard deviation of spatial AOD (lobe) parameters in a LOS and NLOS office environment for the co-polarized scenario (V-V). There were 3 LOS and 18 NLOS environments measured to produce these statistics.

AOD: V-V	Number of Data Points (LOS/NLOS)	LOS		NLOS	
		$\mu$	$\sigma$	$\mu$	$\sigma$
Number Of Lobes	5/16	1.2	0.4	1.9	0.7
$\theta_{AOD}$	6/30	Uniform(0,360)		Uniform(0,360)	
Lobe Azimuth Spread ( $^{\circ}$ )		27.5	11.3	51.5	27.5
RMS Lobe Azimuth Spread ( $^{\circ}$ )		3.7	3.1	8.8	5.5

Table 5.7 Mean and standard deviation of spatial AOA (lobe) parameters in a LOS and NLOS office environment for the co-polarized scenario (V-V). There were 3 LOS and 18 NLOS environments measured to produce these statistics.

AOA: V-V	Number of Data Points (LOS/NLOS)	LOS		NLOS	
		$\mu$	$\sigma$	$\mu$	$\sigma$
Number Of Lobes	26/91	1.4	0.5	2.2	1.1
$\theta_{AOA}$	36/200	Uniform(0,360)		Uniform(0,360)	
Lobe Azimuth Spread ( $^{\circ}$ )		20.4	7.3	35.2	19.7
RMS Lobe Azimuth Spread ( $^{\circ}$ )		2.1	3	6.3	5.3

Table 5.8 Mean and standard deviation of spatial AOA (lobe) parameters in a LOS and NLOS office environment for the cross-polarized scenario (VH). There were 3 LOS and 9 NLOS environments measured to produce these statistics.

AOA: V-H	Number of Data Points (LOS/NLOS)	LOS		NLOS	
		$\mu$	$\sigma$	$\mu$	$\sigma$
Number Of Lobes	3/4	3.3	2.3	4.3	1.7
$\theta_{AOA}$	10/17	Uniform(0,360)		Uniform(0,360)	
Lobe Azimuth Spread ( $^{\circ}$ )		27	28.1	30.9	24.6
RMS Lobe Azimuth Spread ( $^{\circ}$ )		4.5	9.4	4.5	5.6

polarization measurements for TX sweeps were not performed, and so statistics for AODs in LOS and NLOS environments are not available at this time for that antenna polarization configuration. Overall, the mean number of AOA lobes is larger for the V-H cross-polarization antenna configuration for both LOS and NLOS environments. This shows that the propagating wave for 73 GHz may change polarization many times as it hits reflectors before it reaches the

receiver. These statistics will be helpful in determining how to design polarization diversity systems for indoor mmWave communication systems. Although it should be noted that the comparison may be skewed due to the fact that closer T-R separation distances were measured for V-H polarizations, and less TX-RX combinations overall were measured.

## **5.4 73 GHz Indoor Office Environment Partition-Dependent Path Loss Model**

### **5.4.1 Partition-Dependent Directional Antenna Model**

In the indoor measurement analysis, the path loss exponent is useful for predicting large-scale propagation effects. However, the path loss exponent model is inadequate at predicting site-specific propagation effects, such as reflection, diffraction, or penetration losses caused by particular building construction materials [55]. A more refined model is a partition-based model in [9] that assumes free-space propagation in addition to extra attenuation due to the number and type of objects encountered by a single ray drawn between the transmitter and receiver [14].

Table 5.9 shows the T-R separation distance, free space path loss, observed path loss, and the numbers and types of partitions in some of the NLOS RX locations for MTC1 and MTC2 (not including the outage locations). Since the partition-based channel model works well for short T-R separation distances with a small number of multipath scatterers in the environment, only five RX locations from the indoor measurements were chosen to create a partition-based model. By looking at the building floor plan, partitions that existed between each transmitter and receiver link have two categories, soft partition and a wall. Soft partitions include common office furniture such as cubicles, cabinets, closets, etc. The walls are made of common indoor plasterboard and concrete partitions that have a thickness of 6 inches. Tracking a single point-to-point ray between the transmitter and receiver determines the number and types of partitions.

Table 5.9 The parameters for the partition-dependent directional antenna model including the T-R separation distance, free space path loss, observed path loss, partition loss, and the partition type and number, for co-polarized antennas.

TX ID	RX ID	T-R Separation (m)	Path Loss w.r.t 1 m (dB)	Partition Loss (dB)	Partition Type and Number	
					Soft Partition	Wall
MTC1	2	7.8	30.50	12.66	1	0
MTC1	3	10.1	35.10	15.01	1	0
MTC1	5	11.9	43.89	22.38	0	1
MTC1	6	14.4	54.37	31.21	1	1
MTC2	21	6.7	25.60	9.08	0	1

The path loss values for unique pointing angles in the table are obtained from the rotation 0 setting in the boresight-to-boresight sweeps, meaning that the TX and RX antennas are directly pointed towards each other. Based on the data collected in the indoor measurements, a partition-dependent path loss model can be generated by solving simultaneous equations with a least squares approach [56]. The partition dependent propagation attenuation model can be expressed as:

$$P_R = P_T + G_T + G_R + PL_{fs} - \sum_{i=1}^N a_i X_i \quad (5.6)$$

where  $P_R$  denotes the received power (dBm);  $P_T$  is the transmit power (dBm) before the TX antenna;  $G_T$  and  $G_R$  are the gains of the TX and RX antennas in dB, respectively;  $PL_{fs}$  (dB) is the free space path loss at distance  $d$ ; and  $a_i$  in the last term represents the quantities of the  $i^{\text{th}}$  obstructions material that are in the direct path of the TX And RX, and  $X_i$  corresponds to the attenuation values caused by the  $i^{\text{th}}$  obstruction material [57].

The path loss with respect to 1 meter at each RX locations can be written as a vector  $\overline{PL}$ , the T-R separation distances for the five RX locations can be written as a vector  $\overline{d}$ , the number of partitions at each RX locations can be written as a matrix  $A$ , each row of which shows the number of different partitions in the path between the TX and RX. The loss for each partition can

be written as a vector  $\bar{x}$ . The relationship of the above four vectors and matrix can be expressed using the following equations to solve for  $\bar{x}$ :

$$A\bar{x} = \overline{PL} - 20 \log_{10}(\bar{d}) \quad (5.7)$$

$$\bar{x} = \begin{bmatrix} X_a \\ X_b \\ \vdots \\ X_i \end{bmatrix}, \quad A = \begin{bmatrix} a_{11} & a_{12} & \cdots \\ a_{21} & a_{22} & \cdots \\ \vdots & \vdots & \ddots \\ a_{i1} & a_{i2} & \cdots \end{bmatrix}, \quad \bar{d} = \begin{bmatrix} d_1 \\ d_2 \\ \vdots \\ d_N \end{bmatrix}, \quad \overline{PL} = \begin{bmatrix} PL_1 \\ PL_2 \\ \vdots \\ PL_N \end{bmatrix} \quad (5.8)$$

The mean squared errors (or variance) of measured and predicted attenuation values for each location are calculated by:

$$\sigma^2 = \frac{1}{N} |A\bar{x} + 20 \log_{10}(\bar{d}) - \overline{PL}|^2 \quad (5.9)$$

The covariance matrix  $Q$  for each location is calculated by:

$$Q = \begin{bmatrix} \sigma_1^2 & & & \\ & \sigma_1^2 & & \\ & & \ddots & \\ & & & \sigma_i^2 \end{bmatrix} \quad (5.10)$$

The covariance matrix  $Q_b$  associated with each material is obtained by:

$$Q_b = A^T Q A \quad (5.11)$$

The standard deviation of each material can be calculated as:

$$\sigma_{b1}^2 = Q_b(1,1) \quad (5.12)$$

$$\sigma_{b2}^2 = Q_b(2,2) \quad (5.13)$$

Table 5.10 shows the attenuation values calculated for the partition-dependent model for unique pointing angles using the equations described above. The attenuation caused by soft partition, which is a common office material for office cubicles, is about 14 dB. The general wall

including plasterboard walls and concrete walls in indoor environments shows an attenuation loss of 16 dB per wall.

### 5.4.2 Partition-Dependent Omnidirectional Model

Table 5.11 shows the T-R separation distance, free space path loss, observed path loss, and

Table 5.10 Partition attenuation values for the 73 GHz indoor channel measurements for common office building partitions, using co-polarized antennas, obtained from the directional partition-dependent model.

Partition Type	Thickness (cm)	Attenuation Values $\bar{X}_i$ (dB)	Standard Deviation (dB)
Office Partition	3	14.25	1.78
General Wall	15	16.14	3.75

Table 5.11 The parameters for the omnidirectional antenna partition-dependent model including the T-R separation distance, free space path loss, actual path loss and the partition type and number, for co-polarized antennas.

TX ID	RX ID	T-R Separation (m)	Omni-Path Loss w.r.t 1 m (dB)	Partition Loss (dB)	Partition Type and Number	
					Soft Partition	Wall
MTC1	2	7.8	18.75	0.91	1	0
MTC1	3	10.1	18.42	-1.66	1	0
MTC1	5	11.9	29.72	8.21	0	1
MTC1	6	14.4	34.42	11.2	1	1
MTC2	21	6.7	20.31	3.79	0	1

Table 5.12 Partition attenuation values for 73 GHz indoor measurements for common office building partitions, for co-polarized antennas using the omnidirectional partition-dependent model.

Partition Type	Thickness (cm)	Attenuation Values $\bar{X}_i$ (dB)	Standard Deviation (dB)
Office Partition	3	1.03	2.37
General Wall	15	7.40	2.69

the numbers and types of partitions for the NLOS RX location for MTC1 and MTC2 for the omnidirectional model (the same locations as the unique pointing angle model). The path loss values for the omnidirectional model in the table are calculated by summing the received power from all measurement rotations for all the TX and RX combinations while removing the effects of antenna gain. The omnidirectional model includes reflections from the wall and soft partition, so as expected, the received power is higher than the received power from point-to-point measurements. For some less heavily obstructed locations, considering the reflections of surrounding scatterers for non-point-to-point directions, the omnidirectional path loss may be lower than the free space path loss, resulting in negative partition loss values as seen in Table 5.11. This is attributed to the overlap of some angular measurements during sweeps that results in a more than optimistic path loss result. Based on the data collected in the indoor measurements, a partition-dependent path loss model using the omnidirectional model was generated by solving simultaneous equations with a least squares approach [56].

Table 5.12 shows the attenuation values computed for the omnidirectional path loss model using the same equations used for the unique pointing angle model. The attenuation caused by soft partitions is about 1 dB with a standard deviation of 2.3 dB. Since the omnidirectional model includes reflections from the wall and soft partitions as well as some overlapping angular energy, the received power may be higher than the received power from point-to-point measurements. The attenuation values for each construction material are lower than the attenuation values obtained from unique pointing angles. The general wall shows an attenuation of 7.4 dB per object with a standard deviation of 2.7 dB.

The partition-based model can be generated easily because the prediction is usually obtained from simple closed form expressions. However, only propagation losses without great site-

specific accuracy can be predicted. If a significant amount of the received power comes from multipath, then the partition-based model loses its physical significance [55].

## **Chapter 6 Measurement Analysis of the 73 GHz Outdoor Free Space and Foliage Environment**

This section presents the results obtained from the 73 GHz outdoor free space and foliage measurements using 27 dBi gain ( $7^\circ$  HPBW) directional horn antennas for both co-polarized and cross-polarized scenarios at the MetroTech Center on the NYU Engineering campus. The results shown here include directional (unique pointing angle) and omnidirectional path loss models, as well as propagation characteristics of the free space and foliage environments such as RMS delay spreads as a function of T-R separation distance, a foliage attenuation model, and ground bounce reflection coefficients.

### **6.1 73 GHz Outdoor Free Space Channel**

The measurement details for the 73 GHz outdoor free space measurements were fully explained in Section 3.2.2. The purpose of these measurements was to validate theoretical free space propagation in the 73 GHz frequency band, and to create directional and omnidirectional models from the measurements. The measurements were performed on the MetroTech Commons Courtyard in Downtown Brooklyn as detailed in Fig. 3.19, where PDPs were recorded at the RX for multiple TX and RX antenna sweeps for various pointing angle combinations. The RX antenna was always at a height 2 meters relative to the ground and the TX antenna was set to a height of 4.06 meters relative to the ground in order simulate a lamppost level access point to emulate future base stations in the mmWave regime. Four RX locations were measured, with T-R separation distances of 10 m, 20 m, 30 m, and 40 m, where each subsequent RX location was 10 m further from the previous as detailed in Fig. 3.19. At each RX location, the TX and RX antennas were initially aligned perfectly on boresight in the azimuth and elevation planes, and

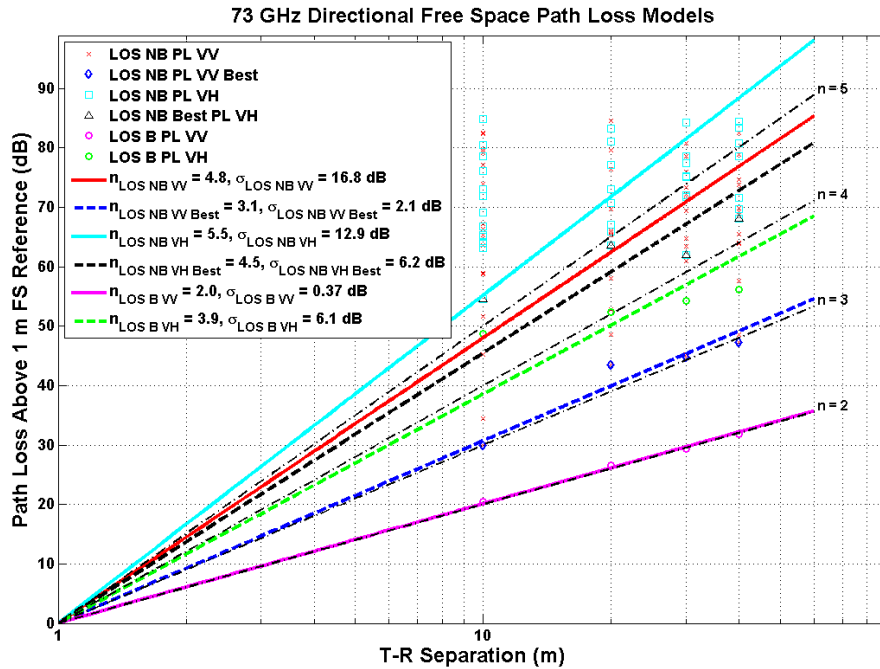


Fig. 6.1 73 GHz outdoor single beam path losses as a function of T-R separation relative to a 1 m free space reference distance, using 27 dBi (7° HPBW) antennas at both the TX and RX. Co-polarized and cross-polarized LOS measured path losses are also shown. The corresponding close-in reference equation lines with respect to a 1 m free space reference distance are shown. Path loss models labeled ‘LOS B’ correspond to angle combinations in which the TX and RX antennas are pointed perfectly on boresight with each other. ‘LOS NB’ measurements indicate TX-RX antenna combinations that were not aligned on boresight. Four distinct T-R separation distances were measured: 10, 20, 30, and 40 m. The TX height was at 4.06 meters and RX heights were at 2 meters relative to ground.

the RX antenna was subsequently rotated in incremental steps defined in Table 3.14 and Table 3.15.

### 6.1.1 Free Space Path Loss Models

Fig. 6.1 shows the co- and cross-polarized path loss models with respect to a 1 m free space reference distance for the outdoor free space measurements. The models labeled ‘LOS B’ refer to measurements where the TX and RX antennas are pointed perfectly on boresight with each other. The models labeled ‘LOS NB’ refer to measurements where the TX and RX antennas were not aligned on boresight but where the TX and RX sites were still in a LOS environment. In Fig. 6.1 the LOS boresight path loss exponent and shadowing factor for the co-polarized scenario (V-

V) were measured to be 2.0 and 0.37 dB respectively, and agrees perfectly with free space propagation, and indicating the validity of measurements and results. The ‘LOS NB’ path loss exponent and shadowing factors with respect to a 1 m free space reference distance for arbitrary antenna pointing angles were measured to be 4.8 and 16.8 dB, respectively for the co-polarized scenario, and decreased to 3.1 and 2.1 dB when considering only the best angles, that is, angles with strongest received power, indicating the advantage of using beamforming and beam combining techniques to dramatically increase link margin, improve SNR, and/or to extend the coverage range [49] [50].

In the cross-polarized scenario, the ‘LOS NB’ path loss exponent and shadowing factor with respect to a 1 m free space reference distance at arbitrary antenna pointing angles were measured to be 5.5 and 12.9 dB respectively, and decreased to 4.5 and 6.2 dB when considering only the best angles as seen in Fig. 6.1. When considering any arbitrary angle the reduction in signal attenuation is only 7 dB / decade when comparing the co- and cross-polarization measurements for the LOS NB scenario. In addition, the XPD factor for LOS measurements was 19 dB / decade with respect to a 1 meter free space reference distance. Understanding the cross-polarization factors and properties in this LOS environment can help with the development of co- and cross-polarized mmWave wireless systems for frequency reuse, or for systems that employ antenna polarization diversity

Fig. 6.2 shows the omnidirectional path loss models for 73 GHz LOS free space propagation in the outdoor environment. The LOS omnidirectional path loss exponent and shadowing factor in the co-polarized scenario were 2.0 and 0.32 dB respectively, agreeing very well with theoretical free space propagation. In the cross-polarized scenario, the path loss exponent and shadowing factor with respect to a 1 m free space reference distance were measured to be 3.8 and

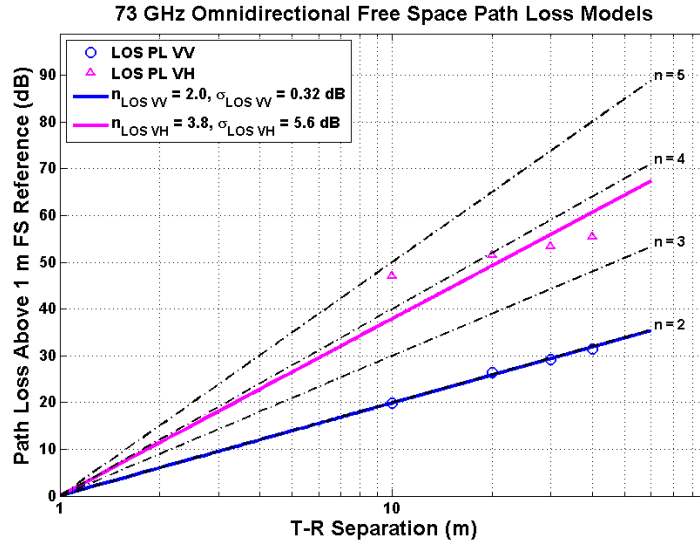


Fig. 6.2 73 GHz omnidirectional LOS free space propagation path loss models with respect to a 1 meter free space reference distance, synthesized from the 73 GHz directional measurements, using a pair of 27 dBi gain horn antennas with a 7° HPBW. Four distinct T-R separation distances were measured: 10, 20, 30, and 40 m. The TX height was at 4.06 meters and RX heights were at 2 meters relative to ground.

5.6 dB respectively, thereby offering a cross-polarization isolation of 18 dB / decade. Similar to the directional model XPD factor, this information can be used to design mmWave wireless systems that take advantage of antenna polarization diversity.

Table 6.1 and Table 6.2 summarize the directional (unique pointing angle) and omnidirectional path loss models for both V-V and V-H antenna polarization configurations for the 73 GHz outdoor LOS channel over an 800 MHz RF bandwidth. The directional path loss models for the outdoor LOS environment prove the viability of the 73 GHz wideband channel in a busy courtyard environment, and the potential to use beamforming and beam combining techniques with the use of high gain directional antennas for non-boresight-to-boresight antenna orientations. In addition, the omnidirectional LOS model in the courtyard environment validates the theoretical path loss exponent of  $n = 2$  as compared to traditional cellular frequency bands.

Table 6.1 Path loss exponents and shadowing factors with respect to a 1 m free space reference distance obtained from the 73 GHz outdoor free space directional (unique pointing angle) measurements, computed for both co-polarized (V-V) and cross-polarized (V-H) scenarios. The TX height was at 4.06 meters and RX heights were at 2 meters relative to ground. TX and RX antennas had 27 dBi of gain with 7° HPBW.

Directional Parameters		TX-RX Polarization			
		V-V		V-H	
TX-ID	Environment Type	PLE	$\sigma$ (dB)	PLE	$\sigma$ (dB)
CMN FS1	LOS-B	2.0	0.4	3.9	6.1
	LOS-NB	4.8	16.8	5.5	12.9
	LOS-NB Best	3.1	2.1	4.5	6.2

Table 6.2 Omnidirectional path loss exponents and shadowing factors with respect to a 1 m free space reference distance synthesized using the 73 GHz free space directional measurements, computed for both co-polarized (V-V) and cross-polarized (V-H) scenarios. TX and RX antennas had 27 dBi of gain with 7° HPBW.

Omnidirectional Parameters		TX-RX Polarization			
		V-V		V-H	
TX-ID	Environment Type	PLE	$\sigma$ (dB)	PLE	$\sigma$ (dB)
CMN FS1	LOS	2	0.32	3.8	5.6

### 6.1.2 Propagation Characteristics of the 73 GHz Free Space Channel

As explained and analyzed for the indoor 73 GHz channel, propagation characteristics for the outdoor free space channel at 73 GHz are also important to understand. Both temporal and spatial statistics are necessary in order to build robust wireless systems that can be adjusted based on models determined for the outdoor environment. At a high level, time delay spreads are important for equalization and beam combining techniques, whereas spatial statistics such as lobes and multipath arrivals are important for beam combining, beamforming, and energy seeking antenna algorithms in order to improve link margin and obtain signals with better SNR. In addition, understanding these statistics for cross-polarized antenna configurations will be important for creating antenna polarization diversity mmWave systems. Fig. 6.3 shows the RMS delay spread CDF for the 73 GHz directional measured data obtained for each unique pointing angle combination in both co-polarized (VV) and cross-polarized (VH) scenarios. The mean and standard deviation of the RMS delay spreads in the co-polarized scenario were measured to be

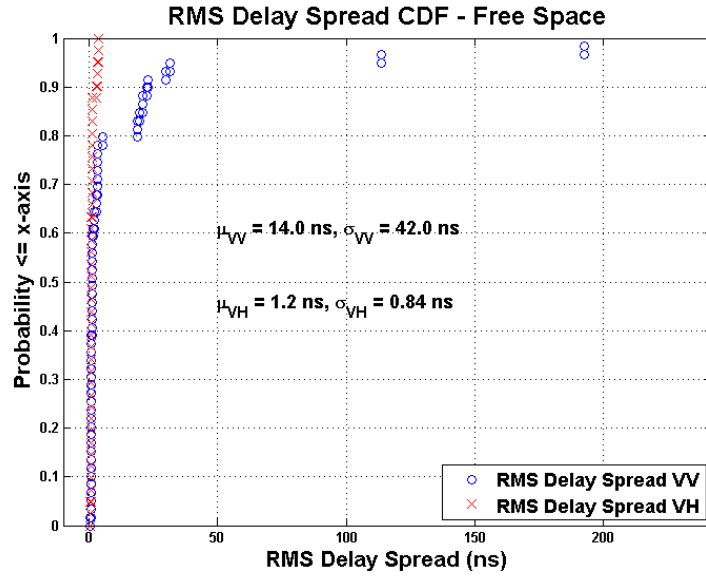


Fig. 6.3 Cumulative distribution function for the outdoor free space 73 GHz unique pointing angle measurements for both co- and cross-polarized antenna configurations. T-R separations distances were for 10, 20, 30, and 40 meters, with the TX antenna at a height of 4.06 meters and the RX antennas at a height of 2 meters. TX and RX antennas had 27 dBi of gain with 7° HPBW.

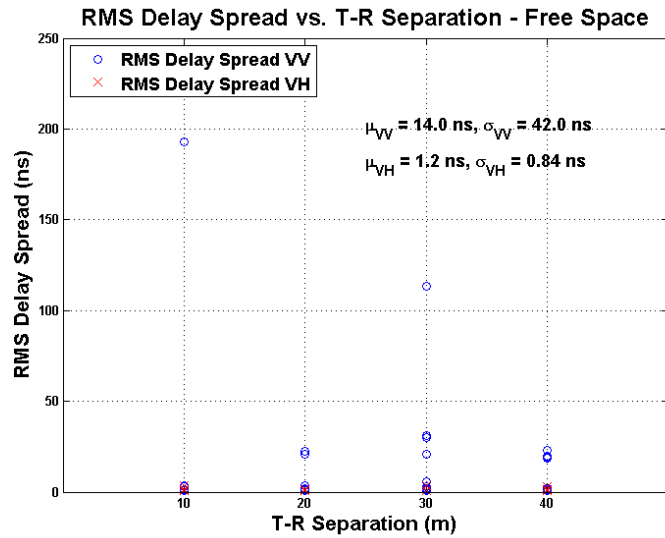


Fig. 6.4 RMS delay spreads as a function of T-R separation distance for the outdoor free space 73 GHz unique pointing angle measurements for both co- and cross-polarized antenna configurations. T-R separations distances were for 10, 20, 30, and 40 meters, with the TX antenna at a height of 4.06 meters and the RX antennas at a height of 2 meters. TX and RX antennas had 27 dBi of gain with 7° HPBW.

14.0 ns and 42.0 ns respectively, with the 50% and 90% probabilities occurring for RMS delay spreads of 0.5 ns and 23 ns, respectively. In the cross-polarized scenario (VH), the mean and

standard deviation of the RMS delay spreads were measured to be 1.2 ns and 0.84 ns respectively, indicating that the cross-polarization discrimination mitigates the propagation of multipath components in an outdoor free space LOS environment. Fig. 6.4 shows the RMS delay spreads as a function of T-R separation distance for the co-polarized and cross-polarized measurements in the outdoor LOS free space environment. The RMS delay spreads appear to be relatively constant over T-R separation distance. The RMS delay spreads for the co- and cross-polarization antenna configurations are relatively uniform as a function of T-R separation distance, respectively. There is one large RMS Delay spread value close to 200 ns for the co-polarized scenario at 10 m, which can be attributed to a reflection off a far building in the environment that was still detectable above the noise floor during measurements. Overall, the cross-polarization RMS delay spreads are relatively small meaning that a majority of the multipath components reach the receiver in a short window. However, these small RMS delay spread values may be from weaker multipath components not detectable by the receiver, due to the XPD factor for cross-polarization.

Fig. 6.5 shows the mean number of multipath components detected at the RX for any arbitrary pointing angle combination between the TX and RX using 27 dBi gain,  $7^\circ$  HPBW antennas. These values show how multipath components arrive at the RX in directional windows in the azimuth plane for fixed elevations. The number of multipath components was determined by implementing a peak detection algorithm that is able to pick up the multipath peak values. It is apparent that more multipath components were detected using V-V antenna polarization rather than V-H cross-polarized antennas, at arbitrary pointing angles. This is most likely due to the weaker cross-polarization signals detected near the noise floor due to the cross-polarization isolation factor. Overall, even in a LOS environment a receiver with directional antenna can

observe multiple copies of the same signal in a tight angular window due to reflections in the environment. The outdoor LOS courtyard measurements show that the propagating signal arrives at the receiver in tight angular windows after reflecting off of obstructions in the environment. This demonstrates that the multipath effect is present in the 73 GHz channel LOS environment, when using directional antennas at both the TX and RX. This will lead to the use of equalization

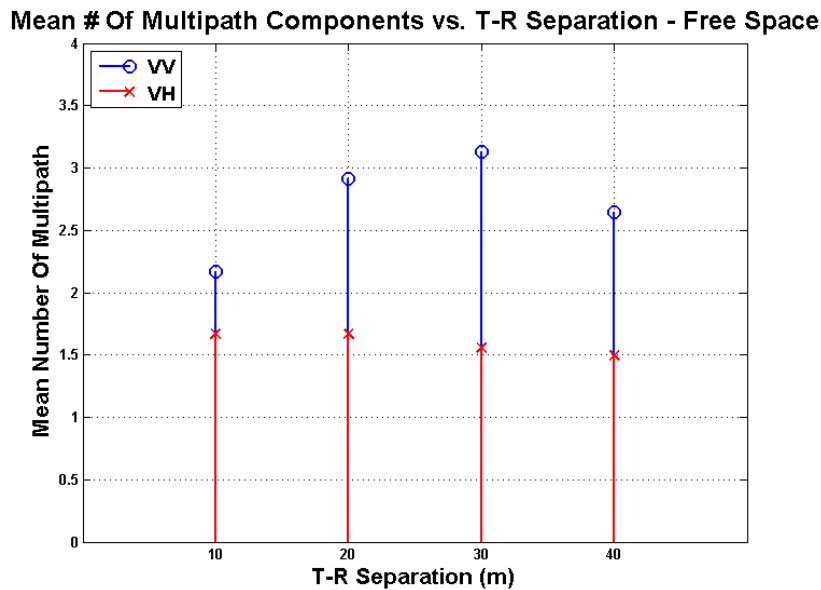


Fig. 6.5 Mean number of multipath components detected at the receiver for any arbitrary unique pointing angle combination between the TX and RX antennas for the outdoor free space 73 GHz unique pointing angle measurements for both co- and cross-polarized antenna configurations. T-R separations distances were for 10, 20, 30, and 40 meters, with the TX antenna at a height of 4.06 meters and the RX antennas at a height of 2 meters. TX and RX antennas had 27 dBi of gain with 7° HPBW.

Table 6.3 Summary of the mean number of multipath components detected at the receiver for any arbitrary unique pointing angle combination between the TX and RX antennas for the outdoor free space 73 GHz unique pointing angle measurements for both co- and cross-polarized antenna configurations. T-R separations distances were for 10, 20, 30, and 40 meters, with the TX antenna at a height of 4.06 meters and the RX antennas at a height of 2 meters. TX and RX antennas had 27 dBi of gain with 7° HPBW.

Location	Environment Type	T-R Separation (m)	Mean Number of Multipath Components	
			VV	VH
Outdoor Free Space	LOS	10.0	2.2	1.7
		20.0	2.9	1.7
		30.0	3.1	1.6
		40.0	2.6	1.5

algorithms at the RX in order to mitigate ISI and to improve SNR. Table 6.3 shows a summary of the multipath components observed at the receiver for arbitrary unique pointing angles for the 73 GHz outdoor free space measurements for both co- and cross-polarized antenna configurations.

PDPs with typical and maximum RMS delay spreads from the free space measurements with co- and cross-polarized antennas are shown in Fig. 6.6. The PDP in Fig. 6.6 (a) was recorded at RX1 for CMN\_FS1 in a LOS\_B environment. When the TX antenna and RX antenna were perfectly pointed towards each other with 10 meters T-R separation distance, the first and strongest arriving component corresponded to the LOS component. The second multipath component resulted from a reflection off of a building wall in the surrounding environment. Fig. 6.6 (b) shows the PDP acquired at the same location as Fig. 6.6 (a), but with the RX antenna 24 ° off the boresight angle in the azimuth plane. There were two multipath components, similar to Fig. 6.6 (a), one was the LOS component and the other came from a reflection off of a building in the courtyard. The received power of each component was about 40 dB lower than the received power as in Fig. 6.6 (a). Fig. 6.6 (c) shows the PDP obtained at the same location with the same TX and RX azimuth and elevation combination as Fig. 6.6 (a) for cross-polarization. Compared to Fig. 6.6 (a), the delay time between multipath components was similar, while the received power for cross-polarization was about 30 dB lower than that for co-polarization configuration in Fig. 6.6 (c). Fig. 6.6 (b) shows the largest observed RMS delay spread of the collected free space measurements, at RX1 for MTC1, the same location as in Fig. 6.6 (a) and Fig. 6.6 (d). The first arriving peak corresponded to the LOS component arriving at the flange of the RX antenna and the last peak resulted from multiple reflections off the building behind the RX, which travelled an additional 700 feet (or 213) meters) beyond the first arriving component.

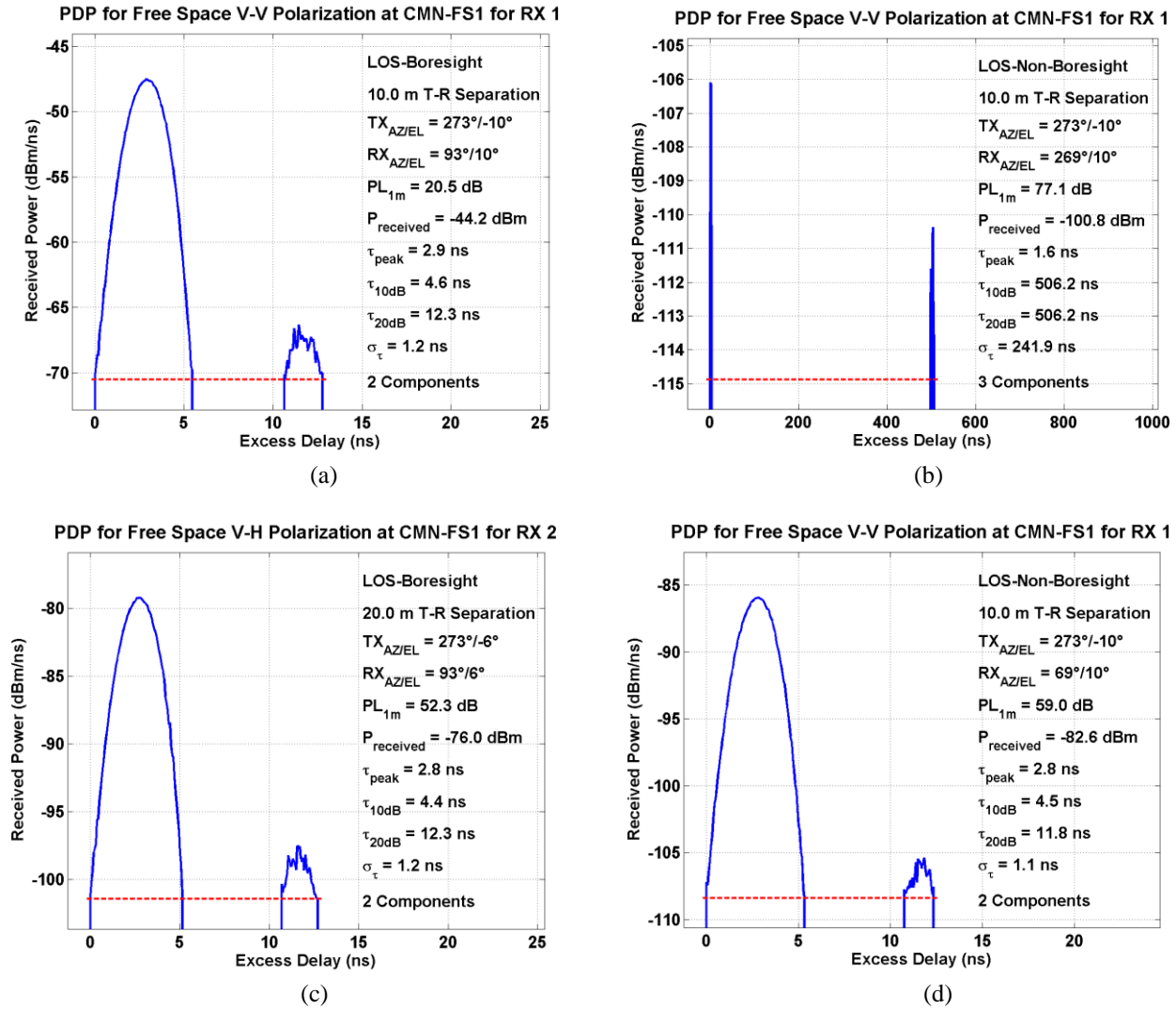


Fig. 6.6 (a), (c) and (d) show typical power delay profiles (PDPs) measured in the outdoor free space environment with vertical-to-vertical and vertical-to-horizontal polarization. (b) shows the PDP with maximum RMS delay spread observed from the outdoor free space measurements. The horizontal red line on each PDP represents the computed noise threshold level. Because of the absence of GPS synchronization between the TX and RX, the excess delay is relative to the first arriving multipath above the threshold level. The received power is in dBm / nanosecond. Each PDP corresponds to a recording for a specific TX-RX antenna angle combination in the azimuth and elevation planes. The measurement information including environmental type, T-R separation distance, TX and RX azimuth and elevation, path loss with respect to 1 meter, received power, maximum peak delay, excess delay 10 dB and 20 dB down from the maximum peak, RMS delay spread, and number of multipath components are shown on the right of each PDP.

## 6.2 73 GHz Outdoor Channel with Foliage

The measurement details for the 73 GHz outdoor foliage measurements were fully explained in Section 3.2.2. The purpose of these measurements was to investigate the 73 GHz propagation

channel when influenced by tree foliage, in addition to understanding the ground bounce effect between the TX and RX. The measurements were performed on the MetroTech Commons Courtyard in Downtown Brooklyn as detailed in Fig. 3.20, Fig. 3.21, and Fig. 3.23. Different measurements sweeps were performed for co- and cross-polarized antenna configurations and a more descriptive explanation the measurement procedure can be found in Section 3.2.2.3. The RX antenna was always at a height 2 meters relative to ground and the TX antenna was set to a height of 4.06 meters relative to ground in order simulate a lamppost level access point envisaged for future base stations in the mmWave regime for common courtyard areas. Four RX locations were measured, with T-R separation distances of 10 m, 20 m, 30 m, and 40 m, where each subsequent RX location was 10 m further from the previous as detailed in Fig. 3.23.

### **6.2.1 Foliage Attenuation Path Loss Models**

Fig. 6.7 shows the 73 GHz foliage attenuation path loss model for the co-polarized (V-V) and cross-polarized (V-H) antenna configurations. This model was created by finding the omnidirectional total received power level at each RX location, and subsequently determining the total path loss after removing the 27 dBi TX and RX antenna gains. Next, the relative path loss with respect to a 1 m free space reference distance was found, and the models were obtained

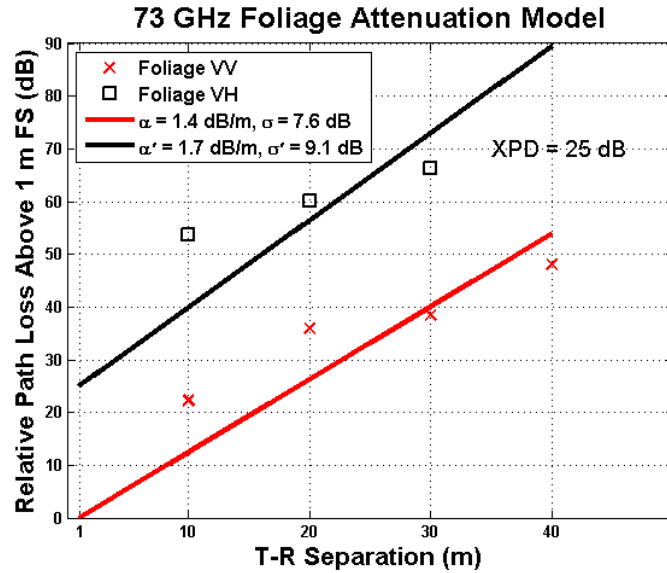


Fig. 6.7 73 GHz outdoor foliage attenuation path loss model for co- (V-V) and cross-polarized (V-H) antenna configurations for T-R separation distances of 10, 20, 30, and 40 meters with the TX at a height of 4.06 meters and the RX heights at 2 meters relative to ground, using 27 dBi gain, 7° HPBW antennas. The foliage type was common cherry tree branches, leaves and trunks.

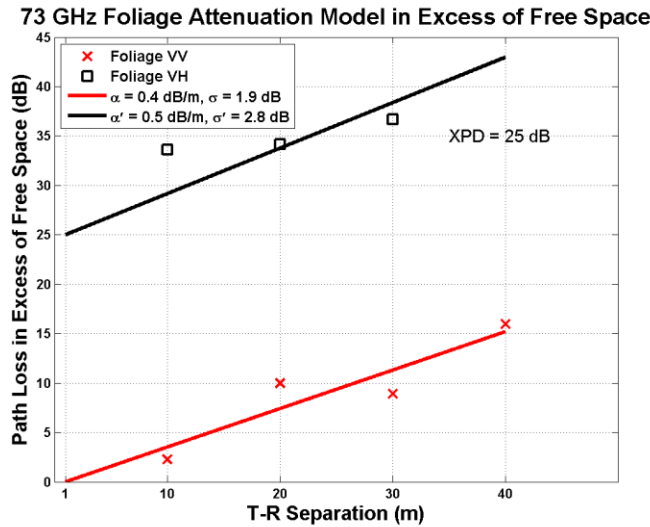


Fig. 6.8 73 GHz outdoor foliage attenuation path loss model in excess of free space path loss for co- (V-V) and cross-polarized (V-H) antenna configurations for T-R separation distances of 10, 20, 30, and 40 meters with the TX at a height of 4.06 meters and the RX heights at 2 meters relative to ground, using 27 dBi gain, 7° HPBW antennas. The foliage type was common cherry tree branches, leaves and trunks.

by applying the MMSE method using T-R separations in m (linear distance scale). For the co-polarized scenario, the foliage attenuation rate was determined to be  $\alpha=1.4 \text{ dB/m}$  with a minimum mean square error of  $\sigma=7.6 \text{ dB}$ .

In order to find the foliage attenuation model for the cross-polarized scenario, the cross-polarization discrimination (XPD) factor was subtracted from the total path loss values. The XPD factor was equal to 25 dB when using the 27 dBi gain horn antennas, and was determined from free space measurements as can be observed from Fig. 6.7. The MMSE method was again applied on the cross-polarized data, and the foliage attenuation rate was found to be  $\alpha=1.7$  dB/m with a minimum mean square error of  $\sigma=9.1$  dB. The following equations can be used to estimate the total path loss through foliage:

$$\text{Co-polarized V-V:} \quad PL(d)[dB] = PL(d_0) + 1.4 \times d[m] \quad (6.1)$$

$$\text{Cross-polarized V-H:} \quad PL(d)[dB] = PL(d_0) + 25 + 1.7 \times d[m] \quad (6.2)$$

where,

$$PL(d_0) = 20 \log_{10} \left( \frac{4\pi d_0}{\lambda} \right) \quad (6.3)$$

Fig. 6.8 shows another 73 GHz foliage attenuation path loss model for the co-polarized (V-V) and cross-polarized (V-H) antenna polarization configurations. This model was created by finding the omnidirectional total received power level at each RX location, and subsequently determining the total path loss after removing the 27 dBi TX and RX antenna gains. Next, the path loss in excess of free space was found, and the models were obtained by applying the MMSE method using T-R separation distances in meters (linear distance scale). For the co-polarized scenario, the foliage attenuation rate was determined to be  $\alpha=0.4$  dB/m with a minimum mean square error of  $\sigma=1.9$  dB.

In order to find the foliage attenuation model for the cross-polarized scenario, the XPD factor was subtracted from the total path loss values. The XPD was equal to 25 dB for the 27 dBi horn antennas, and was determined from free space measurements as can be observed from Fig. 6.6. The MMSE method was again applied on the cross-polarized data, and the foliage attenuation

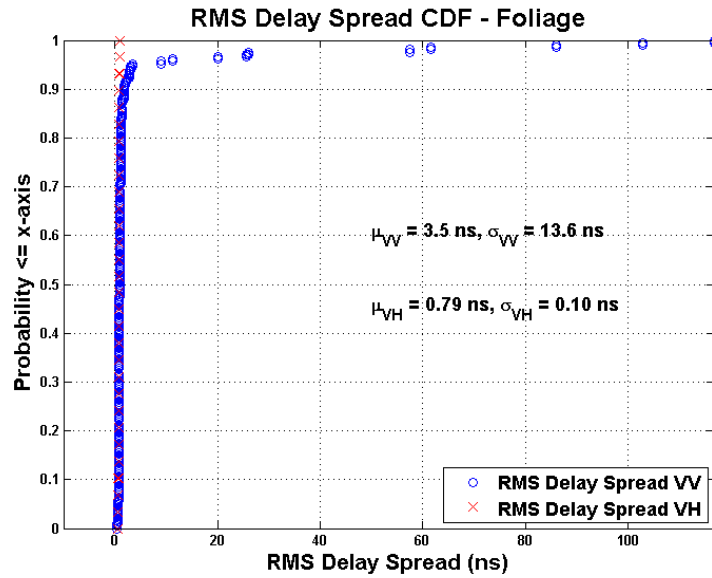


Fig. 6.9 Cumulative distribution function for the outdoor foliage attenuated 73 GHz unique pointing angle measurements for both co- and cross-polarized antenna configurations. T-R separations distances were for 10, 20, 30, and 40 meters, with the TX antenna at a height of 4.06 meters and the RX antennas at a height of 2 meters. TX and RX antennas had 27 dBi of gain with  $7^\circ$  HPBW.

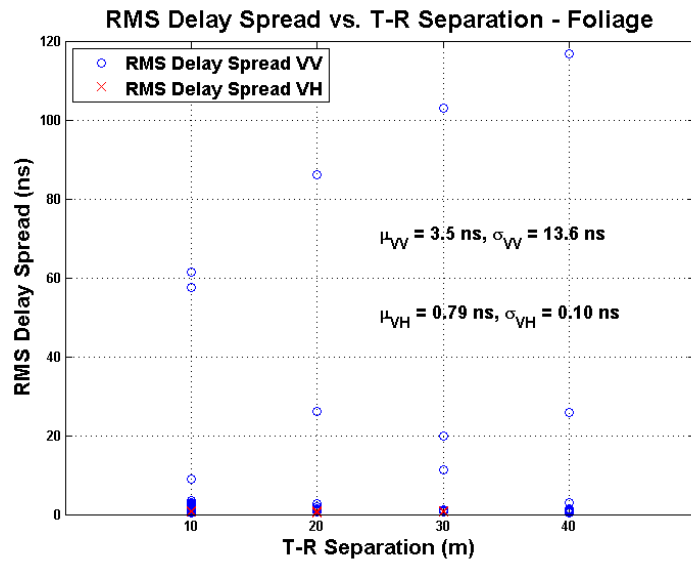


Fig. 6.10 RMS delay spreads as a function of T-R separation distance for the outdoor foliage attenuated 73 GHz unique pointing angle measurements for both co- and cross-polarized antenna configurations. T-R separations distances were for 10, 20, 30, and 40 meters, with the TX antenna at a height of 4.06 meters and the RX antennas at a height of 2 meters. TX and RX antennas had 27 dBi of gain with  $7^\circ$  HPBW.

rate was found to be  $\alpha'=0.5 \text{ dB/m}$  with a minimum mean square error of  $\sigma'=2.8 \text{ dB}$ . The following equations can be used to estimate the path loss in excess of free space through the

foliage:

$$\text{Co-polarized V-V: } PL(d)[dB] = PL_{FS}(d) + 0.4 \times d[m] \quad (6.4)$$

$$\text{Cross-polarized V-H: } PL(d)[dB] = PL_{FS}(d) + 25 + 0.5 \times d[m] \quad (6.5)$$

where,

$$PL_{FS}(d) = 20 \log_{10} \left( \frac{4\pi d_0}{\lambda} \right) \quad (6.6)$$

### 6.2.2 Characteristics of the Outdoor 73 GHz Propagation Channel with Foliage

As explained and analyzed for the outdoor free space 73 GHz channel propagation in Section 6.2.2, propagation characteristics for the 73 GHz channel with foliage are also important to understand for environments that include trees and other types of vegetation. Both temporal and spatial statistics are necessary in order to build robust wireless systems that can be adjusted based on models determined for the outdoor foliage influenced environment. Empirical results that include the effects of foliage can help to build accurate models that will help in designing future systems and networks that may experience such foliage in the propagation environment. Both temporal and spatial statistics will be important for these designs.

Fig. 6.9 shows the RMS delay spread CDF for the 73 GHz directional measured data in an outdoor foliage environment obtained for each unique pointing angle combination in both co-polarized (V-V) and cross-polarized (V-H) antenna scenarios. The mean and standard deviation of the RMS delay spreads in the co-polarized scenario were measured to be 3.5 ns and 13.6 ns respectively, with the 50% and 90% probabilities occurring for RMS delay spreads of 0.5 ns and 0.9 ns, respectively. For the cross-polarized scenario (V-H), the mean and standard deviation of the RMS delay spreads were measured to be 0.79 ns and 0.1 ns respectively, indicating that the cross-polarization discrimination mitigates the propagation of multipath components.

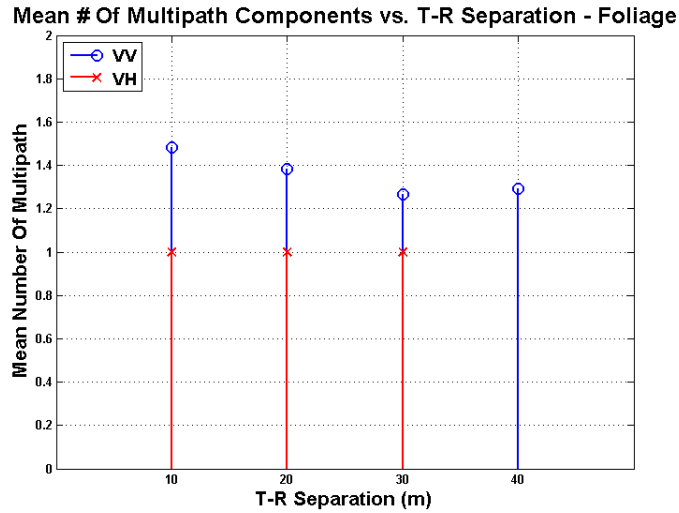


Fig. 6.11 Mean number of multipath components detected at the receiver for any arbitrary unique pointing angle combination between the TX and RX antennas for the outdoor foliage attenuated 73 GHz unique pointing angle measurements for both co- and cross-polarized antenna configurations. T-R separations distances were for 10, 20, 30, and 40 meters, with the TX antenna at a height of 4.06 meters and the RX antennas at a height of 2 meters. TX and RX antennas had 27 dBi of gain with 7° HPBW.

Table 6.4 Summary of the mean number of multipath components detected at the receiver for any arbitrary unique pointing angle combination between the TX and RX antennas for the outdoor foliage attenuated 73 GHz unique pointing angle measurements for both co- and cross-polarized antenna configurations. T-R separations distances were for 10, 20, 30, and 40 meters, with the TX antenna at a height of 4.06 meters and the RX antennas at a height of 2 meters. TX and RX antennas had 27 dBi of gain with 7° HPBW.

Location	Environment Type	T-R Separation (m)	Mean Number of Multipath Components	
			VV	VH
Foliage	NLOS	10.0	1.5	1.0
		20.0	1.4	1.0
		30.0	1.3	1.0
		40.0	1.3	-

Fig. 6.10 shows the RMS delay spreads as a function of T-R separation distance for the co-polarized and cross-polarized measurements. The RMS delay spreads appear to be relatively constant over T-R separation distances. The RMS delay spreads are very small for cross-polarization measurements due to weaker signals not being detected by the receiver as a result of the extra foliage and antenna polarization mismatch.

Fig. 6.11 shows the mean number of multipath components detected at the RX for any arbitrary pointing angle combination between the TX and RX using 27 dBi gain, 7° HPBW TX and RX antennas, through the cherry tree foliage. These values show how multipath arrives at the RX in directional windows in the azimuth plane for fixed elevations, when the propagating wave encounters foliage. The number of multipath components was determined by implementing a peak detection algorithm that is able to pick up the multipath peak values. It is apparent that more multipath components were detected using V-V antenna polarization rather than V-H cross-polarized antennas, at arbitrary pointing angles. This is most likely due to the weaker cross-polarization signals detected near the noise floor due to the cross-polarization isolation factor. Overall, even in the foliage attenuated environment a receiver with directional antennas can observe multiple copies of the same signal in a tight angular window due to reflections in the environment. The outdoor foliage attenuated measurements show that on average one to two copies of the transmitted signal reach the receiver for V-V polarization and only one copy of the transmitted signal reaches the receiver for V-H polarization. The reduction in multipath components in the foliage attenuated environment can be attributed to extra foliage attenuation that will make arriving signals weaker and thus undetectable by our channel sounder system as they approach the noise floor. Table 6.4 shows a summary of the multipath components observed at the receiver for arbitrary unique pointing angles for the 73 GHz outdoor free space measurements for both co- and cross-polarized antenna configurations.

PDPs with typical and maximum RMS delay spreads from the foliage and ground bounce measurements with co- and cross-polarization are shown in Fig. 6.12. The PDP in Fig. 6.12 (a) was recorded at RX1 for CMN1 in a NLOS environment. When the TX and RX antenna were perfectly pointed towards each other, with 10 meters T-R separation distance, the first and

strongest arriving multipath component corresponded to the LOS component arriving at the flange of RX antenna. The second multipath component came from a reflection off of foliage or branches. The third component traveled 400 meters after reflecting off of the two buildings behind the TX and RX. Fig. 6.12 (b) shows the PDP acquired at the same location as Fig. 6.12 (a) with vertical-to-horizontal polarization, where the TX and RX antennas were pointing towards each other through the foliage. Only the LOS component was observed through the foliage. The lower received power, compared to the received power from free space measurements for the same T-R separation distance, can be attributed to the attenuation caused by foliage and branches between the TX and RX. Fig. 6.12 (c) shows the PDP obtained from the ground bounce measurements at the same location of Fig. 6.12 (a) and Fig. 6.12 (b) for vertical-to horizontal polarization, with the same TX and RX antenna azimuth angle combination as in Fig. 6.12 (b). Compared to Fig. 6.12 (b), the received power in Fig. 6.12 (c) was 2 dB lower, which can be attributed to the reflection off the ground. Fig. 6.12 (d) shows the largest observed RMS delay spread from the foliage measurements, recorded at RX4 for MTC1 with 40 meters T-R separation distance. The first component arrived away from the LOS boresight direction, and the second peak which was 2 dB lower than the first peak, came from one reflection from a surrounding building, traveling an additional 240 feet (or 73 m) beyond the first arriving component

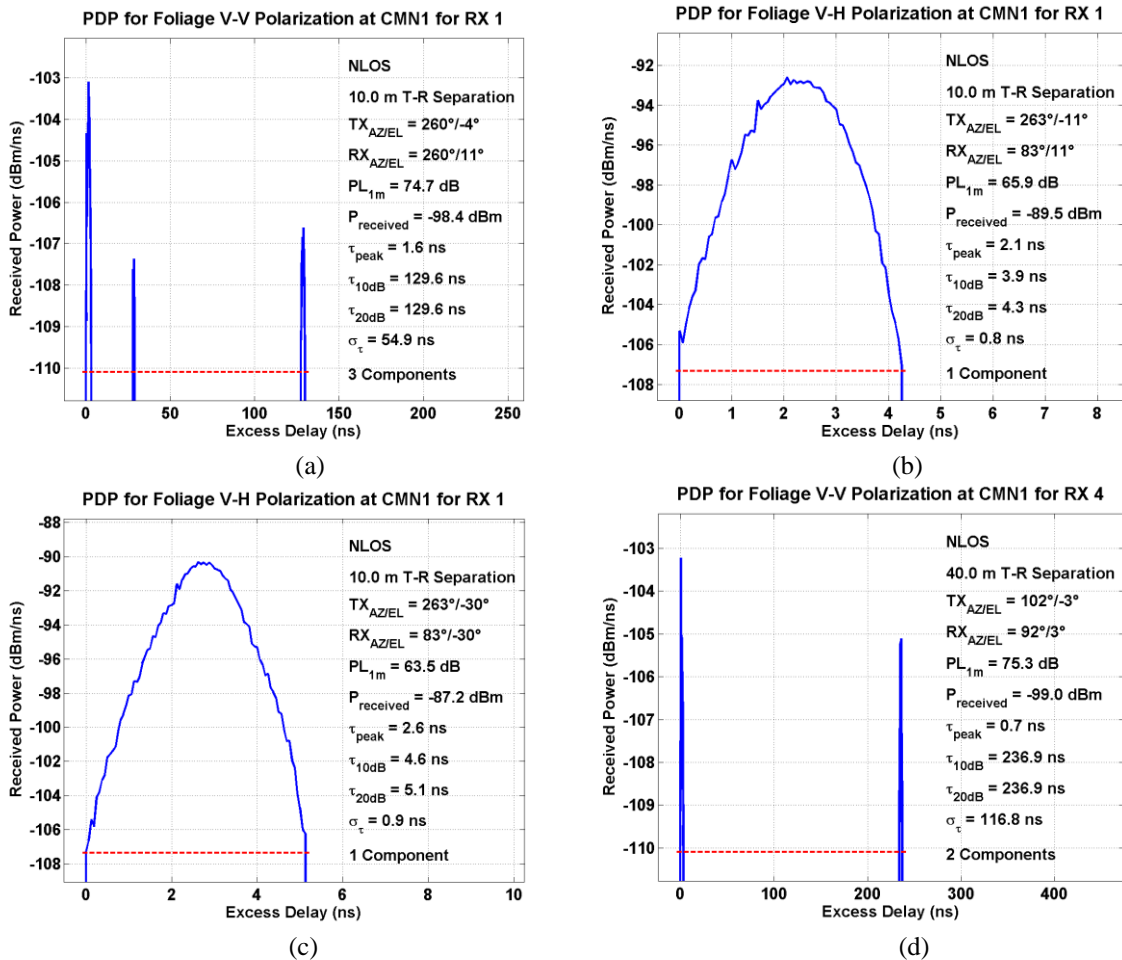


Fig. 6.12 (a), (b) and (c) show typical power delay profiles (PDP) measured in the foliage environment for vertical-to-vertical and vertical-to-horizontal antenna polarization configurations. (d) shows the PDP with maximum RMS delay spread in foliage measurement. The horizontal red line on each PDP represents the computed noise threshold level. Because of the absence of GPS synchronization between the TX and RX, the excess delay is relative to the first arriving multipath above the threshold level. The received power is in dBm / nanosecond. Each PDP corresponds to a recording for a specific TX-RX antenna angle combination in the azimuth and elevation planes. The measurement information including environmental type, T-R separation distance, TX and RX azimuth and elevation, path loss with respect to 1 meter, received power, maximum peak delay, excess delay 10 dB and 20 dB down from the maximum peak, RMS delay spread, and number of multipath components are shown on the right of each PDP.

### 6.2.3 Ground Bounce Reflection Coefficient

A sub-set of the 73 GHz foliage measurements investigated ground bounces, where the T-R separation distances ranged between 10 m and 40 m in 10 m increments, where the elevations of the 27 dBi TX antenna located 4.06 m above the ground and the RX antenna located 2 m above ground level were changed to guarantee perfect ground bounce reflection between the TX and RX antennas. The goal of this work was to do a comparison of reflection coefficients computed based on different T-R separations distances and incident angles to the ground surface, similar to that presented in [58]. The ground material consisted of a soil, dirt, and gravel mixture. It is noted here that while the TX antenna was pointed downwards, the radiation inevitably travelled an unknown distance through the foliated canopy before experiencing the ground bounce, and so the ground bounce reflection coefficients shown in this work will degrade as a result of the foliage loss and the ground bounce. Since the RX antenna was placed at 2 m above ground level and well below tree tops and canopies, the radiation did not encounter branches or leaves after the reflection from the ground.

The ground bounce reflection coefficients were recovered by determining the total free space distance travelled from TX to RX based on the elevation angles (and using trigonometry), and removing the excess free space path loss and foliage attenuation from the total received power. This was performed for the co-polarized and cross-polarized scenarios. Note that for the cross-polarized measurements, the XPD of 25 dB was removed from the total measured received power when recovering the ground bounce reflection coefficient.

The distance traveled in tree canopies  $d_{foliage}$  and the total travelled free space distance  $d_{tot,FS}$  were recovered as follows:

$$d_{foliage} = \frac{h_{TX}}{\sin(|\phi_{TX}|)} \quad (6.7)$$

$$d_{tot,FS} = \sqrt{(h_{TX} + h_{RX})^2 + d_{sep}^2} \quad (6.8)$$

where  $h_{TX}, h_{RX}$  are the TX and RX heights respectively in meters, and  $\phi_{TX}$  and  $\phi_{RX}$  are the TX and RX elevation angles in radians,  $d_{sep}$  is the T-R separation distance in meters.

The received power in linear scale at T-R separation distance  $d_{sep}$  for the free space LOS measurement is:

Co-polarized VV: 
$$Pr_{fs} = \frac{P_T G_T G_R \lambda^2}{(4\pi d_{sep})^2} \quad (6.9)$$

Cross-polarized VH: 
$$Pr_{fs} = \frac{P_T G_T G_R \lambda^2}{(4\pi d_{sep})^2} \cdot 10^{-XPD/10} \quad (6.10)$$

The received power in linear scale at T-R separation distance  $TR_{sep}$  for foliage ground bounce measurement is:

Co-polarized VV:

$$Pr_{foliage} = \frac{P_T G_T G_R \lambda^2}{(4\pi d_{tot,FS})^2} \cdot 10^{-d_{foliage} \cdot \alpha / 10} \cdot |\Gamma|^2 \quad (6.11)$$

Cross-polarized VH:

$$Pr_{foliage} = \frac{P_T G_T G_R \lambda^2}{(4\pi d_{tot,FS})^2} \cdot 10^{-XPD/10} \cdot 10^{-d_{foliage} \cdot \alpha / 10} \cdot |\Gamma|^2 \quad (6.12)$$

where  $\Gamma$  is the reflection coefficient, and  $\alpha$  is the foliage attenuation rate in excess of free space ( $\alpha=0.4$  dB/m for V-V measurements,  $\alpha =0.5$  dB/m for V-H measurements). From the above equations, we can obtain the magnitude of the reflection coefficient:

$$|\Gamma| = \frac{d_{tot,fs}}{d_{sep}} \cdot \sqrt{10^{d_{foliage} \cdot \alpha / 10}} \cdot \sqrt{\frac{Pr_{foliage}}{Pr_{fs}}} \quad (6.13)$$

Fig. 6.13 shows the magnitude of ground bounce reflection coefficients as a function of the incident angle for both co-polarized and cross-polarized measurements. Table 6.5 summarizes

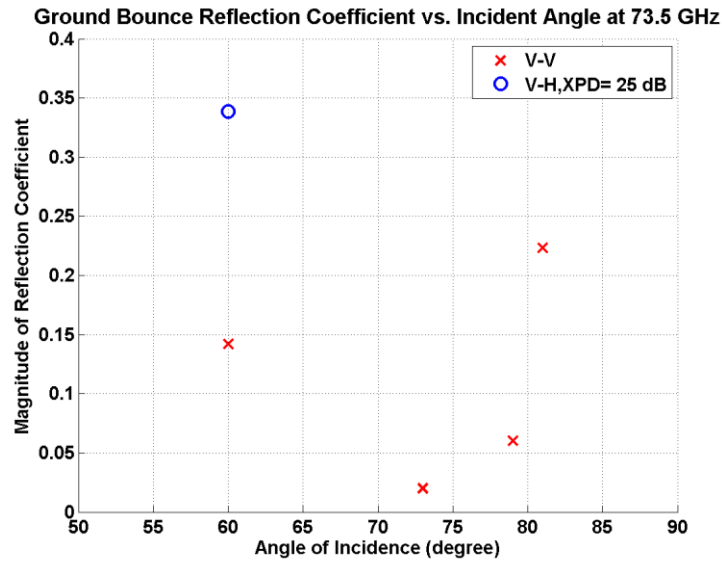


Fig. 6.13 Ground bounce reflection coefficient versus incidence angle at 73 GHz through foliage for a ground material of soil, dirt, and gravel, using 27 dBi gain, 7° HPBW directional antennas for co- and cross-polarization configurations. T-R separation distances of 10, 20, 30, and 40 meters with the TX at a height of 4.06 meters and the RX heights at 2 meters relative to ground were measured.

Table 6.5 Magnitude of ground bounce reflection coefficients obtained from the 73 GHz measurements through foliage for a ground material of soil, dirt, and gravel, using 27 dBi gain, 7° HPBW directional antennas for co- and cross-polarization configurations. T-R separation distances of 10, 20, 30, and 40 meters with the TX at a height of 4.06 meters and the RX heights at 2 meters relative to ground were measured. Magnitude of theoretical Fresnel reflection coefficient when  $\epsilon_r = 7$ .

RX	T-R Separation (m)	TX EL (°)	RX EL (°)	Angle of Incidence (°)	Angle of Reflection (°)	Ground Bounce Distance Traveled (m)	Magnitude of Reflection Coefficient (Measured)		Magnitude of Reflection Coefficient (Theoretical $\epsilon_r = 7$ )	
							VV	VH	VV	VH
1	10	-30	-30	60	60	11.7	0.142	0.339	0.164	0.164
2	20	-17	-17	73	73	20.9	0.020	-	0.086	-
3	30	-11	-11	79	79	30.6	0.060	-	0.298	-
4	40	-9	-9	81	81	40.4	0.223	-	0.373	-

the magnitude of the ground bounce reflection coefficients recovered from the co-polarized and cross-polarized measurements. The magnitude of reflection coefficients for VH measurements at RX 2, 3, 4 are unavailable because signal above the noise floor was not detected at these RX

locations during foliage ground bounce measurements with a transmit power of -7.9 dBm. The reflection coefficients, determined by the material properties and angle of incidence, for vertical and horizontal polarization are given by the equations below [24] [54]:

$$\Gamma_{\parallel} = \frac{\eta_2 \sin \theta_t - \eta_1 \sin \theta_i}{\eta_2 \sin \theta_t + \eta_1 \sin \theta_i} \quad (6.14)$$

$$\Gamma_{\perp} = \frac{\eta_2 \sin \theta_i - \eta_1 \sin \theta_t}{\eta_2 \sin \theta_i + \eta_1 \sin \theta_t} \quad (6.15)$$

where  $\Gamma_{\parallel}$  and  $\Gamma_{\perp}$  represent the Fresnel reflection coefficients when the electric field is parallel and perpendicular to the plane of incidence, respectively.  $\theta_i$  is the angle of incidence and  $\theta_t$  is the angle of refraction.  $\eta_1$  represents the intrinsic impedance of free space and  $\eta_2$  represents the intrinsic impedance of the incident material. For the case when the first medium is free space and the permeability of the two medium are the same, where  $\mu_1 = \mu_2$ , the parallel reflection coefficient can be simplified to [24]:

$$\Gamma'_{\parallel} = \frac{\cos \theta - \sqrt{\epsilon_r - \sin^2 \theta}}{\cos \theta + \sqrt{\epsilon_r - \sin^2 \theta}} \quad (6.16)$$

where  $\epsilon_r$  is the relative permittivity of the incident material, and  $\theta$  is the angle of incidence.  $\Gamma'_{\parallel}$  represents the Fresnel reflection coefficients reflection coefficients for vertical polarization, where the E-field is in the plane of incidence.

The ground can be modeled as soil with dirt, gravel, and fallen leaves. Some measurements show that the permittivity of soil at 35 GHz and 94 GHz ranges from about 3 to 5 [59]. Without exact values of permittivity of the soil for the ground bounce measurements at 73 GHz, a series of typical values of permittivity of soil were plotted in Fig. 6.14. Fig. 6.14 shows theoretical and measured reflection coefficients and the magnitude of reflection coefficients under different

permittivity values of soil as a function of the incident angle for parallel polarization. Table 6.5 summarizes the magnitude of the ground bounce reflection coefficients recovered from the co-polarized and cross-polarized measurements and the theoretical values calculated when we assume that  $\epsilon_r = 7$ . The magnitude of reflection coefficients for VH measurements at RX 2, 3, and 4 are unavailable because signal above the noise floor was not detected at these RX locations during foliage ground bounce measurements with a transmit power of -7.9 dBm.

The reflection coefficients computed in Table 6.5 can be used in applications predicting path loss and signal strength levels for E-band communication systems operating at 73 GHz. The predicted ground bounce onto hard soil can be predicted through foliage using these coefficients in simulators and ray-tracing algorithms and applications.

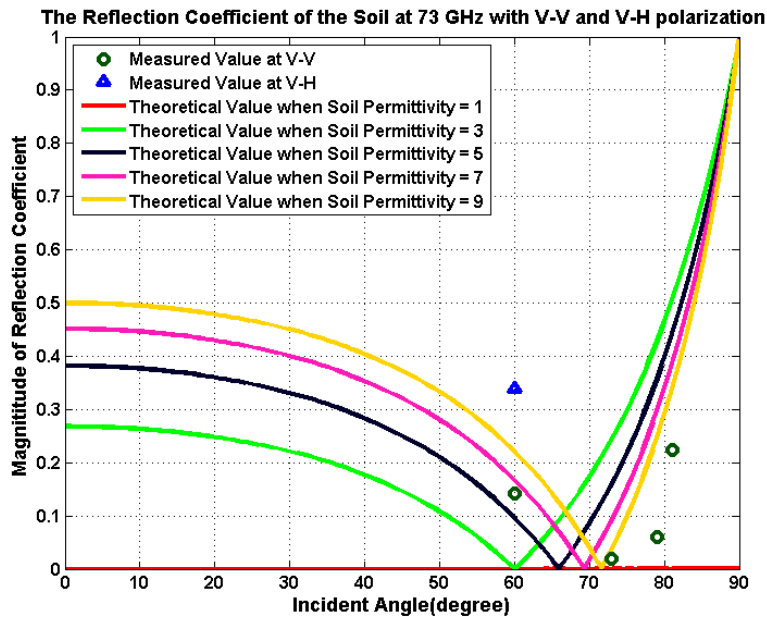


Fig. 6.14 The theoretical and measured ground bounce reflection coefficient versus incidence angle at 73 GHz for vertical-to-vertical polarization through foliage for a ground material of soil, dirt, gravel, and fallen leaves using 27 dBi gain, 7° HPBW directional antennas for co- and cross-polarization configurations. T-R separation distances of 10, 20, 30, and 40 meters with the TX at a height of 4.06 meters and the RX heights at 2 meters relative to ground were measured. Theoretical permittivity values of the soil range, from 1 to 9 in increments of 2 in order to compare theoretical and empirical reflection coefficients.

## Chapter 7 Conclusion

This technical report presented the 73 GHz ultra-wideband propagation measurements performed in Brooklyn, New York in order to investigate the properties and characteristics of the indoor and foliage wideband channels. In this article, we provided a comprehensive literature survey of indoor propagation measurements and corresponding results in the UHF/Microwave bands as well as some mmWave bands, in order to better understand and analyze the current 73 GHz obtained results in the context of past research. The measurement campaign details such as hardware used, environments and configurations tested, and site locations and layouts were also explained. Finally, initial results of the indoor and foliage channels were explained to help provide insight for next generation radio-system design and channel modeling purposes.

From the propagation measurements, directional path loss models were computed for the indoor office environment and revealed LOS-B path loss exponents of 2.2 ( $\sigma = 0.84$  dB) and 4.9 ( $\sigma = 8.7$  dB) for co-polarized and cross-polarized antenna settings, respectively. In NLOS environments the path loss exponents were 5.1 ( $\sigma = 12.2$  dB) and 6.5 (8.8 dB) for co-polarized and cross-polarized antenna settings, respectively. In addition, the path loss exponent was reduced by 18 dB / decade when considering the best directions between the TX and RX antennas for the NLOS environment. These results are consistent with previous outdoors work in the 28 GHz and 73 GHz bands [53] [54]. For indoor omnidirectional models, the path loss exponents for LOS environments were 1.5 ( $\sigma = 0.76$ ) and 4.5 ( $\sigma = 6.6$ ) for co-polarized and cross-polarized antenna settings, respectively. In NLOS environments the omnidirectional path loss exponents were 3.1 ( $\sigma = 8.9$  dB) and 5.3 ( $\sigma = 0.69$  dB) for co-polarized and cross-polarized antenna settings, respectively. These path loss exponent results are very similar to current UHF/Microwave bands, the only difference being the additional path loss due to the increase in carrier frequency.

Temporal statistics of the indoor channel showed average RMS delay spreads of 11.8 ns and 4.8 ns for co- and cross-polarized antennas, respectively. For spatial statistics, the mean number of multipath components observed overall was 4.2 for any arbitrary pointing angle combination, with a standard deviation of 2.5. The indoor results also showed a very reflective environment, but with main directions of arrival, revealing that mmWave channels are more directional than omnidirectional, such that on average, 2.2 main angles of arrival (lobes) were observed in NLOS environments with co-polarized antennas. The AOAs for co- and cross-polarization measurements were uniformly distributed across the entire azimuth plane, and the same was observed for co-polarized AODs. The difference in received power levels and subsequently high path loss exponents for cross-polarized antennas can lead to antenna polarization diversity systems for indoor mmWave communications. A directional indoor partition-dependent model showed that office partitions and general walls induced attenuations of 14.25 dB and 16.14, respectively.

The outdoor free space and foliage measurements allowed us to compute statistics of a LOS courtyard environment. For the directional path loss model, the co- and cross-polarized path loss exponents for LOS-B measurements were 2 ( $\sigma = 0.4$  dB) and 3.9 ( $\sigma = 6.1$  dB), respectively. For LOS-NB, the path loss exponents were 4.8 ( $\sigma = 16.8$ ) and 5.5 ( $\sigma = 12.9$ ) for co- and cross-polarized antennas, respectively. Similar to the indoor directional model, when choosing the best LOS-NB angles, path loss was reduced, specifically by 17 dB / decade and 10 dB / decade for co- and cross-polarized antennas, respectively. The free space omnidirectional model results in a LOS path loss exponent of 2 (identical to theoretical free space) and 3.8 for co- and cross-polarized antennas, respectively. For temporal statistics, the mean RMS delay spread was 14.0 ns and 1.2 ns for co- and cross-polarized antennas, respectively. The overall mean number of

multipath components for free space measurements for any arbitrary pointing angle combination was approximately between 2 and 3 for co-polarized antennas and was approximately 1.6 for cross-polarized antennas.

The outdoor foliage measurements allowed us to recover an attenuation path loss model, and foliage attenuation rates of 1.4 dB/m and 1.7 dB/m for the co-polarized and cross-polarized scenarios, respectively using a pair of 27 dBi gain ( $7^\circ$  beamwidth) directional antennas. The mean number of multipath components for the foliage measurements was 1.3 and 1 for the co- and cross-polarization scenarios, respectively. We were also able to determine ground bounce reflection coefficients, that together with the outdoor free space and foliage model parameters, can be used in ray-tracing and network simulations to model future mmWave E-band networks in common courtyards. For ground bounce incident angles of 60, 73, 79, and  $81^\circ$ , the magnitude of the reflection coefficients computed through foliage were 0.142, 0.02, 0.06, and 0.223, respectively. The path loss models and spatial and temporal statistics found for a common indoor environment for both co- and cross-polarized channels can be used to simulate and model future mmWave networks that may be deployed in office buildings.

Overall, this technical document allows one to understand the propagation database and models generated in regards to measurements recorded from the Fall of 2013 through the Summer of 2014 in both an indoor office environment and outdoor free space and foliage influenced environment at 73 GHz. The report provides detailed descriptions and analysis of the data collected with the intention of assisting in the development of statistical models to be used for simulations, and creating next generation mmWave wireless communications systems.

## References

- [1] “Looking ahead to 5G: building a virtual zero latency gigabit experience,” *White Paper*, Nokia, Dec. 2013.
- [2] “2020: Beyond 4G radio evolution for the gigabit experience,” *White Paper*, Nokia, 2011.
- [3] FCC Code of Federal Regulations, Title 47, Part 15, radio frequency devices [Online]. Available: <http://www.ecfr.gov>
- [4] T. S. Rappaport, J. N. Murdock, and F. Gutierrez, “State of the art in 60-GHz integrated circuits and systems for wireless Communications,” *Proceedings of the IEEE*, vol. 99, no. 8, pp. 1390 – 1436, Aug. 2011.
- [5] T. S. Rappaport, S. Sun, R. Mayzus, H. Zhao, Y. Azar, K. Wang, G. N. Wong, J. K. Schulz, M. K. Samimi, and F. Gutierrez, Jr., “Millimeter Wave Mobile Communications for 5G Cellular: It Will Work!” *IEEE Access*, vol. 1, pp. 335 – 349, 2013.
- [6] M. K. Samimi, “Characterization of the 28 GHz Millimeter-Wave Dense Urban Channel for Future 5G Mobile Cellular,” M. S. Thesis, May 2014.
- [7] T. A. Thomas, H. C. Nguyen, G. R. MacCartney, Jr., and T. S. Rappaport, “3D mmWave Channel Model Proposal,” accepted in *Vehicular Technology Conference (VTC Fall), 2014 IEEE 80<sup>th</sup>*, Sept 14 – 17, 2014.
- [8] M. Bensebti, J.P. McGeehan, and M.A. Beach, “Indoor Multipath Radio Propagation Measurements and Characterisation at 60 GHz,” *Microwave Conference, 1991. 21st European*, vol. 2, pp. 1217 – 1222, 9-12 Sept. 1991.
- [9] A. J. Motley and J. P. Keenan, “Personal communication radio coverage in buildings at 900 MHz and 1700 MHz”, *Electronic Letters*, vol. 24, no. 12, 1988.
- [10] S. Y. Seidel and T. S. Rappaport, “914 MHz path loss prediction models for indoor wireless communications in multifloored buildings,” *Antennas and Propagation, IEEE Transactions on*, vol. 40, no. 2, pp. 207-217, Feb. 1992.
- [11] C. Oestges and A. J. Paulraj, “Propagation into buildings for broad-band wireless access”, *IEEE Transactions on Vehicular Technology*, vol. 53, no. 2, pp. 521 – 536, March 2004.
- [12] European Cooperation in the Field of Scientific and Technical Research, EURO-COST 231, “Digital Mobile Radio Towards Future Generation Systems”, COST 231 Final report [Online]. Available: <http://www.lx.it.pt/cost231/>.

- [13] C. R. Anderson and T. S. Rappaport, "In-building wideband partition loss measurements at 2.5 and 60 GHz", *Wireless Communications, IEEE Transactions on*, vol. 3, no. 3, pp. 922 – 928.
- [14] R. R. Skidmore, T. S. Rappaport, and A.L. Abott, "Interactive coverage region and system design simulation for wireless communication systems in multifloored indoor environments: SMT Plus," *Universal Personal Communications, 1996. Record., 1996 5th IEEE International Conference on*, vol. 2, pp. 646 – 650, 29 Sept – 2 Oct 1996.
- [15] R. R. Skidmore, "A Comprehensive In-Building and Microcellular Wireless Communication System Design Tool", Master Thesis, Virginia Polytechnic Institute and State University, June 1997.
- [16] A. G. Siamarou and M. O. Al-Nuaimi, "Multipath delay spread and signal level measurements for indoor wireless radio channels at 62.4 GHz", *Vehicular Technology Conference, 2001. VTC 2001 Spring. IEEE VTS 53rd*, vol. 1, pp. 454 – 458, 2001.
- [17] G. Durgin, T. S. Rappaport, and H. Xu, "Measurements and models for radio path loss and penetration loss in and around homes and trees at 5.85 GHz," *Communications, IEEE Transactions on*, vol. 46, no. 11, pp. 1484 – 1496, Nov 1998.
- [18] H. K. Chung and H. L. Bertoni, "Indoor propagation characteristics at 5.2GHz in home and office environments," *Communications and Networks, Journal of*, vol. 4, no.3, pp.176 – 188, Sept. 2002.
- [19] K. Sato, T. Manabe, T. Ihara, H. Saito, S. Ito, T. Tanaka, K. Sugai, N. Ohmi, Y. Murakami, M. Shibayama, Y. Konishi, and T. Kimura, "Measurements of reflection and transmission characteristics of interior structures of office building in the 60-GHz band", *Antennas and Propagation, IEEE Transactions on*, no. 45, issue 12, pp. 1783 – 1792.
- [20] K. Sato, H. Kozima, H. Masuzawa, T. Manabe, T. Ihara, Y. Kasashima, and K. Yamaki, "Measurements of reflection characteristics and refractive indices of interior construction materials in millimeter-wave bands," *Vehicular Technology Conference, 1995 IEEE 45th*, Jul. 1995, pp. 449 – 453, Dec. 1997.
- [21] T. Manabe, K. Sato, H. Masuzawa, K. Taira, T. Ihara, Y. Kasashima, and K. Yamaki, "Polarization dependence of multipath propagation and high-speed transmission characteristics of indoor millimeter-wave channel at 60 GHz," *Vehicular Technology, IEEE Transactions on*, vol. 44, no. 2, pp. 268 – 274, May 1995.
- [22] "Digital Mobile Radio Toward Future Generation Systems," COST 231, European Commission, Brussels, Belgium, 1999.

- [23] ITU, “Propagation data and prediction methods for the planning of indoor radio communication systems and radio local area networks in the frequency range 900 MHz to 100 GHz,” 2012.
- [24] T. S. Rappaport, “Wireless Communications: Principles and Practice,” 2<sup>nd</sup> Edition, Prentice Hall, 2002.
- [25] J. Ahmadi-Shokouh, S. Noghanain, E.Hossain, M. Ostadrahimi, and J. Dietrich, “Reflection Coefficient Measurement for House Flooring Materials at 57-64 GHz,” *Global Telecommunications Conference, 2009. GLOBECOM 2009. IEEE*, pp. 1 – 6, Nov. 30 – Dec. 4 2009.
- [26] H. Yang, M. Herben, and P. Smulders, “Impact of antenna pattern and reflective environment on 60 GHz indoor radio channel characteristics,” *Antennas and Wireless Propagation Letters, IEEE*, vol. 4, pp. 300 – 303, 2005.
- [27] T. S. Rappaport and D. A. Hawbaker, “Wide-band microwave propagation parameters using circular and linear polarized antennas for indoor wireless channels,” *Communications, IEEE Transactions on*, vol. 40, no. 2, pp. 240 – 245, Feb 1992.
- [28] C. A. Balanis, “Antenna theory: analysis and design,” 3rd Edition, Wiley-Interscience, 2005.
- [29] FCC Code of Federal Regulations, Title 47, Part 101, Fixed Microwave Services, Subpart C Technical Standards [Online]. Available: <http://www.ecfr.gov>
- [30] 70/80 GHz Spec Sheet [Online]. Available: [http://www.lightpointe.com/images/AireBeam\\_70\\_and\\_80\\_GHz\\_LightPointe\\_Spec\\_Sheet\\_021312.pdf](http://www.lightpointe.com/images/AireBeam_70_and_80_GHz_LightPointe_Spec_Sheet_021312.pdf)
- [31] ETSI EN 302 217-3, Fixed Radio Systems; Characteristics and requirements for point-to-point equipment and antennas; Part 3: Harmonized EN covering essential requirements of Article 3.2 of R&TTE Directive for equipment operating in frequency bands where simplified or no frequency co-ordination procedures are applied [Online]. Available: <http://portal.etsi.org>
- [32] ETSI EN 302 217-4-2, Fixed Radio Systems; Characteristics and requirements for point-to-point equipment and antennas; Part 4-2: Antennas; Harmonized EN covering the essential requirements of article 3.2 of R&TTE Directive [Online]. Available: <http://portal.etsi.org>
- [33] R. Leppänen, J. Lähteenmäki, S. Tallqvist, “Radiowave propagation at 900 and 1800 MHz bands in wooded environments,” COST 231 TD (92)112, Helsinki, 1992.
- [34] “Propagation prediction models,” COST 231 Final Rep., Ch. 4, pp.134–148.

- [35] T. Kurner, R. Faub, and A. Wasch, "A hybrid propagation modelling approach for DCS 1800 macrocells," *Vehicular Technology Conference, 1996. Mobile Technology for the Human Race., IEEE 46th*, vol. 3, pp. 1628 – 1632, Apr 28 – May, 1996.
- [36] F. Wang and K. Saraband, "An enhanced millimeter-wave foliage propagation model," *Antennas and Propagation, IEEE Transactions on*, vol. 53, no. 7, pp. 2138 – 2145, July 2005.
- [37] F. Wang, I. Koh, and K. Sarabandi, "Long distance path-loss estimation for wave propagation through a forested environment," *Proceedings: IEEE International Antennas and Propagation Society International Symposium, 2004. IEEE*, vol. 1, pp. 992 – 925, June 20-25, 2004.
- [38] S. Y. Seidel and T. S. Rappaport, "A ray tracing technique to predict path loss and delay spread inside buildings," *Global Telecommunications Conference, 1992. Conference Record., GLOBECOM '92. Communication for Global Users., IEEE*, vol. 2, pp. 649-653, Dec. 6-9, 1992.
- [39] S. Y. Seidel and T. S. Rappaport, "Site-specific propagation prediction for wireless in-building personal communication system design," *Vehicular Technology, IEEE Transactions on*, vol. 43, no. 4, pp. 879 - 891, Nov 1994.
- [40] C.M.P. Ho and T. S. Rappaport, "Wireless channel prediction in a modern office building using an image-based ray tracing method," *Global Telecommunications Conference, 1993, including a Communications Theory Mini-Conference. Technical Program Conference Record, IEEE in Houston. GLOBECOM '93., IEEE*, vol. 2, pp. 1247-1251, Nov. 29-Dec. 2, 1993.
- [41] C.M.P. Ho and T. S. Rappaport., "Effects of antenna polarization and beam pattern on multipath delay spread and path loss in indoor obstructed wireless channels," *Universal Personal Communications, 1992. ICUPC '92 Proceedings., 1st International Conference on*, pp. 04.02/1,04.02/5, Sept. 29 – Oct. 1, 1992.
- [42] C.M.P. Ho, T.S. Rappaport, and P. Koushik, "Antenna effects on indoor obstructed wireless channels and a deterministic image-based wide-band propagation model for in-building personal communication systems," *International Journal of Wireless Information Networks*, vol. 1, pp. 61-76, Jan. 1994.
- [43] H. Xu, V. Kukshya, and T. S. Rappaport, "Spatial and temporal characterization of 60 GHz indoor channels," *Vehicular Technology Conference, 2000. IEEE-VTS Fall VTC 2000. 52nd*, vol. 1, pp. 6-13, 2000.

- [44] K. R. Schaubach, N. J. Davis, IV., and T. S. Rappaport, "A ray tracing method for predicting path loss and delay spread in microcellular environments," *Vehicular Technology Conference, 1992, IEEE 42nd*, vol. 2, pp. 932-935, May 10-13, 1992.
- [45] G. Durgin, N. Patwari, and T. S. Rappaport, "An advanced 3D ray launching method for wireless propagation prediction," *Vehicular Technology Conference, 1997, IEEE 47th*, vol. 2, pp.785-789, May. 4-7, 1997.
- [46] G. Durgin, N. Patwari, and T. S. Rappaport, "Improved 3D ray launching method for wireless propagation prediction," *Electronics Letters*, vol. 33, no. 16, pp. 1412-1413, July 31, 1997.
- [47] D. Cox, "Delay doppler characteristics of multipath propagation at 910 MHz in a suburban mobile radio environment," *Antennas and Propagation, IEEE Transactions on*, vol. 20, no. 5, pp. 625–635, Sep 1972.
- [48] <http://www.phasematrix.net/phasematrix/products/quicksyn-synthesizers/quicksyn-synthesizers-full>
- [49] S. Sun and T. S. Rappaport, "Multi-beam antenna combining for 28 GHz cellular link improvement in urban environments," *Global Communications Conference (GLOBECOM), 2013 IEEE*, pp. 3754 – 3750, 9-13 Dec. 2013.
- [50] S. Sun, "Antenna Diversity Combining and Beamforming at Millimeter Wave Frequencies," M. S. Thesis, May 2014.
- [51] G. R. MacCartney, Jr., M. K. Samimi and T. S. Rappaport, "Omnidirectional Path Loss Models in New York City at 28 GHz and 73 GHz," to appear in *Personal Indoor and Mobile Radio Communications (PIMRC), 2014 IEEE 25th International Symposium on*, Sept 2 – 5, 2014.
- [52] Y. Azar, G. N. Wong, K. Wang, R. Mayzus, J. K. Schulz, H. Zhao, F. Gutierrez, Jr., D. Hwang, T. S. Rappaport, "28 GHz propagation measurements for outdoor cellular communications using steerable beam antennas in New York City", *2013 IEEE International Conference on Communications (ICC)*, pp. 5143 – 5147, June 9 - 13, 2013.
- [53] G. R. MacCartney, T. S. Rappaport, "73 GHz millimeter wave propagation measurements for outdoor urban mobile and backhaul communications in New York City," *IEEE International Conference on Communications (ICC), 2014*, 10-14 June. 2014
- [54] M. Samimi, K. Wang, Y. Azar, G. N. Wong, R. Mayzus, H. Zhao, J. K. Schulz, S. Sun, F. Gutierrez, Jr., T. S. Rappaport, "28 GHz Angle of Arrival and Angle of Departure Analysis for Outdoor Cellular Communications using Steerable Beam Antennas in New York City,"

2013 *IEEE Vehicular Technology Conference (VTC Spring)*, 2013 *IEEE 77th*, pp. 1 – 6, June 2-5, 2013.

- [55] C.R. Anderson and T.S. Rappaport, “In-building wideband partition loss measurements at 2.5 and 60 GHz,” *Wireless Communications, IEEE Transactions on*, vol. 3, no. 3, pp. 922 - 928, May 2004.
- [56] G. Durgin, T. S. Rappaport, and H. Xu, “Measurements and models for radio path loss and penetration loss in and around homes and trees at 5.85 GHz,” *Communications, IEEE Transactions on*, vol. 46, no. 11, pp. 1484-1496, Nov 1998.
- [57] G. Durgin, T.S. Rappaport, T. S., and H. Xu, “Partition-Based Path Loss Analysis for In-Home and Residential Areas at 5.85 GHz,” *Proc of the 1998 Global Telecom Conference*, Vol. 2, pp. 904-909, Nov. 8-12, 1998.
- [58] O. Landron, M. J. Feuerstein, M.J, and T.S. Rappaport “A comparison of theoretical and empirical reflection coefficients for typical exterior wall surfaces in a mobile radio environment,” *Antennas and Propagation, IEEE Transactions on*, vol. 44, no. 3, pp.341-351, Mar. 1996.
- [59] A. J. Gatesman, T. M. Goyette, J. C. Dickinson, J. Waldman, J. Neilson, and W. E. Nixon, “Physical scale modeling the millimeter-wave backscattering behavior of ground clutter”, *ProcSPIE*, Vol. 4370, (2001).